



**HAL**  
open science

# Coupling 1D atom arrays to an optical nanofiber : Demonstration of an efficient Bragg atomic mirror

Aveek Chandra

► **To cite this version:**

Aveek Chandra. Coupling 1D atom arrays to an optical nanofiber : Demonstration of an efficient Bragg atomic mirror. Atomic Physics [physics.atom-ph]. Université Pierre et Marie Curie - Paris VI, 2017. English. NNT : 2017PA066582 . tel-01916366

**HAL Id: tel-01916366**

**<https://theses.hal.science/tel-01916366>**

Submitted on 8 Nov 2018

**HAL** is a multi-disciplinary open access archive for the deposit and dissemination of scientific research documents, whether they are published or not. The documents may come from teaching and research institutions in France or abroad, or from public or private research centers.

L'archive ouverte pluridisciplinaire **HAL**, est destinée au dépôt et à la diffusion de documents scientifiques de niveau recherche, publiés ou non, émanant des établissements d'enseignement et de recherche français ou étrangers, des laboratoires publics ou privés.

**THÈSE DE DOCTORAT  
DE L'UNIVERSITÉ PIERRE ET MARIE CURIE**

**Spécialité : Physique**

**École doctorale : “Physique en Île-de-France”**

réalisée

**au Laboratoire Kastler Brossel**

présentée par

**Aveek CHANDRA**

pour obtenir le grade de :

**DOCTEUR DE L'UNIVERSITÉ PIERRE ET MARIE CURIE**

Sujet de la thèse :

**Coupling 1D Atom Arrays to an Optical Nanofiber:  
Demonstration of an Efficient Bragg Atomic Mirror**

soutenue le 21 Novembre 2017

devant le jury composé de :

M.	Hugues de Riedmatten	Rapporteur
M.	Mauro Antezza	Rapporteur
M <sup>me</sup>	Catherine Schwob	Examineur
M.	Kamel Bencheikh	Examineur
M.	Julien Laurat	Directeur de thèse



# Acknowledgments

Last few years in Paris have been lovely in many ways. I have explored and travelled in and around France. I have enjoyed the art and culture, the impressive architecture and the natural beauty. In a way, I have gotten used to the language, culture and traditions here.

I am grateful to Julien Laurat for giving me the opportunity to work in his team at Laboratoire Kastler Brossel. The research environment in the lab has been very upbeat and collaborative. I have learnt a lot from my colleagues and friends. Baptiste Gouraud, who built the nanofiber experiment from scratch, has been patient in training me initially in various parts of the experiment. Thanks to his enthusiasm and advice that have helped me grow as a scientist. I have learnt many details of the experiment from Neil Corzo-Trejo during my PhD. Thanks to his guidance, I have learnt to control and debug the experiment in an organized and efficient way. In nanofiber fabrication, Maxime Joos and I have collaborated to improve our setup and the process. Thanks to his support in this regard.

Thanks to Jeremy Raskop for sharing the workload of the experiment in the final year of my PhD and I have also enjoyed sharing some of my experiences with him. A lot of things, involving our experiment, are shared with the free-space sub-team. Thanks to Kun Huang, Pierre Vernaz-Gris and Mingtao Cao - for their contribution and cooperation. Thanks to Alexandra Sheremet for giving an exposure to theoretical toolboxes and approaches, which as experimentalists, we can sometimes miss out on. I would like to thank Imene Esteve from IMPMC, for sharing the electron microscopy facilities with us. I must acknowledge the assistance and support of the technicians in electronics and mechanical workshop at LKB. I would like to thank the other colleagues of my team, internship students, visiting members, other members of our lab and whoever I have crossed my path with, during these last few years. Kudos to everyone!

The love and care of my family, friends and relatives back home have always been special and have kept me going during the rigors of the research life. It was fun to hang out with my friends and companions here in Paris. They have helped me to unwind and enriched my life with interesting exchange of culture, history, food, etc.



# Contents

<b>Introduction</b>	<b>1</b>
<b>1 Optical Nanofibers (ONF)</b>	<b>9</b>
1.1 Propagation in optical nanofibers . . . . .	9
1.1.1 Solution of fields in a nanofiber . . . . .	10
1.1.2 Fundamental $HE_{11}$ mode in a nanofiber . . . . .	13
1.1.3 Chirality in nanophotonic systems . . . . .	15
1.2 Optical nanofiber fabrication . . . . .	18
1.2.1 Design and Requirements . . . . .	20
1.2.2 Preparing, monitoring and characterizing the process . . . . .	24
1.2.3 Fabrication: A Review Story . . . . .	32
1.2.4 Pulling Algorithm . . . . .	35
<b>2 A state-insensitive, compensated nanofiber trap</b>	<b>41</b>
2.1 A two-color dipole trap in the evanescent field . . . . .	41
2.1.1 Optical dipole potential and ac Stark shifts . . . . .	41
2.1.2 Dipole trapping with a nanofiber . . . . .	44
2.1.3 Light-shifts in a nanofiber trap . . . . .	45
2.1.4 Cancelling these shifts . . . . .	46
2.2 Experimental implementation . . . . .	48
2.2.1 MOT and nanofiber . . . . .	48
2.2.2 Polarization alignment of the nanofiber-guided light . . . . .	50
2.2.3 Cancelling the residual magnetic field: Zeeman sublevel microwave spectroscopy . . . . .	51
2.2.4 Laser systems and optical components: an overview . . . . .	54
2.2.5 Spectral filtering systems . . . . .	59
2.2.6 Trap loading sequence . . . . .	59
2.2.7 Procedure for obtaining the nanofiber trap . . . . .	61
2.2.8 Trap characterization . . . . .	64
<b>3 Bragg Reflection from 1D arrays of emitters</b>	<b>69</b>
3.1 Bragg reflection based on two-level atoms . . . . .	70
3.1.1 Single-atom reflection and transmission coefficients . . . . .	70
3.1.2 Spectra simulation . . . . .	74

3.2	Simulating the factors that affect Bragg reflection . . . . .	77
3.2.1	Effect of inhomogeneous broadening . . . . .	77
3.2.2	Effect of disorder induced by the filling factor . . . . .	77
3.2.3	Trapping potential and effect of disorder induced by imperfect axial localization . . . . .	77
3.3	Experimental setup . . . . .	81
3.4	Experimental results . . . . .	82
3.5	Bragg Reflection from arrays of three-level emitters . . . . .	85
3.5.1	Controllable Bragg mirror and optical switching . . . . .	88
	<b>Conclusion</b>	<b>91</b>
<b>A</b>	<b>Python interface for fiber-pulling</b>	<b>93</b>
<b>B</b>	<b>Electron Microscopy</b>	<b>95</b>
<b>C</b>	<b>Electronics for fast current reversal</b>	<b>99</b>
	<b>Bibliography</b>	<b>119</b>

# Introduction

Quantum optics was born in the second-half of the twentieth century in an attempt to understand light-matter interaction at the fundamental level. Since then, new attributes and phenomena such as photon antibunching, parametric downconversion and squeezing have enriched the field and led to new implications and interesting applications spanning physical sciences, information science and beyond. For example, in microscopy, one can detect the presence of quantum emitters, such as molecules in chemistry and biology, by looking at the photon statistics. In metrology [Kómár14], quantum entanglement enables atomic clocks to reach high levels of accuracy  $\sim 10^{-18}$ . Quantum optics has had a profound and continuing impact on the emergence and growth of quantum information science (QIS) [Nielsen10].

## Quantum Information science

Classical information is encoded in discrete values either 0 or 1, called classical bits. Quantum information, on the other hand, is encoded in quantum bits, called qubits, which can take a value of 0 or 1 or some linear combinations of 0 and 1. A qubit state in terms of orthogonal basis states  $|0\rangle$  and  $|1\rangle$ , can be written as:  $|\psi\rangle = \alpha|0\rangle + \beta|1\rangle$  where  $\alpha$  and  $\beta$  are complex probability amplitudes, with  $|\alpha|^2 + |\beta|^2 = 1$ . Qubits, unlike classical qubits, are sensitive to small external perturbations and noise which can easily destroy quantum superpositions. Such a loss of quantum properties is called decoherence.

Qubits can be broadly classified into stationary and flying qubits. Strong candidates for stationary qubits can be single atoms in high-finesse cavities, atomic ensembles, ions, quantum dots, isolated electrons in NV centers, etc. Stationary qubits can be useful for implementation of elementary quantum gates, like the controlled-NOT gate [Monroe95], and storage of quantum information [Julsgaard04].

Flying qubits, on the other hand, can be used to transmit information over long distances. Photons are a natural choice due to their low interaction with matter. Photonic qubits can be encoded in multiple degrees of freedom, including polarization, photon number, orbital angular momentum, time-bin and frequency. They are useful for transmission of quantum information as well as opening up new and ultra-secure ways of communication. Free-space communication with photons may be suitable for future inter-satellites communication in space [Boone15] or between a ground station and a satellite [Yin17]. But at the ground level, such communication is not practical because of obstacles in the path (i.e. no free line of sight). Additionally, environmental

noise and attenuation can lead to decoherence of the fragile quantum states.

An alternative way of communication is to use optical fibers. In this case, the quantum state is isolated from the environment but there are losses in the system because of scattering or absorption in silica. For example, the losses in telecom C-band fibers are  $\sim 0.2$  dB/km, leading to a transmission of 0.01% for every 200 km. In case of classical information encoded in coherent light pulses, one can amplify a signal before further transmission. However in case of quantum information it is not possible to amplify a quantum state, without adding noise to the state, by virtue of the no-cloning theorem [Wootters82]. To circumvent this issue of losing quantum information during transmission over long distances, a proposal [Briegel98] in 1998, introduced the idea of quantum repeaters (QR). It is a device that extends the range of communication between sender and receiver using resources like entanglement and storage of information with quantum memories (QM).

The practical realization of QR can potentially lead to extension of quantum communication to continental scales. In this context, one can envisage a quantum network [Kimble08], which provides a broad frontier for quantum computation, quantum communication and quantum metrology. Quantum networks are composed of quantum nodes, where quantum information is generated, processed and stored locally, and quantum channels linking the nodes for transfer and distribution of quantum information across the network. A quantum network will also allow us to study quantum many-body physics arising from nodal interactions mediated by channels [Lloyd96, Acín07].

The physical realization of quantum networks requires coherent and efficient transfer of information among multiple nodes (stationary qubits) through quantum channels (photonic qubits). For that, it is essential to reversibly map quantum states between these two types of qubits. This can be achieved via strong and well-controlled light-matter interaction. Hence, there are worldwide efforts to develop quantum interfaces for the realization of such strong light-matter interaction. This is the context of the thesis.

## Quantum non-linear optics

Photons are non-interacting by nature and they can be made to weakly interact via a medium. As a result, intense light beams are required for modifying the refractive index of a medium leading to non-linear effects for example second-harmonic generation (SHG) in crystals. This is the regime of classical non-linear optics. In quantum nonlinear optics [Chang14], the medium's response is different to one incident photon compared to two incident photons [Peyronel12, Tiarks14]. This is possible, if the first photon saturates the atom modifying the atom's response to the second photon. However, it is challenging to realize such a situation because of the limitation imposed by the atom-photon interaction strength.

The strength of the atom-photon interaction is characterized by the probability  $p$  of one photon to interact with one atom. If  $\sigma$  is the atom's absorption cross-section (effective area 'seen' by photons) and  $A$  is the beam mode area then this probability is given by:  $p \approx \sigma/A$  (see Figure 0.1). On atomic resonance, the absorption cross-section reaches its maximal value ( $\sigma \sim \lambda^2$ ) and the interaction probability reduces to:

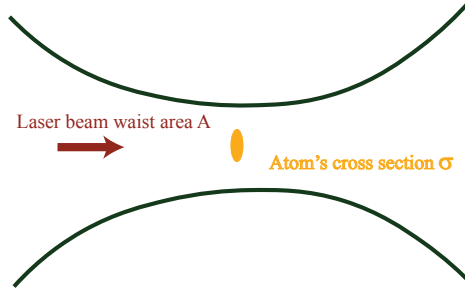


Figure 0.1 – A laser beam of waist area  $A$  and wavelength  $\lambda$  is tightly focused on an atom, with absorption cross-section area  $\sigma \sim \lambda^2$ . Optical diffraction does not allow the beam to be focused to areas much below  $\lambda^2$ . The atom-photon interaction probability  $p \approx \lambda^2/A$  is typically less than unity.

$p \approx \lambda^2/A$ . In free-space because of diffraction, the light cannot be focused much below wavelength scale limiting the atom-photon interaction probability to less than unity  $p < 1$ . Therefore, a large number of photons  $n \approx 1/p \approx A/\lambda^2$  are needed to saturate an atom and induce a nonlinear optical response. The best results obtained in the attempt to maximize atom-photon interaction probability  $p$  in free-space by concentrating a laser beam to a tiny area are:  $p \approx 0.05$  with neutral atoms [Darquié05, Khoon08],  $p \approx 0.01$  with ions [Hétet11] and  $p \approx 0.1$  with molecules on a surface [Wrigge08].

There have been efforts to build new interfaces and develop practical approaches to reach the regime  $p \rightarrow 1$ . We will review some of the main approaches here. Thus, experimental realization of strong atom-photon interaction is at the heart of this largely inter-connected field of quantum nonlinear optics, quantum many-body physics, quantum information science and technology.

## Approaches to strong atom-photon interaction

**Cavity QED** – A single atom, if placed in an optical cavity, has a higher probability  $p$  to interact with a photon because the photon bounces back and forth between the cavity walls (characterized by a finesse  $F$ ) before it escapes the cavity. The atomic states are coupled to the cavity modes and this leads to a nonlinear energy level structure given by the Jaynes-Cummings Hamiltonian. A cavity QED system is typically characterized by the single-atom cooperativity  $C$ . A large cooperativity  $C \gg 1$  ( $p$  approaches unity) implies that a single photon can alter the atom's response inside the cavity. Some experiments in cavity QED have demonstrated non-linear effects - nonlinear phase shift of one photon by one atom [Turchette95, Reiserer14], generation of single photons from a cavity-trapped atom [McKeever04] and using Rydberg atoms in high-Q microwave cavities [Har06].

The usual macroscopic dimension cavities can be substituted by micro- and nanoscale cavities. There have been cavity QED experiments where atoms or “artificial atoms”

are interfaced with - microtoroidal resonators and microsphere resonators [Aoki06, Dayan08, Shomroni14], bottle microresonators [Junge13], fiber cavities [Steiner13], and photonic crystal nanocavities [Englund10, Thompson13, Tiecke14].

**Collective atomic excitation** – A collective state of  $N$  atoms can also show increased coupling to a single electromagnetic mode. For three-level atoms, with two ground states  $|g\rangle, |s\rangle$  and an excited state  $|e\rangle$ , a photon can be absorbed by the whole ensemble and mapped onto a single collective state:  $|S_i\rangle = \frac{1}{\sqrt{N}} \sum_{i=1}^N |g_1, \dots, s_i, \dots, g_N\rangle$ . A well-known protocol in this context is the Duan-Lukin-Cirac-Zoller (DLCZ) protocol [Duan01]. In this protocol, detection of a single photon heralds the creation of a single collective excitation. A phased-matched coherent beam can then be applied to convert this collective excitation into a propagating photon. This is a promising method to generate single photons from atomic ensembles [Chou04]. A scalable, practical implementation of this protocol can find applications in building quantum-repeater architecture and quantum networks.

Atomic ensembles also enable to realize reversible light-matter interfaces, for instance under conditions of electromagnetically induced transparency (EIT) [Fleischhauer05]. In EIT, a strong laser (control) field addressing the  $|s\rangle \rightarrow |e\rangle$ , induces a spectral transparency window for a weak probe (or single photons) resonant to the  $|g\rangle \rightarrow |e\rangle$  transition, in an otherwise opaque medium. The probe pulse travels at much reduced speed in the form of a coupled excitation of light and matter called spin-wave. By ramping down the control field, the quantum state of the probe is mapped onto atoms as a collective atomic excitation. When the control field is turned back on, the quantum state of the probe can be retrieved with high fidelity. This memory protocol has been realized in a variety of experiments to store light at the single-photon level [Choi08, Nicolas14]. A recent review on quantum memories can be found in [Heshami16]. However, an ensemble of atoms is usually limiting the achievable non-linearity.

**Rydberg atoms** – In this approach, atoms are excited to a Rydberg state (with a high principal number  $n \sim 100$ ). This generates dipole-dipole interactions between two Rydberg atoms creating Rydberg excitation blockade [Lukin01] which prevents Rydberg excitation of other atoms within a blockade radius. Strong optical nonlinearities can be generated in this system [Pritchard10, Gorniaczyk14, Han10].

Recent advances in clean room fabrication have made it possible to combine atoms and nanophotonics into an integrated system. In this context, we already mentioned one such effort - use of micro- and nanoscopic cavities for cavity QED experiments. Here, we introduce a relatively new approach, in the name of Waveguide-QED, which will be the specific focus of this thesis.

## Waveguide QED

As the name suggests, it involves light-matter interaction via a waveguide. Light, in the waveguide, is confined in micro- or nanoscale dimensions and hence the mode area  $A$  is reduced to wavelength or subwavelength scale. This leads to an enhanced atom-photon

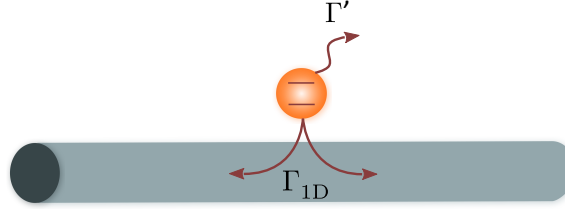


Figure 0.2 – Illustration of 1D nanoscale waveguide QED system: An atom decays into the waveguide with a coupling rate  $\Gamma_{1D}$  and into all other channels with a decay rate  $\Gamma'$ . The coupling to the waveguide is given by the ratio  $P = \frac{\Gamma_{1D}}{\Gamma'}$ .

interaction probability  $p \approx \lambda^2/A$ . This implies that a significant fraction of the power, guided by the waveguide, is absorbed by the atoms.

Waveguide-QED systems provides a robust and versatile platform for experiments in quantum information science and technology, chiral quantum optics [Lodahl17], quantum nonlinear optics, quantum many-body physics arising from long range ordering of spins and so on. There are also theoretical proposals [Zheng13, Paulisch16] for universal quantum computation in waveguide-QED systems.

There are several waveguide QED systems - plasmonic nanowires [Akimov07], quantum dot or diamond nanowires [Claudon10, Babinec10], 1D open superconducting transmission lines [Hoi12], photonic crystal fiber and waveguides [Okaba14, Arcari14] and optical nanofibers [Solano17c]. In this thesis, we focus on a specific 1D nanoscale waveguide-QED system - the optical nanofiber platform. We will introduce this platform here.

**Photonic crystal fibers** – We take a brief detour to look at another commonly-used waveguide QED system - photonic crystal fibers (PCFs) or hollow core fibers. These are special optical fibers fabricated in a way to have multiple holes or hollow regions across the fiber cross section. Light in certain well-defined wavelength bands is trapped in the air by a full two-dimensional photonic band gap of the cladding (silica). Light is confined to a dimension of few micrometers and is guided in a single mode. There are propagation losses and technical challenges when working with hollow core PCF. By loading cold atoms inside the hollow core of PFC, slow light and all-optical switching have been demonstrated in [Bajcsy09], and raman memory in [Sprague14].

## Nanofiber platform

Compared to photonic crystal fibers, nanofibers allow even tighter confinement of light at subwavelength scale. A major fraction of the light energy travels as an evanescent field outside the nanofiber. Only atoms in the vicinity can interact with the guided mode via the evanescent field. Compared to a cavity-QED system, a distinctive feature in such waveguide QED system is that the atoms are coupled here to a continuum of guided modes. Consequently, the difficulties of working with a narrow-band cavities

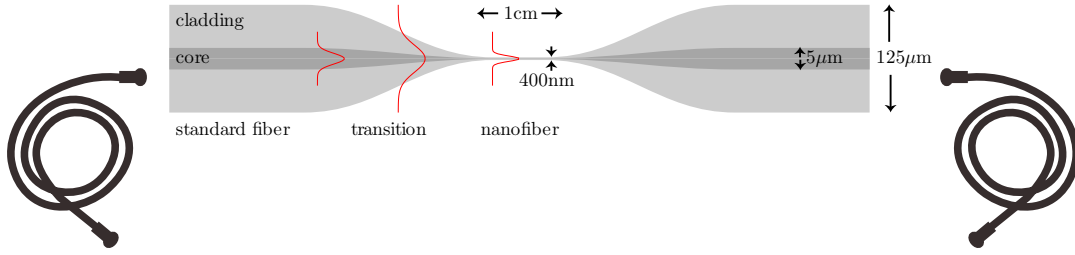


Figure 0.3 – An optical nanofiber in an all-fibered setting. The nanofiber, at the center, allows subwavelength confinement of light which results in intense evanescent fields. It is adiabatically coupled to standard single-mode fibers on both sides.

are avoided.

Because of the coupling to the waveguide, the spontaneous emission rate of the atom is enhanced  $\Gamma = \Gamma_{1D} + \Gamma'$ . The coupling to the waveguide can be characterized by the ratio  $P = \frac{\Gamma_{1D}}{\Gamma'}$ , where the decay rate into the guided mode is  $\Gamma_{1D}$  and into all other channels is  $\Gamma'$  (mainly into free-space  $\Gamma' \simeq \Gamma_0$ ) as illustrated in Figure 0.2.

Nanofibers, unlike some other nanostructures, do not require ultra-clean room facilities for fabrication. They can be fabricated in a regular lab environment though cleanliness has to be maintained at all levels [Ward14, Hoffman14b]. Nanofibers can be produced with ultra-high transmission and they withstand high optical powers.

Figure 0.3 illustrates an optical nanofiber connected to commercial fibers on both sides. From standard single-mode fibers, light is adiabatically coupled into a nanofiber, where it interacts with atoms via the strong evanescent field. Then, it is again adiabatically coupled back to the standard single-mode fiber on the other side. There is almost no transmission loss in the system. Light propagates as single-mode in the nanofiber.

Some typical characteristics of the nanofiber, involving our parameters, are listed below:

- **Tight confinement** of light to a subwavelength diameter allows strong light-matter interaction. In our case, a probe resonant with  $D_2$  line of cesium at wavelength 852 nm propagates in the nanofiber of diameter 400 nm. The atom-photon coupling strength is typically characterized by the ratio  $P = \Gamma_{1D}/\Gamma'$ , whose value amounts to a few  $10^{-2}$  in our experiment with trapped atoms. At resonance, one atom thus scatters  $P^2 \simeq 10^{-4}$  in intensity into the waveguide.
- **Large evanescent field** of ONFs is useful for coupling with matter- atoms, quantum dots, etc - as well as coupling of light into microresonators or other waveguides. About, 60% of light energy propagates as an evanescent field outside a nanofiber.
- **Long interaction length:** For a tightly focussed beam of light, the interaction distance is given by the Rayleigh length is  $L_R = \pi w_0^2/\lambda$ . If we focus a 852 nm beam to a waist of 1  $\mu\text{m}$  radius, then the interaction length is limited to about 4  $\mu\text{m}$ . Compared to free-space optics, ONFs allow us to interact strongly with

atoms over a relatively longer interaction length, given by the length of nanofiber waist. In our case, ONF waist is  $\sim 1$  cm long. With more advances in fabrication, the length of the waist could in principle be made longer to a few centimeters.

- **Configurability and Robustness** of nanofibers refers to the capability of low loss splicing to standard optical fibers and easy interconnection among fibered components. This allows transmission of optical signals without much loss, which will be crucial for building all-fibered quantum technologies. The flexibility of nanofiber even allows it to be bent into a knot with small radius of few millimeters which can then be used like a cavity.

In 2002, there were proposals from Hakuta and co-workers [Balykin04, Patnaik02] to interface atoms with the evanescent field of a nanofiber. First experiments in USA by S. Spillane *et al.* [Spillane08] and by S. Hendrickson *et al.* [Hendrickson09], with warm atomic vapors demonstrated nonlinear effects that could be achieved because of the high intensity of a tightly confined beam in a nanofiber. The experiments gave evidence of the saturation effects at low powers (nW) compared to saturation effects in a free-space configuration.

The first experiments with cold atoms were done by probing the atomic cloud with resonant light in the nanofiber. It was carried out by A. Rauschenbeutel [Sagué07] in Germany/Austria. The modified spontaneous emission rate of atoms and effect of surface interactions were studied by collecting the MOT fluorescence. They were carried out by K. Hakuta in Japan [Nayak09], and S. Chormaic [Morrissey09] in Ireland.

In 2010, the atoms were first trapped in nanofiber vicinity by A. Rauschenbeutel's group [Vetsch10]. Following it, a compensated nanofiber trap was implemented by J. Kimble's group [Goban12]. Since then, more groups across the world have been using nanofibers for interfacing with atoms. To mention some recent experiments in last few years - demonstration of memory for nanofiber-guided light by interfacing with cold atoms in our group [Gouraud15] and with trapped atoms [Sayrin15] (A. Rauschenbeutel's group), showing sub-Poissonian atom number distribution [Béguin14], collective spin states for trapped atoms [Béguin17] and coherent backscattering from 1D atomic arrays [Sørensen16] (J. Appel's group in Denmark), large Bragg reflection in one-dimensional atomic chains close to a nanoscale waveguide demonstrated in our group [Corzo16], cavity QED experiments performed using Bragg mirrors on both sides of a nanofiber [Kato15] (T. Aoki in Japan), measurement of trap frequencies [Solano17b] and alignment-dependent decay rates [Solano17d] and demonstration of super- and sub-radiance [Solano17a] in nanofiber trapped atoms (L.A. Orozco and S. Rolston group in Maryland USA).

Atoms trapped close to the vicinity of a nanofiber is a novel waveguide QED platform. On this platform, one of our goals is to implement quantum information protocols. This is motivated by the availability of high optical depth (OD) in the trapped ensemble of atoms, where OD is defined as  $-\ln\left(\frac{I}{I_0}\right)$  with  $I_0$  and  $I$  being the light beam intensities before and after the optical medium. Also, since the atoms are held down at the lattice sites, potential long coherence times of the quantum state is possible. This will manifest in the form of high efficiency and long lifetimes of the implemented memory protocols. There is another cold atoms experiment (elongated MOT with large number of atoms and OD) in our team and the plan is combine the two experiments.

Single photons generated from one can be stored in the other and vice versa. Then it will be possible to demonstrate entanglement of the two remote atomic ensembles, a step towards hybrid quantum networking. The other objective is to make use of the spatial ordering and long range interactions of atoms in 1D chains to observe interesting many-body effects emerging from optical forces and dipole interactions.

In our team, as a first experiment, we demonstrated memory for tightly guided light in a nanofiber with cold atoms in the vicinity of the nanofiber. This is when I joined Julien Laurat's quantum networks team. We prepared and soon implemented the dipole trap where atoms are trapped in two 1D chains close to the nanofiber. We spent time on optimizing and characterizing the trap. We observed 3-level coherent processes like EIT with trapped atoms. Around that time, we had to add filtering systems to our existing setup and make it more compact. We finally demonstrated Bragg reflection from this 1D lattice chains when the lattice period is made closely commensurate with the resonant wavelength.

**Thesis outline**— The first chapter introduces our tool - optical nanofibers. The propagation and polarization of nanofiber-guided light as well as fabrication techniques are discussed. The second chapter introduces the nanofiber-mediated dipole trap - the theoretical background as well as our particular compensated trapping scheme. The experimental part gives an overview of our setup - from light-atom interfacing to the dipole trap. The final chapter describes a full experiment with trapped atoms - Bragg reflection from 1D atomic chains. The theory and the experiment are described. Reflectance up to 75% was demonstrated with only 2000 trapped atoms. In addition, the reflection shows dependency on orientation of the probe polarization relative to the atomic chain - a signature of chirality in nanoscale waveguide QED systems.

# Chapter 1

## Optical Nanofibers (ONF)

Optical fibers are widely used for telecommunication as they allow transmission of light with relatively low loss over long distances. Since 1970s, the growth of telecommunication industry have made optical fibers cheap and easily available for more usage in science and technologies. Efforts to stretch them to thinner diameters have become quite popular for evanescent field coupling to quantum emitters, micro- and nanoscale structures and other applications like sensing. A paper published in Nature, 2003 [Tong03] demonstrated a simple, top-down process for fabricating low loss silica tapers. Though there was significant transmission loss compared to what was achieved soon after with flame-brushing techniques [Leon-Saval04, Brambilla04]; the loss was low enough to initiate more research in this direction.

This chapter is divided into two parts. In the first part, we explain the propagation of light in nanofibers. We describe in particular its single-mode guiding properties and the complex polarization structure of its mode. In the second part, we describe nanofiber fabrication. The technical aspects including the issues we faced, in the context of interfacing with cold atoms in ultra-high vacuum, will be detailed.

### 1.1 Propagation in optical nanofibers

Light propagates in fibers because of total internal reflection at the core-cladding boundary. We consider here step-index optical fiber where the refractive index changes from core to cladding in a discrete step, as illustrated in Figure 1.1. It has a core of radius  $\rho$  and refractive index  $n_{Co}$  and a cladding of radius  $\rho_{Cl}$  with slightly smaller refractive index  $n_{Cl}$ . The cladding is typically made of silica ( $n \sim 1.45$  for  $\text{SiO}_2$ ) and the core is made of silica doped with germanium or fluorine because of which the core has 1% higher refractive index than the cladding. The light in the core penetrates into the cladding as evanescent wave (exponentially decaying) and a thick layer of cladding is required for isolation of the guided light from the surrounding. The cladding diameter is usually  $125\mu\text{m}$ . When the diameter of core is small (typically  $5\text{-}10\mu\text{m}$ ) such that only a single mode is allowed to propagate, then the fiber is called a single-mode fiber. Fibers with large core diameters (typically  $50\text{-}60\mu\text{m}$ ) allow propagation of many modes together and are called multimode fibers. Each mode is characterized by its propagation constant  $\beta$ , group velocity, polarization and a transverse spatial

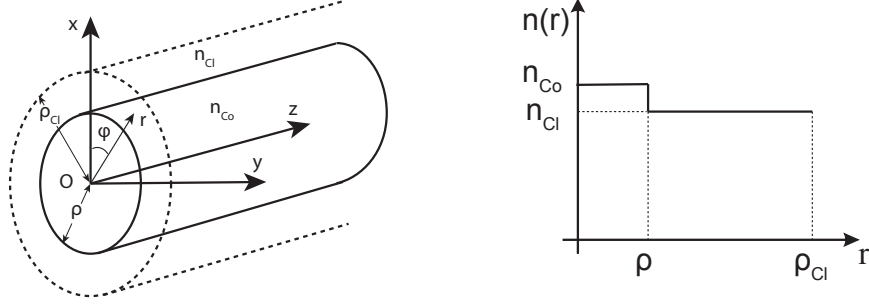


Figure 1.1 – Section of a circularly symmetric step-index fiber (left) represented in cylindrical coordinates. The  $z$ -axis coincides with the fiber axis of symmetry. The refractive index profile (right) of such a fiber is shown. The core of radius  $\rho$  has refractive index  $n_{Co}$  and the cladding of radius  $\rho_{Cl}$  has refractive index  $n_{Cl}$ .

distribution.

If a fiber is stretched to a subwavelength diameter (few hundred nanometers) the original core will almost vanish and the light will be guided in the (original) cladding-air boundary. An exception here compared to standard fibers, is a significant fraction of light propagates as evanescent field outside the nanofiber. The original cladding becomes the new core ( $n_{Co} = 1.45$ ) and the surrounding air is now the cladding ( $n_{Cl} = 1$ ) for the waveguide.

In this section, we present the general solution of fields in a step index fiber, which includes both standard fibers and nanofibers. Following it, we will focus on the mode propagating through a nanofiber, which is the fundamental  $HE_{11}$  mode.

### 1.1.1 Solution of fields in a nanofiber

One has to solve Maxwell's equations and derive the field solutions in optical waveguides. The derivation along with the mode functions can be found in [Snyder83, Yariv06]. A short summary of guided and radiation modes of the nanofiber is presented in [Le Kien05]. Separate solutions are obtained for each of the core and cladding regions. It turns out that the transverse field components are real and the longitudinal field components are imaginary with a  $\pi/2$  phase difference. Only in subwavelength waveguides like nanofibers, these longitudinal components are significant because of the variations of transverse components over a wavelength scale, as discussed later in subsection 1.1.3. For standard fibers or even micro-scale fibers, the longitudinal components are negligible.

The continuity of electric and magnetic fields at the core-cladding boundary helps to determine the unknown constants in the solution. The transcendental equation for the longitudinal propagation constant  $\beta$ :

$$\frac{J_{l-1}(h\rho)}{h\rho J_l(h\rho)} = \left( \frac{n_{Co}^2 + n_{Cl}^2}{2n_{Co}^2} \right) \frac{K_{l-1}(q\rho) + K_{l+1}(q\rho)}{2q\rho K_l(q\rho)} + \frac{l}{(h\rho)^2} \pm R, \quad (1.1.1)$$

where

$$R = \left[ \left( \frac{n_{Co}^2 - n_{Cl}^2}{2n_{Co}^2} \right)^2 \left( \frac{K_{l-1}(q\rho) + K_{l+1}(q\rho)}{2qaK_l(q\rho)} \right)^2 + \left( \frac{l\beta}{n_{Co}k_0} \right)^2 \left( \frac{1}{(q\rho)^2} + \frac{1}{(h\rho)^2} \right)^2 \right]^{1/2}$$

and  $J_l(x)$  and  $K_l(x)$  are Bessel functions of the first kind and modified Bessel functions of the second kind respectively,  $l = 0, 1, 2, \dots$  for modes of different order. The following quantities are introduced:

$$\begin{aligned} h &= \sqrt{n_{Co}^2 k_0^2 - \beta^2}, \\ q &= \sqrt{\beta^2 - n_{Cl}^2 k_0^2}. \end{aligned} \quad (1.1.2)$$

The propagation constant  $\beta$  is defined such that the solution of the electric and magnetic fields can be written in the general case as:

$$\begin{aligned} \vec{E}(r, \phi, z, t) &= (e_r \hat{r} + e_\phi \hat{\phi} + e_z \hat{z}) \exp[i(-\omega t \pm \beta z)] \\ \vec{H}(r, \phi, z, t) &= (h_r \hat{r} + h_\phi \hat{\phi} + h_z \hat{z}) \exp[i(-\omega t \pm \beta z)]. \end{aligned}$$

For any lossless mode to be confined to the core,  $\beta$  lies within the range  $n_{Cl}k \leq \beta \leq n_{Co}k$ , where  $k = \omega/c$  is the wave vector of the field in vacuum. By solving Eq. (1.1.1) numerically, one obtains discrete values for  $\beta$ , corresponding to a different propagating mode in an optical fiber. For each set of modes  $l$ , there are multiple solutions of  $\beta$  labelled by a mode index  $m$ .  $m$  is a positive integer numbering the  $\beta$  values in decreasing order i.e.  $m = 1$  corresponds to the largest value of  $\beta$  for a given value of  $l$ . The fundamental mode has the highest value of the propagation constant  $\beta$ .

The different modes are usually classified based on the properties of their field components. If the mode has no electric field in the direction of propagation ( $E_z = 0$ ), then it is called transverse electric ( $TE_{0m}$ ) mode corresponding to  $l = 0$  in Eq. (1.1.1). Similarly, if it has no magnetic field in the direction of propagation ( $H_z = 0$ ), then it is called a transverse magnetic ( $TM_{0m}$ ) mode corresponding to  $l = 0$  in Eq. (1.1.1). If the mode has all six non-vanishing components ( $E_r, E_\phi, E_z, H_r, H_\phi, H_z$  in cylindrical coordinates) then it is called a hybrid mode ( $HE_{lm}$  or  $EH_{lm}$ ), corresponding to  $l > 0$  in Eq. (1.1.1). The  $\pm$  signs in Eq. (1.1.1) represent two different sets of hybrid modes, the  $HE(-)$  and  $EH(+)$ . This difference lies in the contribution of  $E_z$  and  $H_z$  to the mode:  $E_z$  is larger (smaller) than  $H_z$  for the  $EH$  ( $HE$ ) modes. For standard fibers, we can approximate these modes with transverse and linearly polarized (LP) modes appearing in the context of field solutions in free-space. This is the weak guidance approximation and is valid only when the refractive indices of core and cladding are close to one another  $n_{Co} \sim n_{Cl}$ . Of course, one cannot make such approximation for the field modes of nanofiber and have to stick to the general solution.

We now focus on the guiding properties of a tapered optical fiber or nanofiber and estimate the diameter at which a tapered fiber becomes single-mode. Figure 1.2 gives the variation of effective refractive index  $n_{\text{eff}} \equiv \beta/k$  for different modes, as function of fiber core radius  $\rho$ . One can deduce the dispersion relation,  $\beta$  as a function of  $\lambda$ , from these curves. Note, when the diameter of a tapered fiber is not small enough, a number of modes are supported by it and its  $n_{\text{eff}}$  approaches the refractive index

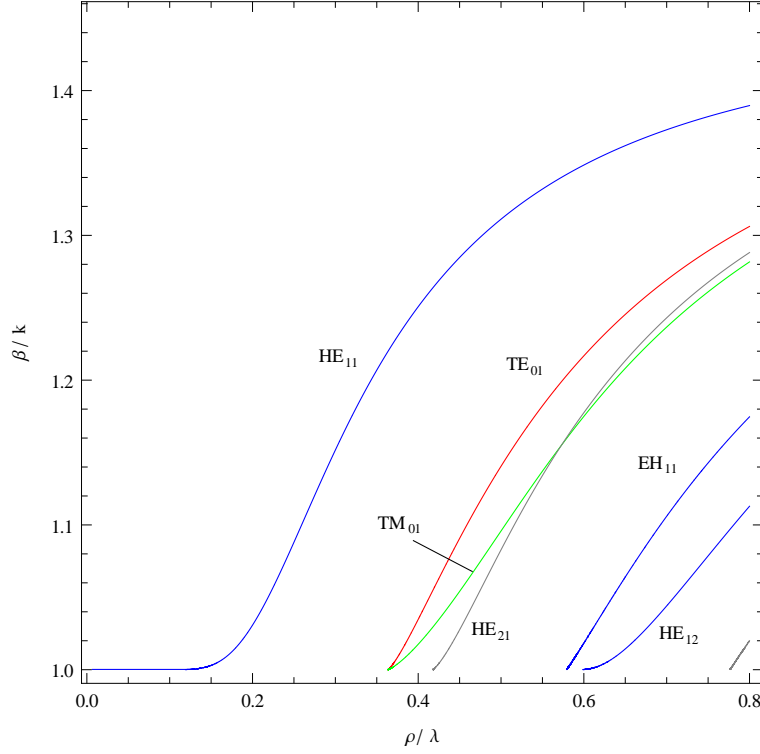


Figure 1.2 – Effective refractive index  $n_{\text{eff}} = \beta/k$  as a function of the fiber core radius - or equivalently as a function of  $V$ , with  $n_{Cl} < n_{\text{eff}} < n_{Co}$ . The different modes with different  $\beta$  can co-propagate except when  $V < 2.405$ , or here  $\rho/\lambda < 0.36$ . The nanofiber is then single-mode.

of silica  $n_{Co} \sim 1.45$  implying that the mode is guided mostly in silica. But with decrease in diameter, lesser number of modes and finally a single mode is guided in the waveguide with  $n_{\text{eff}}$  approaching 1, implying a large fraction of the modal energy is in the evanescent field outside the nanofiber.

In the limit of the diameter approaching zero only one mode - the fundamental mode  $\text{HE}_{11}$  is guided through the nanofiber. This gives the single-mode condition for the waveguide. It can be read as  $\rho/\lambda < 0.36$  from Figure 1.2. With the definition,  $V = 2\pi \frac{\rho}{\lambda} \sqrt{n_{Co}^2 - n_{Cl}^2}$ , the single-mode condition is:

$$0 < V < 2.405. \quad (1.1.3)$$

If the diameter of the nanofiber is reduced below this  $\rho/\lambda = 0.36$ , there is an optimal value  $\rho/\lambda = 0.23$  at which the intensity of evanescent field reaches maximum on the surface, as discussed in the next section. This optimal value corresponds to a diameter of 400 nm for  $\lambda = 852$  nm, resonant with  $D_2$  line of cesium. If the diameter is decreased further, the field intensity on the surface decreases till a point where the light will not be guided anymore and will be lost in the radiation modes [Sumetsky06].

**Energy distribution** – To find the fraction of light energy in the evanescent field, we have to integrate the  $z$ -component of cycle-averaged Poynting vector over a transverse

plane to obtain the guided power. The total guided power is given by:

$$P_{tot} = \frac{1}{2} \iint_{A_\infty} \text{Re}[(\vec{E} \times \vec{H}^*) \cdot \vec{z}] dx dy. \quad (1.1.4)$$

The integral can be expressed in terms of Bessel functions [Snyder83] for computing the power. Instead of integrating over all area, as in Eq. (1.1.4), if the integration is done only over the core area, then the guided power inside the core is:

$$P_{co} = \frac{1}{2} \iint_{A_{co}} \text{Re}[(\vec{E} \times \vec{H}^*) \cdot \vec{z}] dx dy.$$

The fraction  $\eta$  of total power guided inside the core is:

$$\eta = \frac{P_{co}}{P_{tot}}.$$

In our case, nanofibers with 400 nm diameter guides light with wavelength  $\lambda = 852$  nm. With these parameters, only about 40% of the input power is guided inside the core. Amazingly, the subwavelength diameter allows 60% of the light energy to propagate as an evanescent field outside the nanofiber.

### 1.1.2 Fundamental HE<sub>11</sub> mode in a nanofiber

Once the nanofiber diameter has reached the single-mode threshold value  $\rho/\lambda < 0.36$  or equivalently  $V < 2.405$ , only the fundamental HE<sub>11</sub> mode propagates in the nanofiber. Consider an electric field linearly polarized along  $y$  in free-space. When this is coupled into a nanofiber, the electric field distributions of HE<sub>11</sub> mode propagating in the nanofiber is shown in Figure 1.3. The free-space mode, which is Gaussian, loses its azimuthal symmetry in the  $x$ - $y$  plane in a nanofiber. Figure 1.3(c) shows a significant jump or discontinuity of the electric field intensity along  $y$  at the nanofiber surface. This can be explained as follows. Due to the sharp contrast in refractive indices between the silica core,  $n_{Co} = 1.45$  and the vacuum cladding,  $n_{Cl} = 1$  the normal (radial) component  $E_r$  of the electric field is discontinuous at the boundary but the tangential components  $E_\phi$ ,  $E_z$  are continuous. Along  $y$ , all the field is in radial direction resulting in the discontinuity at the boundary but along  $x$ , all the field is tangential to the surface and hence the field is continuous across the boundary. The electric field is said to be quasi-linearly polarized along  $y$  in the nanofiber because of the existence of longitudinal electric field component, which is detailed in subsection 1.1.3.

With approximations, it can be shown the radial component of the evanescent electric field (i.e. field outside the nanofiber) decays as,

$$E_i(qr) \sim c_i r^{-1/2} e^{-qr}$$

where  $r$  is the distance from the center of ONF,  $E_i$  is the  $i$ -th field component with  $c_i$  being its amplitude factor and  $q$  is given by Eq. (1.1.2). The decay length of the exponentially decaying part of the evanescent field is:  $\Lambda = 1/q_{11}$  where  $q_{11}$  is obtained from the knowledge of the propagation constant  $\beta_{11}$  of the fundamental mode HE<sub>11</sub>. In our case,  $\beta_{11} = 1.069$  (in dimensionless units) with  $\rho = 200$  nm and  $\lambda = 852$  nm.

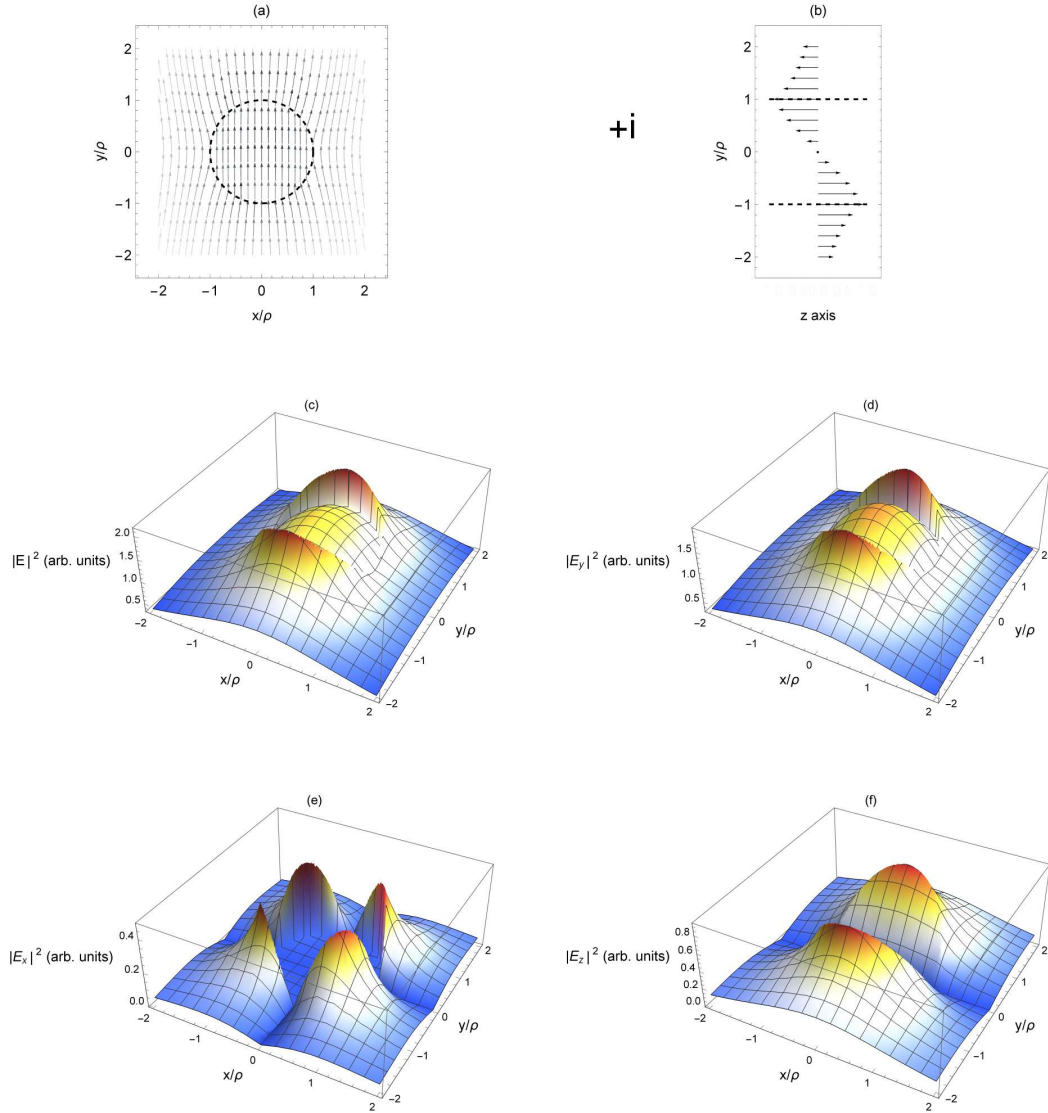


Figure 1.3 – Electric field distribution of the  $HE_{11}$  mode quasi-linearly polarized along  $y$  in a nanofiber of radius  $\rho = 200$  nm, refractive indices  $n_{Co} = 1.45$  and  $n_{Cl} = 1$  for  $\lambda = 852$  nm. (a) Transverse field components in the  $z = 0$  plane: field direction shown by arrows and field amplitude represented with gray scale; the core denoted with dashed lines. (b) Longitudinal field components on the  $x = z = 0$  line. (c) Electric field intensity, (d)  $X$ -component of field intensity, (e)  $Y$ -component of field intensity, (f)  $Z$ -component of field intensity in the  $z = 0$  plane.

Using this, we estimate an exponential decay length of 360 nm though the actual decay length will be smaller than this because of the  $r^{-1/2}$  dependence.

We already mentioned in our introduction that the atom-photon interaction probability scales as  $\sigma/A$  where  $\sigma = \frac{3\lambda^2}{2\pi}$  is the resonant absorption cross section of an atom and  $A$  the mode area. An “effective mode area” for nanofiber guided modes can be defined as the ratio of the guided power to the field intensity. Figure 1.4 shows the

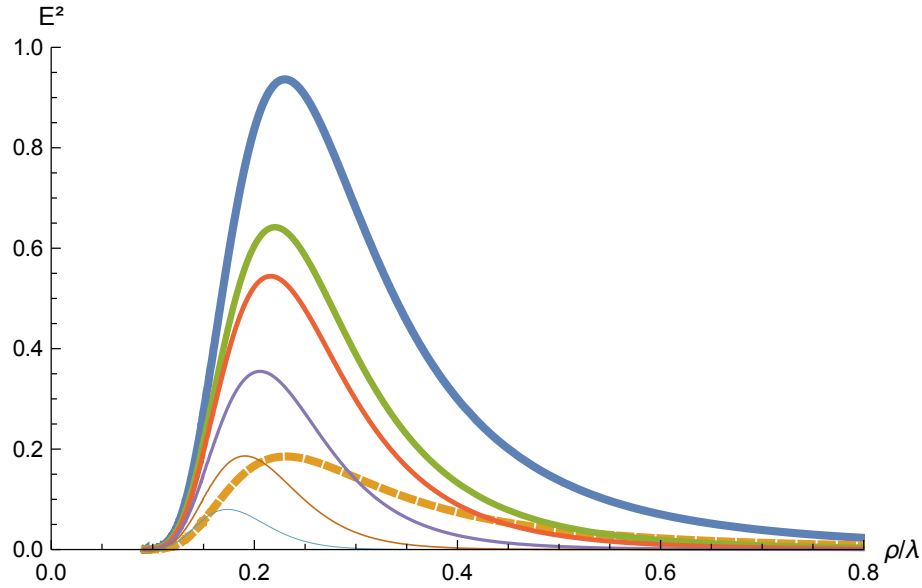


Figure 1.4 – Electric field intensity of the quasi-linearly polarized fundamental  $\text{HE}_{11}$  mode given as a function of the fiber radius for different positions close to the fiber, in units of the inverse maximal atomic scattering cross section  $\frac{1}{\sigma} = \frac{2\pi}{3\lambda^2}$ . The solid lines are for positions along the quasi-linear polarization axis, from thicker lines to thinner lines at distances  $0, \rho/6, \rho/4, \rho/2, \rho$  and  $2\rho$  from the surface. The dashed line is for a position along the orthogonal direction, on the fiber surface. The maximal electric field intensity at the fiber surface occurs at an optimal radius  $\rho = 0.23\lambda = 196$  nm.

electric field intensity as a function of the fiber radius for different positions in the nanofiber vicinity. The plot shows from thickest line to thinnest line this effective area can be as small as the scattering cross section (i.e.  $\sigma/A$  is close to unity for thickest line and  $\sigma/A \sim 1/20$  for the thinnest line). The maximal electric field intensity on the fiber surface is obtained for an optimal radius  $\rho = 0.23\lambda = 196$  nm. For other distances  $\rho/6, \rho/4, \rho/2, \rho$  and  $2\rho$  from the fiber surface, the maximal field intensity is found at  $\rho/\lambda = 0.220, 0.216, 0.206, 0.191, 0.173$  respectively. Similarly, on the orthogonal direction (dashed line) the maximum of the field intensity occurs at  $\rho = 0.232\lambda = 198$  nm on the fiber surface.

### 1.1.3 Chirality in nanophotonic systems

The longitudinal field component for the propagating modes of a nanofiber is significant and has a  $\pi/2$  phase-shift relative to the transverse field components. This is because of the confinement of light transversally to its propagation direction and this effect is prevalent in several nanoscale systems - photonic nanostructures, nanoscale waveguides, microresonators and so on. This longitudinal field component in the context of nanophotonics has led to an interesting phenomena with potential applications under the name - chiral light-matter interaction [Lodahl17].

Consider a strongly focused beam of light confined in nanostructures of wavelength  $\lambda = 2\pi/k$  where  $k$  is the wavenumber and  $\omega$  the angular frequency, that propagates

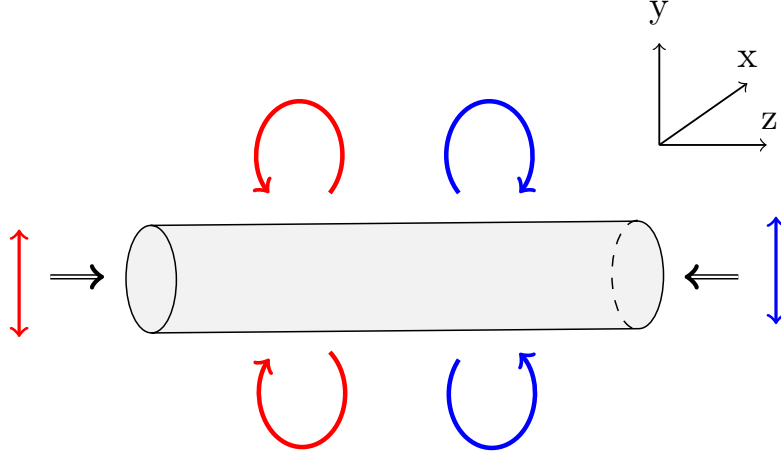


Figure 1.5 – Elliptical polarization of the electric field in the nanofiber vicinity. Here the guided mode is quasi-linearly polarized along  $y$ . The polarization rotates in opposite directions for  $y > 0$  and  $y < 0$  for a given propagation direction. Now, if this propagation direction is reversed the direction of polarization rotation for  $y > 0$  and  $y < 0$  is also reversed. This ellipticity of  $\vec{E}$  in the evanescent field therefore depends on the propagation direction and this phenomenon is called spin-momentum locking.

along  $\pm z$ . The electric field is  $\vec{E}_{\pm}(\vec{r}, t) = \vec{\mathcal{E}}_{\pm} \exp[-i(\omega t \mp kz)] + \text{c.c.}$ , where  $\vec{\mathcal{E}}_{\pm}$  is the complex amplitude,  $\vec{r}$  is the position vector,  $t$  is the time. Assuming a slowly-varying amplitude along  $z$  and applying Gauss's law  $\vec{\nabla} \cdot \vec{E} = 0$ :

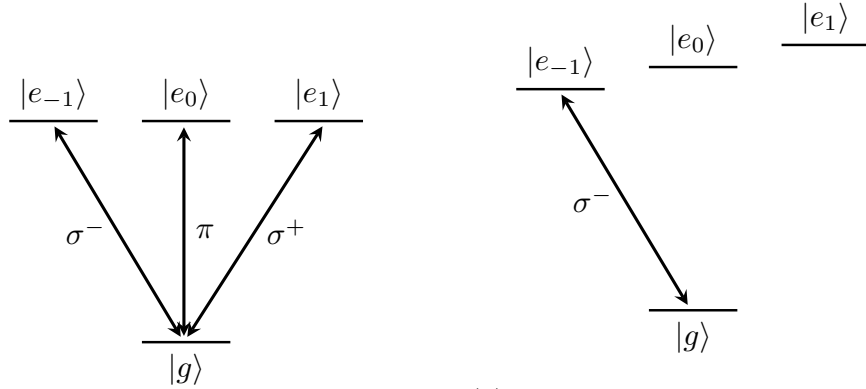
$$\mathcal{E}_{\pm, z} = \mp \frac{i}{k} \left( \frac{\partial \mathcal{E}_{\pm, x}}{\partial x} + \frac{\partial \mathcal{E}_{\pm, y}}{\partial y} \right).$$

The longitudinal and transverse components are comparable only when the latter varies over a length scale of  $1/k = \lambda/2\pi$ . The  $\pm\pi/2$  phase of  $\mathcal{E}$  implies that even a linearly polarized input becomes elliptically polarized in the strongly confined region and that sense of rotation of  $\vec{E}$  depends on the propagation direction  $\pm z$ . For an input, linearly polarized along  $y$ , the complex polarization structure of the field in a nanofiber is shown in Figure 1.5. The electric field of a nanofiber is maximal in the  $x = 0$  plane outside the fiber. The polarization of the field is elliptical in this plane, rotating around the  $x$  axis in opposite directions for  $y > 0$  and  $y < 0$  subregions. Now with a reversal in propagation direction, the sense of polarization rotation in  $y > 0$  and  $y < 0$  is also reversed. Now along  $x$ , the longitudinal electric field component vanishes since there is no variation of the electric field along the tangent (to the surface). Thus, there is no elliptical polarization structure for  $x > 0$  and  $x < 0$  subregions.

The spin angular momentum density [Bliokh14] of the evanescent electric field is:

$$S_{\mathcal{E}} = -[i\epsilon_0/(2\omega)]\mathcal{E}^* \times \mathcal{E},$$

where  $\epsilon_0$  is the vacuum permittivity. The existence of  $\mathcal{E}_{\pm, z}$  leads to a transverse spin component in the  $x$ - $y$  plane that flips sign when the propagation direction is reversed. This link between the sign of the transverse spin and the propagation direction,



(a) With no external magnetic field (Zeeman sublevels are unsplit), the atoms will absorb a photon from left, in a same way it will absorb a photon from right. This is an example of reciprocal chirality.

(b) A magnetic field applied from left to right, in the figure, splits the Zeeman sublevels. As a consequence the atom will absorb a photon from left with a different strength relative to the absorption of a photon from right. This is an example of non-reciprocal chirality.

Figure 1.6 – Illustration of reciprocal and non-reciprocal chirality in nanofiber and similar waveguide QED systems.

known as spin-momentum locking - is a consequence of the time-reversal symmetry of Maxwell's equations. Therefore, the strong light confinement can lock the polarization of the light to its propagation direction, which can lead to propagation-direction-dependent emission, scattering and absorption of photons by quantum emitters. It can be useful for building optical devices such as isolators and circulators.

In last few years, many experiments have demonstrated this chiral light-atom interaction with possible applications in photonics-based quantum technologies. The directional spontaneous emission of photons by trapped Cs atoms into a nanofiber [Mitsch14a] has been used to realize a nanophotonic optical isolator where the direction of the resulting isolation is controlled by the internal spin state of the atoms [Mitsch14b, Sayrin15]. A similar experiment with gold nanoparticles on a nanofiber [Petersen14] has been used to realize a chiral waveguide coupler in which the ellipticity of the incident light determines the propagation direction. Other experiments use Whispering Gallery Mode (WGM) microresonators [Junge13] and make use of the atomic-state dependent directional coupling to realize a single-atom switch, optical circulator and router [Scheucher16, Shomroni14].

In our experiment, the atoms are placed in two 1D arrays close to the nanofiber. The spontaneous emission of atoms into the guided mode is symmetric in forward and backward directions if the input polarization is aligned orthogonal to the atoms. However, if the input polarization is aligned along the plane of the atoms, the emission is asymmetric i.e. the rate of forward decay is unequal to that of the backward decay. This is an example of chirality. This effect will be studied along with our atomic Bragg mirror realization and signatures of this effect will be shown in this context. Note, the chirality in our case is reciprocal since changing the propagation direction will not

change the coupling of atoms to the left and right propagating modes. The atoms will absorb a photon from left, corresponding to  $\sigma^+$  (or  $\sigma^-$ ), in the same way it will absorb a photon from right, corresponding to  $\sigma^-$  (or  $\sigma^+$ ), since there is no applied magnetic field and consequently Zeeman sublevels are unsplit. The situation is illustrated in [Figure 1.6a](#).

However, in presence of an external magnetic field, the component along the fiber axis  $z$  will cause Zeeman sublevel splitting, as shown in [Figure 1.6b](#). The atoms will absorb a photon from left, with a strength proportional to a linear combination  $\sigma^-$ ,  $\sigma^+$  and  $\pi$  transitions. It will absorb a photon from right with a strength proportional to a different linear combination  $\sigma^-$ ,  $\sigma^+$  and  $\pi$  transitions. The unequal coupling strength on both sides is induced by the external  $\mathbf{B}$  field. This is an example of non-reciprocal chirality.

In this first section, we have looked into nanofiber-guided mode and its propagation characteristics. We now turn to the details of optical nanofiber fabrication. An important part of this thesis work has been dedicated to this fabrication and its reliability.

## 1.2 Optical nanofiber fabrication

The nanofiber production bench (or pulling rig) in LKB was first set up by former PhD student, Baptiste Gouraud in our team [[Gouraud16](#)]. It is designed to produce tapers - microfibers and nanofibers in a clean environment. The pulling rig is in close proximity with the cold atoms setup for easy transfer of nanofibers into the vacuum chamber. During the course of my PhD, we broke or damaged nanofibers (while interfacing with atoms) quite a few times and each time we had to go back to fiber-pulling to obtain a ‘good’ nanofiber. I have spent a fair share of my time in fabrication. In this context, I would like to thank a fellow PhD student, Maxime Joos, who is also working with nanofibers in our neighbouring team at LKB, for his contributions and helpful discussions. We have implemented changes from time to time to our pulling rig for the better and they are explained in this section.

Fabrication of tapered fibers (including nanofibers) has been going on for ten or more years in the community and typically 90 – 95% used to be a benchmark number for high transmission. It is only in last few years that production of nanofibers with transmission  $> 99\%$  tapers have been demonstrated by some groups, for example ultra-high transmission tapers were obtained in [[Hoffman14b](#), [Nagai14](#)] by maintaining cleanliness at all levels and optimizing the taper shape. In addition, high-resolution imaging of Rayleigh scattering from a nanofiber for analyzing propagating modes in tapers [[Ravets13](#), [Hoffman15](#)] and precise estimation of diameter from modal interference [[Fatemi17](#)] are important ingredients to characterize the process. The fabrication process has been reviewed in [[Ward14](#)].

The fabrication principle is the following: a standard optical fiber is heated and pulled symmetrically from both sides at the same time. The heating softens the fiber and the pulling stretches it. This results in thinning of the part of the fiber, which has been heated up in the flame. If done in suitable conditions, one can obtain a profile, shown in [Figure 1.8](#), where the submicron waist is adiabatically connected via



Figure 1.7 – The nanofiber production bench. At the center, the fabrication takes place in a clean environment. On the left wall a fiber spool supplies commercial fiber required for fiber-pulling. Under the optical table, the hydrogen generator produces ultra-pure hydrogen essential for a clean flame during fiber-pulling. The entire process is controlled and monitored by a computer on the right.

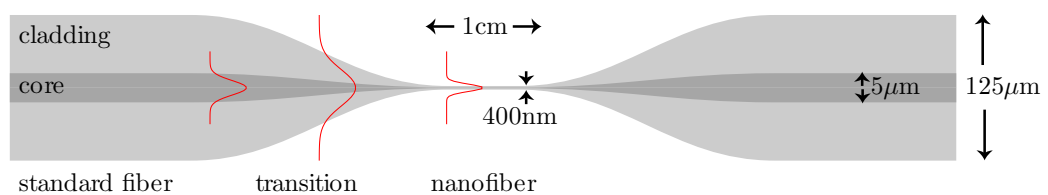


Figure 1.8 – A typical nanofiber (taper). Light coupled from standard single-mode fibers is initially guided in the core-cladding interface. The taper transition region enables light to be adiabatically coupled from the standard fiber to the nanofiber. In transition region, light can be multi-mode as it is guided both in core-cladding as well as cladding-air interfaces. At the nanofiber waist, light is single mode and it is guided in the cladding-air interface. A lossless taper or a nanofiber of almost unity transmission is engineered from standard fibers, by choosing an adiabatic trajectory, in a clean heat-and-pull fiber-pulling process.

a transition region to a standard fiber on both sides.

We describe the propagation of light in this system. The light coupled from left initially propagates in the unmodified single-mode fiber. The light is guided in the core and gets reflected at core-cladding interface. When guided light reaches the transition region, the decrease in diameter of the core reduces the mode area. However, there is no mode to cutoff since the light is already single-mode for the core-cladding guidance. The effective refractive index  $n_{\text{eff}}^1$  of  $\text{HE}_{11}$  mode decreases but is still greater than index of cladding  $n_{Cl}$  such that  $n_{Cl} < n_{\text{eff}} < n_{Co}$ . At around fiber radius  $\sim 20\mu\text{m}$  (for 800 nm fibers) the core is too small to maintain its guiding properties and the light escapes the core and leaks into the cladding but is reflected at cladding-air interface (it might be lost here if the tapering angle is not small enough). The light is now guided by the cladding-air interface and the effective refractive index satisfies  $1 < n_{\text{eff}} < n_{Cl}$ . In this region, the fiber is multi-mode for cladding-air guidance<sup>2</sup>. As the diameter decreases further, the higher order modes are cutoff one after the other. When the diameter reaches the cutoff for all higher order modes, the fiber is single-mode, see Eq. (1.1.3), and the light is guided in the fundamental  $\text{HE}_{11}$  mode. It continues to be in the same mode although the diameter of nanofiber might still decrease to reach the target diameter. On the other side of the taper waist, the light is guided back into the core (of the unmodified single mode fiber) via the transition region in the same way. If the fiber taper was designed and produced carefully, the transmission through it will be almost unity. This evolution of modes along the length of a taper has been demonstrated in [Hoffman15] by high-resolution imaging of Rayleigh scattering.

### 1.2.1 Design and Requirements

The taper transition region has to be designed in such a way that no guided light is lost from the waveguide. This is ensured by maintaining the tapering angle below a certain threshold value. The tapering angle here refers to the angle made by the tangent, drawn at the point, with the horizontal line. This threshold is given by the adiabaticity criterion [Black91] which requires the tapering angle  $\Omega(r)$  to be smaller than  $\Omega_c(r)$  where

$$\Omega_c(r) = \frac{r(\beta_1(r) - \beta_2(r))}{2\pi} = \frac{r}{z_t} \quad (1.2.1)$$

where  $r$  is the local fiber radius,  $\beta_1$  and  $\beta_2$  are the propagation constants of the fundamental  $\text{HE}_{11}$  mode and the first excited mode  $\text{HE}_{12}$  respectively and  $z_t$  is the local coupling length of these two modes. The argument is that the local taper length-scale  $r/\Omega(r)$  has to be larger than the coupling length  $z_t = 2\pi/(\beta_1(r) - \beta_2(r))$  between the fundamental and the first excited mode for lossless transmission of power in the taper. If at any point, the local tapering angle  $\Omega(r)$  approaches  $\Omega_c(r)$ , higher order modes will be excited in the taper and the light energy in that mode will be lost later when the taper reaches the cutoff radius for that mode. Following the adiabaticity criterion, the taper shape can be optimized in terms of pulling parameters to obtain

<sup>1</sup>Recall,  $n_{\text{eff}} = \beta/k$  where  $\beta$  is the propagation constant of a mode.

<sup>2</sup>This means, the fiber supports higher order modes but the guided light would still propagate in single mode if the tapering angle is small enough.

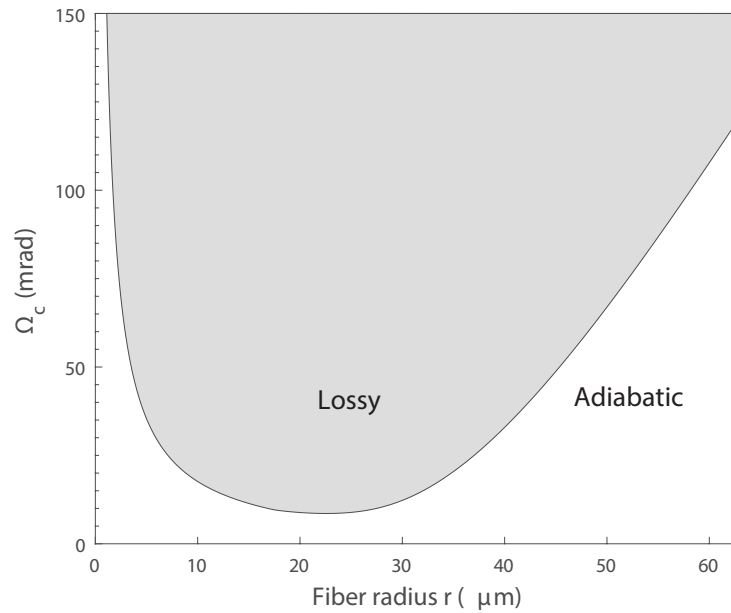


Figure 1.9 – Upper bound  $\Omega_c$  of taper angle as a function of fiber radius using the parameters for the fiber Thorlabs SM800-5.6-125 used in our experiment. The taper profile will be adiabatic as long as its taper angles are below this curve (in white region). If the taper angles are above this curve (in gray region) there will be transmission losses.

short and compact taper trajectories with ultra-high transmission as demonstrated in [Nagai14].

In our lab, we use a standard single-mode fiber at the operating wavelength of 830nm, Thorlabs SM800-5.6-125 (Fibercore), whose numbers are: Cladding diameter - 125  $\mu\text{m}$ , Core diameter - 5.8  $\mu\text{m}$ , Numerical aperture - 0.12, Cutoff wavelength - 778 nm, Refractive indices of core and cladding are 1.45625 and 1.45282 respectively.

For such a fiber, the upper bound  $\Omega_c$  of taper angle is calculated using a three layer model [Karapetyan12] and plotted as a function of fiber radius in Figure 1.9. The lowest value of  $\Omega_c$  is  $\sim 10$  mrad which occurs at about 20-25  $\mu\text{m}$  radius. In this region a transition from core- to cladding-guided mode takes place and hence a small angle needs to be maintained to ensure an adiabatic transformation. In all our trajectories, we choose taper angles much smaller than 10 mrad. Fiber pulling is studied theoretically in [Birks92]. We explain it briefly here.

Figure 1.10 illustrates a pulling step. An untapered fiber XY of radius  $r_0$  and length  $L_0$  being symmetrically pulled to a tapered fiber (XY stretched now) of waist radius  $r_w$  and uniform taper waist of length  $l_w$ . The taper transition has a length  $z_0$  on both sides and the taper shape is given by the local radius  $r(z)$ , where  $z$  is a longitudinal coordinate such that origin of  $z$  is at the beginning of each taper transition i.e.  $r(0) = r_0$  and  $r(z_0) = r_w$ . The taper extension  $x$  (which is a function of time  $t$ ) is the distance through which the taper has been stretched during pulling i.e., the difference of distance XY before and after the pull.  $L$  is the length of taper heated by the flame, called hotzone length, which can be a function of  $x$ .  $L_0$  is its initial value

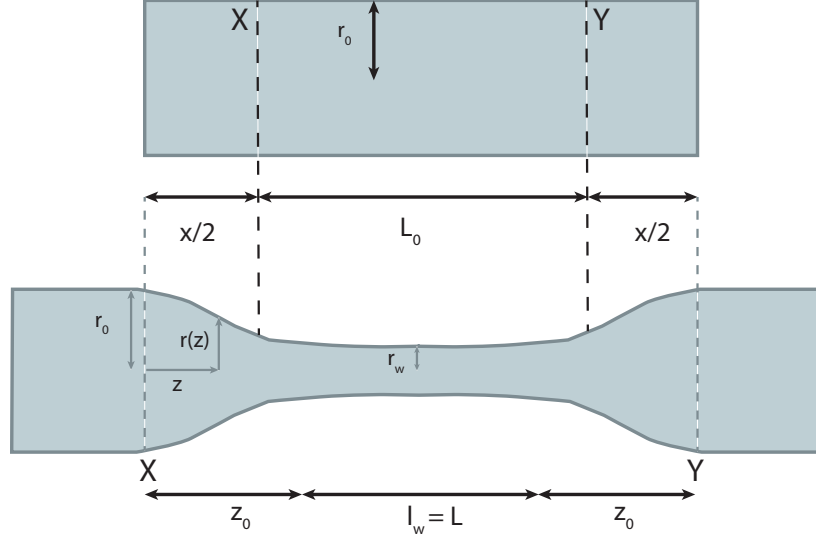


Figure 1.10 – An unstretched fiber XY of radius  $r_0$  and length  $L_0$  is symmetrically stretched/pulled to a tapered fiber with distance XY now longer than initial XY. The tapered fiber has identical taper transition  $z_0$  on both sides and radius of waist  $r_w$  with taper waist length  $l_w$ . The taper profile is given by the local radius  $r(z)$  as a function of longitudinal coordinate  $z$ .

at  $x = 0$ . At time  $t$ , the length of taper waist is equal to the hot-zone length at that time i.e.  $l_w(t) = L(t)$ .

Assuming  $L \geq 1$  and  $dL/dx \leq 1$ , which ensures the hotzone length does not overtake the preceding taper transitions, there are two fundamental equations governing a pulling process. The first one conserves volume in the stretched taper so that one can equate the instantaneous volume at time  $t$  to the volume at next instant  $t + \delta t$  i.e.  $\pi(r_w + \delta r_w)^2(L + \delta x) = \pi r_w^2 L$ . This gives the general form:

$$r_w(x) = r_0 \exp\left[-\frac{1}{2} \int_0^x \frac{dx'}{L(x')}\right]. \quad (1.2.2)$$

The second one compares lengths before and after a pulling step. This relates the taper transition length  $z_0$  to the taper extension  $x$  i.e.

$$2z_0 + L = x + L_0. \quad (1.2.3)$$

This relation holds true for successive pulling steps such that one can substitute  $z_0 = z$  and obtain the extension  $x(z)$ . From these two equations, Eq. (1.2.2) and Eq. (1.2.3), the complete taper profile  $r(z)$  can be determined.

We describe now how controlling the hot-zone length  $L(x)$  i.e. the movement of flame will determine the shape of fiber taper. There are two usual strategies:

1. **Constant hot-zone:** For  $L(x) = L_0$ , the solution is  $r_w(x) = r_0 e^{-x/2L_0}$ . Substituting  $z(x) = x/2$  we get a taper profile,

$$r(z) = r_0 e^{-z/L_0} \quad (1.2.4)$$

which is exponentially decaying. This is the case if the fiber is heated uniformly over a constant width and pulled symmetrically from both sides. However, the length of taper waist  $l_w \approx L_0$  is around 1 mm. This is not practical as the taper is short for interaction with atoms and the heating can be non-uniform as different parts of fiber are heated to different temperatures. Consequently, the taper shape cannot be very precisely controlled.

2. Linear hot-zone variation: For  $L(x) = L_0 + \alpha x$ , the solution is,

$$r(z) = r_0 \left[ 1 + \frac{2\alpha z}{(1 - \alpha)L_0} \right]^{-1/2\alpha}$$

$\alpha$  is a constant that determines the relative rates of hot-zone change and taper elongation. One can obtain various taper shapes based on the value of  $\alpha$ . A linear taper profile is obtained with  $\alpha = -0.5$ . This linear taper profile shape is widely implemented and so do we in our fabrication, because of practical simplicity.

**Flame-brushing technique** – The linear variation in hot-zone length required for the latter method can be obtained if the flame is made to travel in an oscillatory manner along a distance  $L$ , so that in each oscillatory cycle every element in the length  $L$  is heated identically. If the flame’s speed of travel is large compared to the speed of taper elongation  $dx/dt$  then the model described above is satisfied. The effective hot-zone length  $L$  will clearly equal to the flame’s distance of travel, so that  $L$  is known, controllable. Some of the first taper fabrications [Bilodeau88, Kenny91] were done with this method. The same technique can be put into practice with a variation if, instead of actually brushing the flame, the motorized pulling stages are made to move back-and-forth.

Then, the motion of stages can be broken down into two parts: first, the stages are moving apart with a pulling velocity  $v_f$  that stretches the fiber and second they are both moving together back-and-forth with brushing velocity  $v_b$  (relative velocity between stages is zero). This is much more practical and simpler than moving the flame burner. We implemented this technique in our setup, see Figure 1.11.

The nanofiber we manufacture is meant to be interfaced with cold atoms for quantum optics experiments. Hence it must satisfy the following criteria:

- High transmission  $\gtrsim 99\%$  and reproducibility: High transmission in nanoscale waveguides is important for quantum optics experiments, because the experiment is performed with a signal usually at the single-photon level for observing non-classical signatures. The fabrication of high transmission nanofibers must be reproducible for actually enabling us to interface such a nanofiber with cold atoms. This is based on the demands of our interface. Storing a high-transmission nanofiber for insertion in the vacuum chamber after a day or few days, is not practical, as dust particles will settle on it. Similarly, one cannot keep the vacuum chamber open and expose the vacuum components to ambient air-conditions for too long as it will also contaminate them. Therefore, we have practically some hours to produce a nanofiber with a high transmission and transfer it into the vacuum chamber within the same day. Thus, having a reproducible and reliable pulling process is important.

- Nanofiber target diameter 400 nm and waist length  $\sim 1$  cm: Very precise control of the diameter is difficult. Based on statistical dispersion of measured diameter by SEM (see [Figure 1.2.2](#)) our ONF diameter were found to be between 390 nm and 440 nm. The length of waist is measured to be 9-10 mm.
- High-power guidance of nanofibers in vacuum, particularly for 686 nm: One of the constraints in our experiments is that our nanofibers should be able to guide relatively large laser powers  $\sim 10$  mW at 686 nm under vacuum conditions. This is a crucial for setting up the dipole trap to trap atoms close to the nanofiber.

We have discussed the design and requirements of the fabrication process. Now, we look into its practical implementation.

## 1.2.2 Preparing, monitoring and characterizing the process

### Cleaning and preparing for fiber pulling

The fiber-pulling rig is placed under a laminar flow system to maintain a clean environment. In addition, gloves, hats, sleeves and proper clothes are used to prevent dust contamination, especially for fabricating a nanofiber that will be inserted in the vacuum chamber.

Preparing for a fiber-pull involves clean and careful handling of the fiber and different tools. The fiber is initially cleaned by sweeping a cleaning tissue moistened by isopropyl alcohol. Few centimeters of polymer jacket are stripped off the fiber and it is swept with moist cleaning tissue in a three-step cleaning process - first with isopropyl alcohol, then acetone and finally isopropyl alcohol. The acetone dissolves the remaining polymer pieces on the fiber. The fiber is then clamped between the translation stages. The initial distance between the stages is kept just enough to allow gluing nanofiber onto the vacuum fiber holder at the end of pull. The flow is set to its minimal value during pulling otherwise we see the fiber vibrate during the pulling.

All the elements of the process, including motor for the translation stages and motor for moving the flame are controlled by a python interface (screenshot in [Figure A.2](#) of [Appendix A](#)). Before we start a fiber-pull, we check that the fiber is indeed clean by moving the stages back and forth while viewing it by a camera with a microscope objective. We call this a ‘fiber scan’. If there is a dust, we do tissue-sweeps with acetone followed by isopropyl alcohol and repeat the fiber scan. This may have to be done recursively a few times until no dust is visible on the fiber. When we are ready, the fiber-pulling process is activated. This involves raising the flame to a desired height by triggering at the flame motor. After a time lag, the motor for stages are triggered and flame-brushing commences. The pulling process can last from few minutes to almost half an hour depending on the chosen trajectory. The fiber is monitored using cameras with/without microscope objective. The transmission of a laser source through the fiber is also monitored, as shown in the following.

### Monitoring the transmission

Recording of transmission through a fiber in real-time during pulling is one of the first indicators of how the pulling is going on. If the fiber breaks during pulling or if there

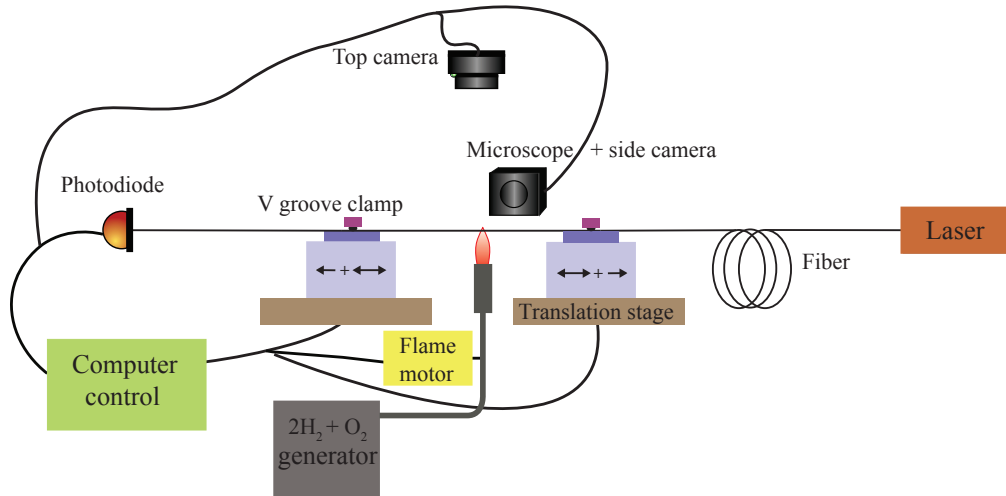


Figure 1.11 – Schematic of our flame-brushing rig. A standard optical fiber is clamped between the two translation stages. The motors for the flame and the translation stages are precisely controlled by the computer. While the fiber is being heated by a hydrogen-oxygen flame, the linear translation stages are set into a pulling as well as a back-and-forth ‘brushing’ motion. During the pulling, transmission through the fiber is monitored continuously by sending a laser beam. The fiber is monitored by the top camera and the side camera (with a microscope objective) during the process.

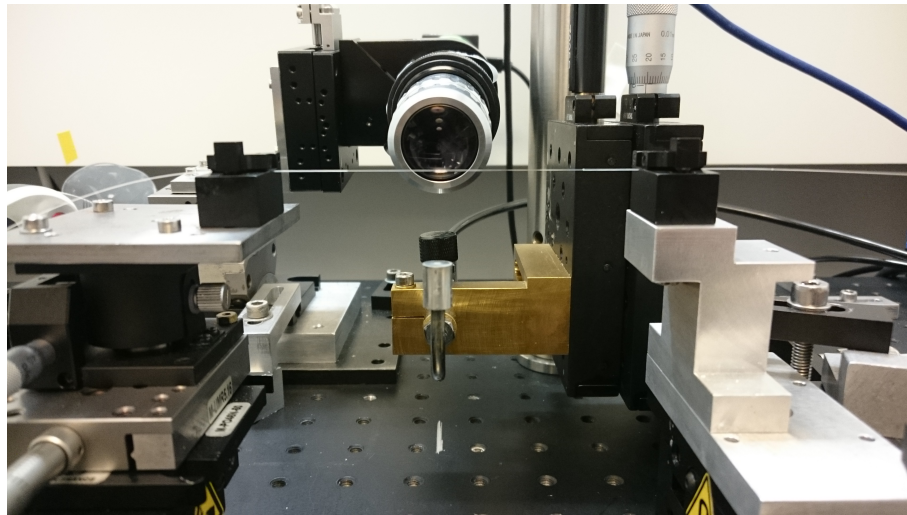


Figure 1.12 – Center of our fiber-pulling setup. A standard optical fiber, with its polymer jacket stripped off, is held between two “V” groove clamps, which are placed on translation stages (bottom). The position of left “V” groove clamp can be adjusted by using manual translation stages to align it with the right. The microscope, attached to the side camera is used for precise positioning of the torch tip and checking the fiber cleanliness before the pulling. The torch tip, with the flame lit, will be raised to a desired height when the pulling is activated.

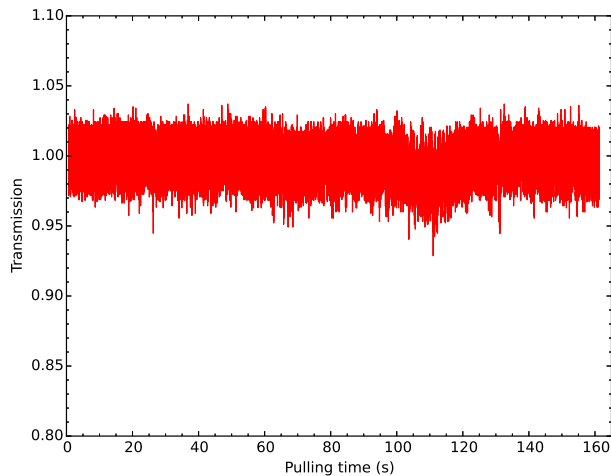


Figure 1.13 – Close to unity transmission for a pull obtained with the compact trajectory, mentioned in subsection 1.2.4.

is dust on the fiber the transmission drops or degrades. If the pulling parameters are far from their optimal values, the transmission can be quite low (less than 80 – 90%) as well. There are other factors like pulling trajectory and algorithm that significantly impact the transmission. Thus, obtaining a high transmission implies most of the critical aspects of fabrication are taken care of. In our setup, once the pulling is optimized we routinely obtain high transmission  $\sim 99\%$ . The pulling parameters, the trajectory/algorithm or in short the factors that led to this high transmission will be discussed later in subsection 1.2.3. An example of a high transmission pull is shown in Figure 1.13.

The transmission profile, shown in Figure 1.14, can also give us information on the diameter of fiber. As already discussed, higher order modes can be excited in the taper transition region, and owing to the variations of taper length during the pulling, they can interfere with the fundamental  $HE_{11}$  mode or among themselves to produce beat-notes, seen as oscillations in the transmission profile. Towards the end of a pull, these oscillations stop since the fiber has reached the cutoff diameter for all higher order modes i.e. fiber is single mode. These oscillations can be viewed as beat frequencies in spectrogram (a local, windowed Fourier transform of time-domain signals as a function of time), see Figure 1.14. Since the propagation constants of each mode are a function of fiber diameter, the beat-note frequencies, once identified as interference of few particular modes, can give us the fiber diameter in real time. What is easy to spot on the spectrogram is the last beat frequency (last rising curve) which implies the fiber has reached the single mode diameter. The oscillations and beat frequencies are usually visible for slightly lossy tapers since it is relatively easy to excite higher modes in them. Such oscillations or beat frequencies have even reported even for ultra-high transmission in [Hoffman14b].

Therefore, monitoring of transmission is a simple yet useful tool in nanofiber fabrication. In our setup, we usually send a 780 nm laser through the fiber for this purpose,

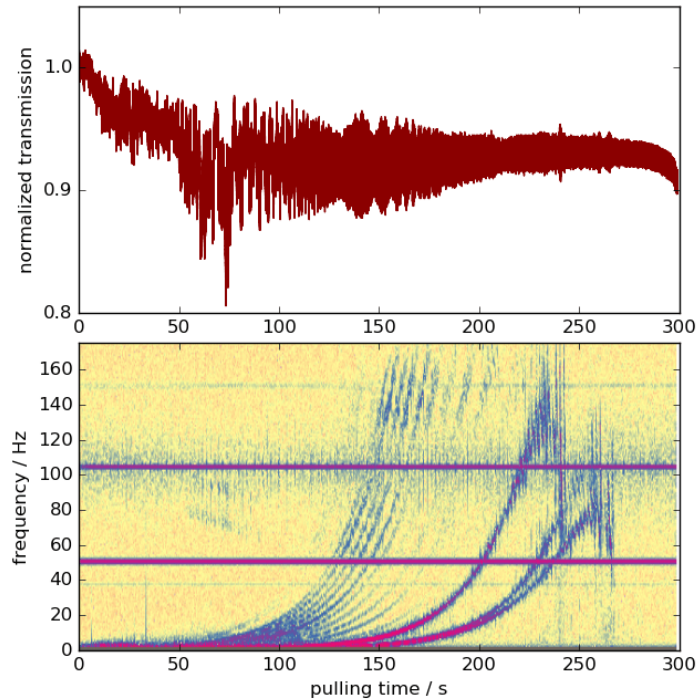


Figure 1.14 – Transmission profile (above) as well as the corresponding spectrogram (below) during a pulling process. The oscillations and the beat frequencies can clearly be seen in the transmission curve and the spectrogram respectively. The last beat frequency (seen as the last rising curve) on the spectrogram, corresponding to the interference of fundamental mode and the next higher order mode, implies the fiber has reached single-mode cutoff diameter.

which means the single-mode cutoff diameter is 570 nm.

### Characterizing the flame

The flame is produced using a stoichiometric mixture of hydrogen and oxygen (i.e.  $\text{H}_2 : \text{O}_2$  in a volume ratio of 2 : 1). The gases were initially generated in our lab by electrolysis of water using a generator from the company Hydrochaluveau. The gases produced were not pure and these impurities became later an issue in our experiment, as discussed in [subsection 1.2.3](#). We had to clean the generator periodically and replace the water.

Mass flow controllers (called flowmeters) are used for controlling the gas flow in order to produce a stable and reproducible flame. The gas mixture is dried and filtered before going through the flowmeter. The flow is set to a low value for the pulling process. Close to the torch tip a small device is installed to prevent the back-action of the flame. We have two flowmeters from two companies- Red-Y (smart GSC-A9SA-BB22) and Sierra (SmartTrak 50). It is important to note that the required flow also depends on the size of torch tip or nozzle used.

**Characterizing distance  $d$  from fiber to nozzle tip** – Aligning and positioning the flame with respect to the fiber is crucial for the success of fiber-pulling. The flame, which is controlled by a motor, has to be calibrated for that. Before the start of a pull, the flame is kept a few centimeters below the fiber. This relatively large distance allows lighting the flame without depositing soot on the fiber. Note, one must wait for some minutes for the gas flow and hence the flame, to be stable before starting a fiber-pull. One of the first tasks in pulling is to find a good combination of flow and the height at which the flame has to be raised for a well-functioning fabrication process. This task is accomplished in the following way. Starting from scratch, the lowest value of gas flow is chosen to produce a flame initially. This flow can be increased later by small steps as required. The initial flame height is chosen such that it is close enough to the fiber to soften it, yet far enough to not bend it or push it up. A practical way to do this is to choose a height at which the flame is just touching the fiber and a reddish-yellow glow on the fiber could be seen in dark conditions. This defines now a small interval ( $\sim$  a few mm) for the flame position to establish a controlled pulling process. The flame position needs to be fine-tuned to reach the optimal values for a reproducible, efficient (high transmission) pulling process. Because of an inherent unpredictability in the pulling process, the optimization has to be done step-by-step by monitoring the success of pulls at each step given by a set of parameters over a finite number of samples. Thus, the process of reaching the ‘best’ pulling parameters or condition is indeed time consuming.

For calibration of flame, the flame is turned off and a reference point is set by ‘touching’ the unstripped fiber with the torch tip. This is done by viewing in the side camera with microscope objective. ‘Touching’ here implies the nozzle comes in contact with the fiber and pushes it up by a quarter of its diameter (for purpose of standardization). Once calibrated, we can move the torch tip by a distance  $d$  relative to this reference point. However, the calibration needs to be checked on a regular basis since we found the initial position of the flame motor tends to drift away with time affecting the pulling process. In addition, by viewing the fiber from the top, it is ensured that the fiber is centered on the flame in transverse direction during pulling.

**Flame-width  $L_0$  measurement** – The effective flame width  $L_0$  is an experimental parameter used in our algorithm (subsection 1.2.4). Because of the flame shape,  $L_0$  is a function of the distance  $d$  from fiber to torch tip, as described above. We measure  $L_0$  by only pulling without brushing<sup>3</sup> i.e., by letting the stages move apart at a constant velocity  $v_f$ . This results in an exponential profile with a waist length  $L_0$ , see Eq. (1.2.4):

$$r_w = r_0 \exp\left(-\frac{t_h v_f}{2L_0}\right)$$

where  $t_h$  is the pulling time and  $r_0$  the unmodified radius of the fiber. We use our imaging system to measure the radius of the fiber waist at different times  $t_h$  during a fiber-pull. A sharp contrast for the fiber edges are created with respect to the background so that by image analysis one finds the fiber radius  $r_w$  at each time step. Since  $v_f$  has a fixed value, one can do linear fit when  $\ln(r_w/r_0)$  is plotted as a function

---

<sup>3</sup>Note, this is not the flame-brushing technique used in a regular fiber-pulling process.



Figure 1.15 – Side and top views of both nozzles used in our setup.

of pulling time  $t_h$  to extract  $L_0$  (see Figure A.1 in Appendix A). In the algorithm, with the aluminium nozzle (design presented below), we use  $L_0 = 0.63$  mm based on measurement values lying between 0.6-0.65 mm for following sets of flow corresponding to distance  $d$ :

Flow (Sierra in scc/min)	d (in mm)
110	0.83
130	1.92
150	2.15

During the course of my PhD, we have used two torch tips or nozzles Figure 1.15a. The first or old nozzle (see Figure 1.15b) was smaller and well-suited for fabricating nanofibers using our initial scheme (discussed in subsection 1.2.3). It has a single hole of 0.5 mm diameter. The produced flame has a 0.42 mm effective width with a flow of 280 mls/min (standard milliliters per minute) using the Red-Y flowmeter.

Figure 1.15c shows the bigger torch tip or nozzle. It is made of aluminium. It allowed us to implement the latter scheme, whose algorithm is presented in subsection 1.2.4 with great reproducibility and high transmission  $\gtrsim 99\%$ . The produced flame has a 0.6-0.65 mm flame width with a flow of 110-140 mLs/min using Sierra flowmeter. We will discuss these two schemes in subsection 1.2.3.

Recently, we have installed a new hydrogen generator (HyGen 200 from Claind) for ultra-pure  $H_2$  and mix it separately with ultra-pure  $O_2$  from a small oxygen tank. Both flowmeters are now used to control the flow of each of the gases separately before mixing them. We give a set of current flow parameters for pulling:

$H_2$ (Sierra in mL/min)	$O_2$ (Red-Y in mL/min)	d (in mm)	$L_0$ (in mm)
60	180	0.8	0.43

### Electron Microscopy validation

The theoretical limit of resolution of optical microscope is  $\sim \lambda/2$ , where  $\lambda$  is the wavelength of light used. To achieve better resolution, one has to go for electron microscope. Electrons, with sufficiently high kinetic energy (eg. accelerated through a high voltage), have much shorter wavelengths enabling a typical resolution on the order of nanometers. In a scanning electron microscope, a focused electron beam is

scanned over a surface to create an image. The electrons in the beam interact with the sample, producing various signals that can be used to obtain information about the surface topography and composition.

We use scanning electron microscopy (SEM) to characterize the nanofiber diameter, thanks to SEM facilities shared by IMPMC at UPMC. This process is destructive, which means that the fiber measured under SEM cannot be re-used for the experiment. It is useful though to get a quick estimate of the nanofiber diameter based on the statistics of measured samples (size  $\sim 10$  or  $20$ ). A sample SEM image of a nanofiber is displayed in ???. The technical details for measuring nanofibers with SEM is presented in [Appendix B](#). Once we have optimized the pulling parameters for ob-

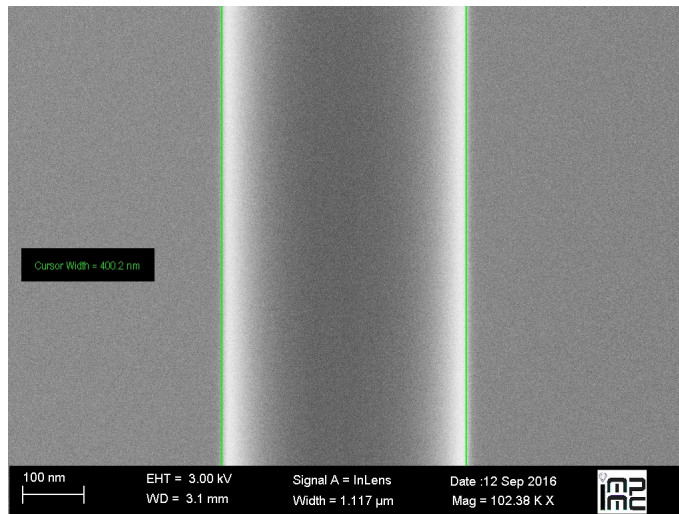


Figure 1.16 – Diameter measurement of a nanofiber with SEM.

taining reproducible, high transmission tapers, we go on to check our other requirement - diameter. We fabricate a series of tapers for a given set of parameters, sometimes another set of tapers for different parameters and glue them on a specimen stub meant for SEM measurements. The measurements give us an estimate on the diameter along with dispersion. Usually, the target diameter is reached with a  $\pm 5\%$  variation<sup>4</sup> from one fiber to the other. In addition, the fluctuations of diameter in the nanofiber waist for a given nanofiber have been measured up to  $\pm 10\%$  from one point to the other. We do not know the source of these diameter fluctuations in the nanofiber waist. The fact that we do not have a very stable (and uniformly heated) flame or nanofibers moving away from the flame during a pull could contribute to this dispersion. Recently, we have started to slightly move (what we call ‘jog’) the flame motor in small steps (tens of microns) during a fiber-pull towards the direction in which the nanofibers has moved. A few samples produced in this way have shown reduced fluctuations in diameter by an order of magnitude. More samples have to be tested and further investigation needs to be done before any conclusion.

Once, we are producing nanofibers of a desired diameter, verified by microscopy, we

<sup>4</sup>Note the number of tapers characterized by SEM is rather low for giving very significant error bars.

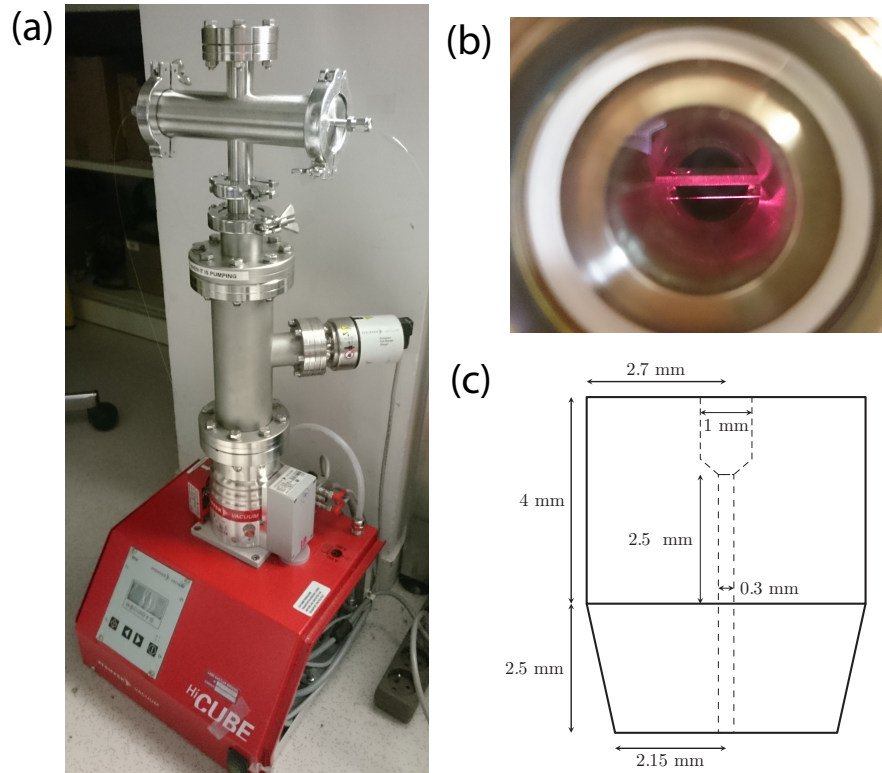


Figure 1.17 – Testing high-power handling capability. (a) The test chamber mounted on turbo pump, enabling it to reach high vacuum  $\sim 10^{-7}$  mbar conditions. (b) A nanofiber, inside this high vacuum test chamber, surviving 10 mW of 686 nm sent into it. (c) Updated drawing of vacuum fiber (teflon) feedthrough.

look into a crucial aspect of the nanofibers in the particular context of our experiment - their capability to handle high-power in high-vacuum conditions.

### Testing high-power handling capability of nanofibers in high-vacuum

The nanofiber easily survives when high power is sent into it in ambient air conditions. We tested with 1 watt of laser power at 852 nm, and there was no noticeable damage on our nanofibers (usually tested for 400 nm diameter fibers). In vacuum, when we send light into nanofiber, a tiny amount of light is always scattered at the ONF waist. This is Rayleigh scattering. However, if there are dust particles or other molecules in the taper, a part of light would get absorbed along with increased scattering from the surface. The absorbed light energy is converted into thermal energy at the nanofiber waist or taper transition region. This thermal energy is dissipated easily in air. However, due of lack of heat conduction in vacuum the thermal energy will melt or damage the nanofiber. Therefore, having a dust free enviroment and enforcing the cleanliness is critical for obtaining a nanofiber that can be used in ultra-high vacuum conditions.

The dipole trap around nanofiber (detailed in [chapter 2](#)) is set up by injecting a

combination of red-detuned and blue-detuned beams. Therefore, a nanofiber must be able to withstand 10 mW of blue-detuned light at 686 nm, 1 mW of red-detuned light at 935 nm in high vacuum conditions. We have implemented a system to test this power handling capability of nanofibers in vacuum. After a fiber pull, the nanofiber is collected in a holder and inserted in a test chamber (see Figure 1.17). Once high vacuum ( $\sim 10^{-7}$  mbar) is reached, 10 mW of blue-detuned light at 686 nm is launched into the nanofiber. The process is then repeated for a finite number of samples. The survival statistics give us an idea whether our current algorithm, pulling parameters and cleanliness aspects are all working together or if there are still improvements needed.

This crucial testing capability helped us mitigate the problem of breaking nanofibers in real vacuum chamber when 10 mW of 686 nm light was injected into it. It will be discussed in the next section.

### 1.2.3 Fabrication: A Review Story

After giving previously the general background of nanofiber fabrication, I will now describe the difficulties and various issues we faced in the context of fabricating nanofibers for interfacing with cold atoms, in a chronological order. This will help us understand the changes that have been made in the different aspects of fiber pulling to improve the overall process.

At the start of my PhD thesis, we had a working fabrication scheme for nanofiber production. This was developed by the former PhD student, Baptiste Gouraud. The pulling algorithm used was similar to that presented in the master's thesis of Christian Lutzler [Lutzler12]. This initial scheme helped us obtain nanofibers and interface with cold atoms for quantum optics experiments. The first experiment in the group was the demonstration of memory for the tightly guided light in an ONF [Gouraud15, Gouraud16]. In this experiment, the cold atoms moving around the nanofiber were interfaced with the guided mode via the evanescent field of the nanofiber. The next step was to trap atoms around nanofiber for large optical depth and long interaction times. Indeed, we implemented the dipole trap in the vicinity of a nanofiber with the expected characteristics. Using the trapped atoms, we performed Bragg reflection from the 1D chains of trapped atoms [Corzo16]. In between the two experiments we had to change the nanofibers twice in the experiment. Every time we insert a nanofiber into the vacuum chamber, we have to break the vacuum, dismantle a part of the experiment in order to open the chamber. In both cases, a big particle, referred here as 'dust', got stuck on the nanofiber surface scattering bulk of the guided light in the nanofiber and preventing any interfacing with atoms. Since then, we have been careful to keep the dispensers current not too high, typically between 3.5-4.5 A, as deemed necessary for the experiment. However, this initial scheme we used has had several limitations and the goal has been to move to an efficient scheme based on recent developments in the community.

The limitations comes from the algorithm which calculates the flame trips assuming a point heater source. It does not try to smoothen the taper profile and only one-linear-slope (we used a constant taper angle 1.55 mrad relative to the fiber axis) can be implemented in this trajectory. It worked for us since we had initially a small torch

Table 1.1 – Part number of materials for nanofiber fabrication.

<b>Equipment type</b>	<b>Company and part number</b>
Hydrogen-Oxygen generators	Hydrochaluumeau Hobby (old) and HyGen 200 (new) from Claind
Gas flow controllers	Vögtlin red-y smart GSC-A9SA-BB22 and Sierra SmartTrak 50
Gas drier (Peltier effect based)	M&C techgroup ECP-1000G
Gas filter	Swagelok SS-4F-K4-7 (7 $\mu\text{m}$ pore size) and SS-4F-K4-05 (0.5 $\mu\text{m}$ pore size)
Laminar flow clean air environment	Air C2, ISO 5 environment
Vibration isolated table and breadboard	Thorlabs, PBG52511 on sorbothane SB12B
2 linear translation stages and controller (for pulling and brushing)	Newport, 2 XMS100 and XPS-Q4
Linear translation stages and controller (for bringing/removing the flame from the fiber)	Thorlabs, Z825B and PT1
2 fiber clamps	Thorlabs, 2 T711/M-250 "V-groove" fiber holders
Fiber cleavers	Thorlabs S90W (quick and versatile cleave), and Fujikura CT-30A (precision cleaver)
Fiber stripper	Thorlabs T06S13 and FTS4 (Jonard)
Temporary fiber connections elements	Thorlabs, BFTU (fiber holder, now obsolete), 30126D1 (ferrule, obsolete), and ADAFC2 (mating sleeve)
UV led (for UV curing glues)	Thorlabs CS2010
Laser source (780nm) and photodetector	Thorlabs S1FC780 and DET100A/M
Cameras, standard or microscope objectives	IDS
Analog signal acquisition device	National Instruments USB-6008
Lens paper	Thorlabs, MC-5
UV curing glue	Dymax, OP-67-LS (for high vacuum) and Norland Optical Adhesive 65 (for regular use)

tip. The success rate of producing nanofibers was not high since around 30-40 % of them would break during fabrication. Sometimes the taper would go out of the flame during pulling owing to a small size of torch-tip diameter and that would explain the breaking of tapers. The ones that survived will have, on average, a typical post-pull transmission of around 90 %. Occasionally, (like 1 or 2 out of 15-20 fiber-pulls), one would obtain a taper transmission of around 96-97 %. In a nutshell, the fiber pulling was not reproducible and obtaining a taper of high transmission 99 % was rare.

We therefore incorporated a new scheme - based on work done by F. Warken and later improved by J. Hoffmann [Hoffman14a]. The algorithm allowed more control in producing a smooth taper shape but it involved using a bigger flame. We tried in the beginning with our small torch tip and had some success. We started to obtain 97-98 % transmission on a more regular basis. Soon, we designed a bigger torch tip enabling us to implement this scheme efficiently. The bigger torch tip or in other words a bigger flame width allowed the taper to be always inside the flame during the pull. With this algorithm, we initially implemented a one-linear-slope trajectory with better reproducibility and high transmission of around 98 %. We tested the high power handling capability of nanofibers by sending more than 20 mW of light at 852 nm and most of them, around 80-90 % survived. Some nanofibers burnt at higher power of around 50 mW. That did not make us concerned because we don't need to send power of that order in our experiment. In a nutshell, we expected nanofibers would survive 8 mW of 686 nm since most of them survived 20-30 mW of 852 nm. Unfortunately, in reality things turned out to be different.

Towards the end of the Bragg-reflection experiment, the nanofiber began to get loose and would start to move even though it was still glued onto the vacuum fiber holder on either side. The nanofiber had more like a swinging motion. In retrospect, the reason could be the nanofiber had not been tightened enough after the fiber-pull. Interestingly enough, whenever the MOT cloud was overlapped with nanofiber the nanofiber would stop to swing after some hours. Fortunately, this allowed us to finish the experiment. After the experiment, we went on to change this 'swinging' nanofiber for a new one but a problem appeared: nanofibers would melt in ultra-high vacuum when 8 mW of blue-detuned light at 686 nm is sent into it. In one of our attempts, we put a nanofiber inside the vacuum that did not melt, but developed a big, bright spot, when blue-detuned light was sent into it. Whatever caused this spot, it did not let us reach the usual optical depth with trapped atoms and hence the nanofiber was rendered useless. It took us some months to finally install a 'good' nanofiber in UHV, that is the current one.

To make a nanofiber survive inside vacuum is a challenge as it depends on various factors- some identified, some may not be clearly understood as yet. In our case, nanofibers would survive 20-30 mW of 852 nm but would break for 8 mW of 686 nm. Our guess is: since there is an absorption line of oxygen close to 686 nm, the blue-detuned light would get relatively absorbed more if there are residual oxides on the surface of taper causing a thermal damage in vacuum. Even if it was a valid reason for breaking, we could not get around this issue other than being as clean as possible at all levels. Also, improvements in algorithm and making a smoother, compact profile trajectory made the fabrication process efficient and helped in mitigating the problem.

Over a period of few months, we did a few things in parallel to improve the process.

First, the cleaning of generator for hydrogen-oxygen, which was not meant to produce ultra-pure gases required for delicate fabrications. Therefore, there were possible impurities present in the flame. So, we began to replace the water of the generator, on a more regular basis, with distilled water to make the produced gases as pure as possible. We began to remove the residual condensed water from the dryer on a regular basis so that the gases can be dried properly. We replaced the old gas particulate filters of  $7\ \mu\text{m}$  (pore size) with new filters  $7\ \mu\text{m}$  and  $0.5\ \mu\text{m}$  filters placed in series. In terms of pulling, we went for a compact trajectory having multiple linear slopes [Wuttke13b] as it would reduce the taper length and pulling time compared to one-linear-slope trajectories. Infact, this trajectory gave us great reproducibility and high transmission ( $\gtrsim 99\%$ ).

One last improvement that probably helped us, was a small change in algorithm. Previously, at turning points both the motorized stages would be stopped together and then restarted after a split second in opposite direction. Following the cue from J. Hoffman's algorithm, the stages were made to stop one after the other to maintain the pulling velocity  $v_f$  between them at turning points. More discussion on the pulling algorithm can be found in subsection 1.2.4.

There have been some difficulties with torch tips or nozzles. The nozzle we designed with aluminium had deposition of oxide over time. It was a source of dust reducing the transmission of fiber-pulls. We used Thorlabs fiber-polishing sheets to polish the top surface of the nozzle. This indeed helped us retrieve the high transmission of fiber-pulls. In addition, the nozzle holes got enlarged and distorted because of the heat, owing to low thermal resistance of aluminium. Probably, a large flame accidentally made once or twice deteriorated the nozzle tip. To circumvent this issue, we designed a brass nozzle. However, the quality of brass (available at that time in our workshop) would react with the gases in the flame and leave a black residue on the nozzle. This further reduced the post-pull transmission of nanofibers and we came back to using aluminium nozzle, a new one this time. We are careful not to make a big flame now and do polish the tip if/when necessary.

Enforcing all the steps carefully mentioned in the last two paragraphs, we managed to mitigate the problem, if not solve it. More and more nanofibers were surviving with 8-10 mW of 686 nm light than before. We carried out these high-power guidance tests in the test vacuum chamber. From a situation where only 10-20 % of nanofibers would survive, it eventually went up to fairly decent fraction of 70% survival in high vacuum conditions. We verified in tandem that the values of ONF diameter lie between 390 - 440 nm and that of waist length around 9-10 mm by SEM measurements.

#### 1.2.4 Pulling Algorithm

The algorithm is very similar to what is described in the thesis of F. Warken [Warken07] and J. Hoffmann [Hoffman14a]. The code, written in Matlab, outputs a file (called PVTM) to be loaded into our controller (XPS-Q4 from Newport) for communication with the motorized stages. The PVTM file contains position ( $x_1$ ), velocity ( $v_1$ ) of first motorized stage and position ( $x_2$ ), velocity ( $v_2$ ) of second motorized stage to be achieved within a specified time ( $T$ ), in the format  $[T\ x_1\ v_1\ x_2\ v_2]$ .

Starting from a taper waist, the adiabatic taper profile, following Eq. (1.2.1), is

constructed in a recursive algorithm till the standard fiber diameter  $125 \mu\text{m}$  is reached. In this algorithm, tapers of different taper angles can be joined to one another with slopes varying between 0.3 and 5 mrad. Finally, an exponentially decaying taper shape joins the linear profile to the nanofiber waist. The angle of starting exponential should match the taper angle of adjoining linear taper for a smooth taper profile.

The main points of the algorithm are listed here:

- Continuing our discussion from subsection 1.2.1, the fiber waist radius  $r_n$  at step  $n$  is related to the radius  $r_{n-1}$  at step  $n - 1$ . Using Eq. (1.2.2), we have:

$$r_n = r_{n-1} \exp\left(\frac{-t_{0,n}v_{f,n}}{2L_0}\right) \quad (1.2.5)$$

where  $t_{0,n}$  is the full-flame-sweep time through a point on the fiber,  $v_{f,n}$  is the pulling velocity at which the motors move apart, and  $L_0$  is the effective flame width.

- The fiber-pulling is assumed to be symmetric relative to the center of the flame and that the pulling velocities distributed inside the flame is assumed to be linear. Under these assumptions, the differential equation (see appendix of [Warken07]) can be solved to express  $t_{0,n}$  in terms of other known parameters:

$$t_{0,n} = \frac{L_0}{v_{f,n}} \ln\left(\frac{2v_{b,n} + v_{f,n}}{2v_{b,n} - v_{f,n}}\right). \quad (1.2.6)$$

- For a linear taper of taper angle  $\Omega$ , the first point, which in practice is the last pulling step for that section, the flame does not completely sweep through that point, because of which it is calculated by

$$r_{n+1} = r_{n-1} + L_0 \tan(\Omega/2)$$

while all other points in the taper are calculated by<sup>5</sup>

$$r_{n+1} = r_{n-1} + Lue_n \tan(\Omega)$$

where

$$Lue_n = L_0(v_b/v_{f,n-1} + 1/2) \ln(1 + 2v_{f,n-1}/(2v_b - v_{f,n-1})).$$

Also, the last point in the iteration has to be adjusted to reach the final radius  $r_0$  of standard fiber.

With these expressions the ratio  $r_n/r_{n-1}$  is given by the geometrical constraints imposed on the fiber. Typically, we fix the velocity of burner  $v_{b,n} = v_b$  (2 mm/s) and  $v_f$  can vary from  $10 \mu\text{m/s}$  to less than 1 mm/s.

To ensure a section in the taper region connects smoothly to the adjacent sections  $v_{b,n}$  is chosen such that  $v_{b,n} > v_{f,n}/2$ , which implies that the flame can reach previously thinned points. Once we experimentally establish the effective flame width  $L_0$ , fix  $v_b$ , specify the desired taper radius  $r_w$ , the length of taper waist  $L_w$  and taper angle  $\Omega$  for

<sup>5</sup>These expressions  $r_n$  can be derived from Eqns.(1.2.5) and (1.2.6)

the given fiber-pull, the algorithm calculates the necessary parameters and generates a PVTM file with computed positions, velocities that the motorized stages would reach at specified times.

During the course of my PhD, we focused mainly on two specific trajectories- a one-linear-slope trajectory and a compact trajectory with multiple linear slopes. The pulling process has been efficient and high transmission has been routinely reached for both of them.

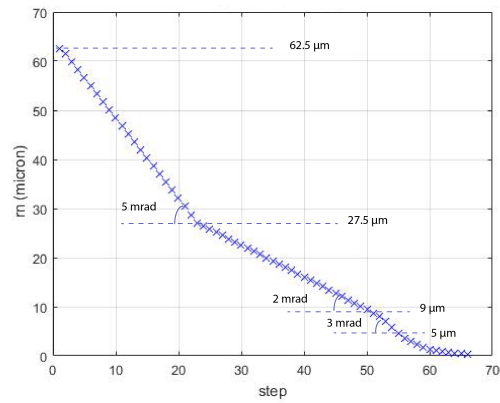
First, we describe the *compact trajectory* which has been used for producing the current nanofiber in experiment. The trajectory and the optimized parameters are:

- 5 mrad from cladding radius  $62.5 \mu\text{m}$  to a radius of  $27.5 \mu\text{m}$ , 2 mrad from  $27.5 \mu\text{m}$  to  $9 \mu\text{m}$ , 3 mrad from  $9 \mu\text{m}$  to  $5 \mu\text{m}$  and finally an exponential decay from  $5 \mu\text{m}$  to the nanofiber waist. The slopes are matched at  $5 \mu\text{m}$  junction i.e., the starting angle of exponential is 3 mrad. See [Figure 1.18a](#).
- Post-pull transmission for the current nanofiber in experiment is 99 %.
- Distance from fiber to nozzle tip,  $d = 0.83 \text{ mm}$  for flow = 110 scc/min during pulling, where  $d = 0 \text{ mm}$  corresponds to nozzle ‘touching’ the fiber.
- Pulling time 162.2s for target diameter 680 nm. Start brush delay of 11s is the estimated time before the start of pull during which the flame motor raises the nozzle to the height  $d$ . End brush delay of 1s is the estimated time before the end of pull during which the flame motors should lower the nozzle back to initial position.

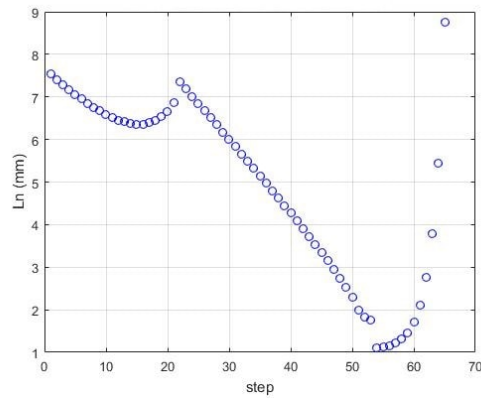
A higher target diameter 680 nm was set to produce nanofibers of 400 nm diameter. This was because of the following reason. In our old generator, there was a separate small slot for a liquid at its exit. In one instance, we had put ethanol instead of water there. This increased the flame temperature by few hundred degrees and as a result the nanofibers fabricated were getting thinner than their targeted values.

- The clamps on two translation stages are apart by about 15 cm and each stage can be moved by  $\pm 50 \text{ mm}$  about its mean position. We present the initial position of stages in our configuration:  $[-35, 6] \text{ mm}$ , before the start of the pull. This ensures at the end of the pull the translation stages would just provide enough gap ( $\geq 14.5 \text{ cm}$ ) to insert the vacuum fiber holder between the translation stages in order to glue the nanofiber onto the holder.
- Tightened by  $340 \mu\text{m}$ . This is done step-by-step by small increments of  $20 \mu\text{m}$  and the slackness of nanofibers monitored in camera. We found that tightening nanofibers typically between  $300\text{-}400 \mu\text{m}$  usually works fine and the right amount of tension is critical for our experiment. This additional tension can sometimes improve the post-pull transmission of a taper. However, tightening it beyond  $800 \mu\text{m}$  can break the nanofiber.

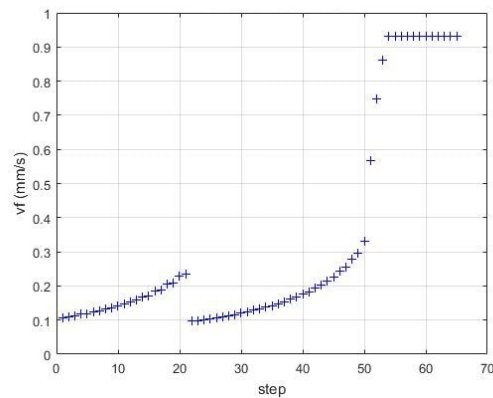
Next, we describe the *one-linear-slope trajectory* which had been implemented before the compact trajectory. The taper length of nanofibers in this case has been long relative to ones based on the compact trajectory.



(a) Evolution of taper radius as a function of pulling step. The different angles chosen for the compact trajectory are marked.



(b) Amplitude of moving flame as a function of pulling step.



(c) Pulling velocity as a function of pulling step.

Figure 1.18 – The evolution of pulling parameters as calculated by the pulling algorithm for the compact trajectory.

- 2 mrad from cladding radius  $62.5 \mu\text{m}$  to a radius of  $6 \mu\text{m}$  followed by an exponential decay to the nanofiber waist. The slopes are matched at  $6 \mu\text{m}$  junction i.e., the starting angle of exponential is 2 mrad.
- Typical post-pull transmission for nanofibers were around 98 %.
- Distance from fiber to nozzle tip,  $d = 2.15 \text{ mm}$  for a flow = 150 scc/min using the Sierra flowmeter. Later, we reduced the flow to 130 scc/min and worked at  $d = 1.92 \text{ mm}$ . Note, the measured flame width (0.6-0.65 mm) remained the same for both cases.
- Pulling time 566.8s for target diameter 410 nm. A corresponding delay is added before the start of pull during which the flame motor raises the nozzle to the desired height  $d$ .
- Similarly, initial positions (coordinates) of the two stages in our configuration: [-46, -16] mm, before the start of the pull to ensure that the nanofiber can be glued onto the holder at the end of pull.
- Tightened by  $480 \mu\text{m}$  at steps of  $20 \mu\text{m}$  while monitoring the slackness of nanofibers in camera. Since the nanofibers have been relatively loose or slack compared to ones obtained by the compact trajectory, more tension is applied in this case.

In conclusion, we have presented a full picture of nanofiber fabrication, including tools, techniques and finally the algorithm to generate user-defined taper shape. I have also summarized the difficulties of fabrication in the context of producing a nanofiber for light-atom interfacing in ultra-high vacuum. This is an ongoing work, not just in our group but also in the community, to develop protocols for survival of ultra-high transmission nanofibers in ultra-high vacuum and with atoms in a more deterministic, reproducible way.

### Chapter Conclusion

To summarize the chapter in few main points:

- The propagation properties of an optical nanofiber are described. When the fiber is small enough, below 600 nm in diameter, only the fundamental  $HE_{11}$  mode propagates with a significant 60% fraction of power in the evanescent field. It has a complex intensity and polarization pattern: the polarization is elliptical in general and varies at a subwavelength scale.
- The complex polarization structure of guided modes is due to the presence of the longitudinal electric field component. It has opened a new domain called chiral light-matter interaction in the context of waveguide-QED. This chirality has interesting applications in building quantum nanoscale devices. We observe chiral effect in the atomic Bragg mirror realization to be discussed in [chapter 3](#).
- The fabrication of nanofibers. We implemented the flame brushing technique: a standard, commercial fiber is pulled while heated by a clean flame. We obtain fiber tapers with high overall transmission  $\gtrsim 99\%$ . The nanofiber waist is a centimeter long with a 400 nm diameter, optimal for  $D_2$ -line resonant interaction ( $\lambda = 852$  nm) with cesium atoms close to the fiber surface.
- We review the different changes made in fabrication over a period of time to improve the pulling process. The issue of breaking nanofibers in vacuum with 686 nm light has been mitigated by following a series of steps towards cleanliness and changes in algorithm/trajectory.

In the next chapter, I will report how we interface cold atoms with a nanofiber and implement a two-color dipole trap where atoms are trapped in 1D arrays close to the nanofiber.

# Chapter 2

## A state-insensitive, compensated nanofiber trap

We have already discussed the first important tool of our experiment - the optical nanofiber. The other part of the experiment is interfacing the cold atoms with the nanofiber guided mode and trapping atoms in the nanofiber vicinity. For this purpose, atoms are first slowed down and collected in a magneto-optical trap (MOT) overlapped with the nanofiber. Then, they are cooled down further and loaded in a nanofiber-mediated dipole trap based on counter-propagating guided modes. We describe the whole process in details in this chapter as well as developing the necessary theoretical tools to understand them. In the first part of this chapter, we remind the theory of dipole potential and optical Stark shifts in the context of trapping atoms close to a nanofiber. We mention about our particular trapping scheme and how it can be useful in preserving the internal states of the atom. In the second part of this chapter, we implement this scheme experimentally. The experiment is detailed and the results showing typical trap characteristics are presented.

### 2.1 A two-color dipole trap in the evanescent field

In this section, we will briefly explore the theoretical aspects of a dipole trap. We first remind the dipole potential for a two-level atom and then extend it to a realistic multi-level atom. We will present general expressions for ac Stark shift experienced by an atomic state in far-off-resonance dipole traps. The nanofiber trap is an example of such a trap. We study the origin of different light-shifts in a nanofiber trap and how they can cause dephasing of a collective quantum state in the ensemble. Finally, we show how our particular state-insensitive, compensated scheme helps to cancel some of these shifts.

#### 2.1.1 Optical dipole potential and ac Stark shifts

We consider a two-level atom with ground state  $|g\rangle$  and excited state  $|e\rangle$ . Let  $\Delta = \omega - \omega_0$  be the detuning from the atomic resonance frequency  $\omega_0$ . Let us consider a

monochromatic electric field of the form:

$$\mathbf{E}(t) = \hat{\epsilon} E_0(\mathbf{r}) \frac{e^{-i\omega t}}{2} + c.c.$$

where  $\hat{\epsilon}$  is the unit polarization vector.

The interaction between the atom and this electric field  $\mathbf{E}(t)$  is given by  $H_{int} = \mathbf{d} \cdot \mathbf{E}$ . The dipole moment, expressed as  $\mathbf{d} = \alpha(\omega)\mathbf{E}$ , is induced by this external field  $\mathbf{E}$  and the polarizability  $\alpha$  characterizes the response of the atom to the applied field. We are interested in studying far-off resonance interactions i.e.  $\Delta \gg \Gamma$  where  $\Delta$  is the detuning from atomic resonance and  $\Gamma$  is the spontaneous decay rate of the excited state. From the interaction Hamiltonian  $H_{int}$ , if one calculates the force on the atom by this external electric field, two forces will show up in the equation. The first one, radiation-pressure force is dissipative and depends on the gradient of the phase of the field. This is, for example, responsible for cooling and trapping atoms in magneto-optical trap (MOT). The second one, optical dipole force depends on  $\Delta$  and the gradient of the field. It is dispersive and conservative in nature. Hence, it can be used to trap atoms at the focus of a laser beam or at crests and troughs of a standing wave.

The dipole force can be expressed as a gradient of potential, referred to as dipole potential. At the first order approximation, the dipole potential is given by:

$$V_{dip} = \frac{\hbar |\Omega(\mathbf{r})|^2}{4\Delta} \propto \frac{I}{\Delta}, \quad (2.1.1)$$

where the Rabi frequency  $\Omega(\mathbf{r})$  is defined as:

$$\Omega(\mathbf{r}) = -\frac{\langle g | \hat{\epsilon} \cdot \mathbf{d} | e \rangle E_0(\mathbf{r})}{\hbar}.$$

In terms of polarizability  $\alpha$ , an alternative form of dipole potential is:

$$V_{dip} = -\text{Re}[\alpha(\omega)] |E_0|^2 = -\frac{1}{2\epsilon_0 c} \text{Re}[\alpha(\omega)] I(\mathbf{r}).$$

To note, the dipole potential has a negative shift for red detuning ( $\Delta < 0$ ) and a positive shift for blue detuning ( $\Delta > 0$ ) and on resonance the dipole force vanishes.

An important parameter concerning dipole traps is the photon scattering rate, which is proportional to the power absorbed by the atoms since the absorbed power will be emitted in subsequent spontaneous emission processes to conserve energy. The scattering leads to heating and loss of atoms in the trap. Far off resonance, the scattering rate is given by

$$R_{sc} = \frac{P_{abs}}{\hbar\omega} \propto \frac{I}{\Delta^2}$$

We see the dipole potential, from Eq.(2.1.1), scales as  $I/\Delta$  whereas the scattering rate scales as  $I/\Delta^2$ . Therefore, for a desired potential depth, the scattering should be made as small as possible by increasing the detuning  $\Delta$ . The decrease in potential can be compensated by increasing the intensity. This will reduce the noise and increase the lifetime in a trap.

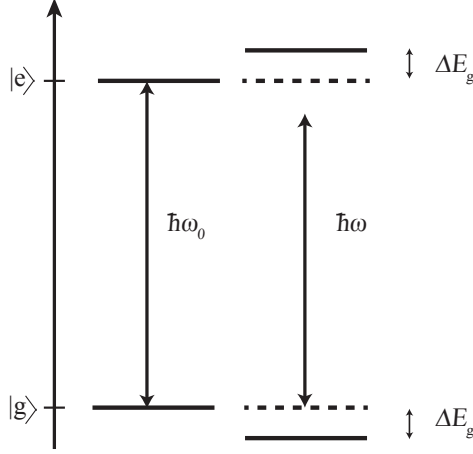


Figure 2.1 – Ac Stark shift in a two-level atom by a red-detuned light ( $\Delta < 0$ ), shifting  $|g\rangle$  down and  $|e\rangle$  up by equal amounts  $\Delta E_g$ .

The dipole potential, given by Eq.(2.1.1), for the two-level atom can be interpreted as optically induced Stark shift of the two-levels [Dalibard85]. The energy shift turns out to be opposite for  $|g\rangle$  and  $|e\rangle$  but by equal amounts as illustrated in Figure 2.1. The ground-state shift is given by:

$$\begin{aligned} \Delta E_g &= \frac{\hbar|\Omega(\mathbf{r})|^2}{4\Delta} = \frac{|\langle g|\hat{\epsilon} \cdot \mathbf{d}|e\rangle|^2|E_0(\mathbf{r})|^2}{\hbar} \left( \frac{1}{\omega - \omega_0} - \frac{1}{\omega + \omega_0} \right) \\ &= -\frac{2\omega_0|\langle g|\hat{\epsilon} \cdot \mathbf{d}|e\rangle|^2|E_0(\mathbf{r})|^2}{\hbar(\omega_0^2 - \omega^2)}, \end{aligned} \quad (2.1.2)$$

where the inverse detuning  $\frac{1}{\Delta} = \frac{1}{\omega - \omega_0}$  is replaced by  $\frac{1}{\Delta} = \left( \frac{1}{\omega - \omega_0} - \frac{1}{\omega + \omega_0} \right)$ . This is because for far-off resonance interaction, we must include the contribution coming from the counter-rotating term in the atom-field Hamiltonian  $H_{int}$ , outside rotating wave approximation (RWA).

We see, the ac Stark shift given by Eq. (2.1.2), happens to be a perturbation of second order (quadratic) in electric field. The first order shift  $\langle k|\tilde{H}_{int}|k\rangle$  for a non-degenerate level  $|k\rangle$  vanishes as the dipole operator only couples states of opposite parity<sup>1</sup>.

We can extend our formalism to a real multiple-level structure atom summing over contributions from all excited states, instead of contribution from one excited state as done for a two-level case. The energy shift (ac Stark shift) for the state  $|\alpha\rangle$ , characterized by quantum numbers  $F, m_F$ , is given by [Steck, Geremia06]:

$$\Delta E(F, m_F; \omega)_{|\alpha\rangle} = -\alpha_{\mu\nu}(F, m_F; \omega)_{|\alpha\rangle} (E_0^{(-)})_{\mu} (E_0^{(+)})_{\nu}$$

where the polarizability tensor  $\alpha_{\mu\nu}$  is a rank-2 tensor. It can be expressed as a sum of irreducible parts (under a transformation of rotation) of rank 0, 1 and 2. Using these

<sup>1</sup>Except in hydrogen, where degeneracy of opposite-parity states causes a first-order shift and hence a linear Stark effect.

properties, one can define an effective ac Stark shift Hamiltonian in Cartesian coordinates basis for an atom in the state  $|n J F\rangle$  [Deutsch98, Rosenbusch09, Lacroute12]:

$$\begin{aligned}
H_{stark} &= H_0 + H_1 + H_2 \\
&= -\alpha^{(0)} \mathbf{E}^{(-)} \cdot \mathbf{E}^{(+)} - i\alpha^{(1)} \frac{(\mathbf{E}^{(-)} \times \mathbf{E}^{(+)}) \cdot \mathbf{F}}{2F} \\
&\quad - \sum_{\mu, \nu} \alpha^{(2)} E_{\mu}^{(-)} E_{\nu}^{(+)} \frac{3}{F(2F-1)} \left[ \frac{1}{2} (F_{\mu} F_{\nu} + F_{\nu} F_{\mu}) - \frac{1}{3} F^2 \delta_{\mu\nu} \right]
\end{aligned} \tag{2.1.3}$$

where  $\alpha^{(0)}$ ,  $\alpha^{(1)}$  and  $\alpha^{(2)}$  are the atomic dynamic polarizabilities; their expressions and values (corresponding to cesium D<sub>2</sub> line) can be found in [Le Kien13, Goban15]. In this Hamiltonian, the mixing of energy levels of different hyperfine states have been neglected since typically the hyperfine splittings (hfs) are much larger than the ac Stark shifts i.e.,  $F$  is a good quantum number. A more rigorous approach treating the hfs splitting and Stark shift to be perturbations of same order is presented in [Le Kien13].

The scalar shift,  $H_0$  is independent of  $F$  (and  $m_F$ ). It is in general different for ground  $|g\rangle$  and excited states  $|e\rangle$ , so that a two-level  $|g\rangle - |e\rangle$  resonant transition will be driven out of resonance.  $H_1$  is the vector shift which induces a Zeeman-like splitting proportional to  $m_F$ . It can be interpreted as a ‘fictitious magnetic field’ which lifts the angular momentum degeneracy. It arises due to the ellipticity of the electric field. In the  $\sigma^{\pm}, \pi$  basis, vector shift is activated by  $\sigma^{\pm}$  and not by  $\pi$  polarization.  $H_2$  is the tensor shift and has quadratic dependence on  $m_F$ . In the  $\sigma^{\pm}, \pi$  basis, tensor shift is activated by  $\pi$  and combination of  $\sigma^{\pm}$  polarizations.

### 2.1.2 Dipole trapping with a nanofiber

We now turn to the principle of trapping atoms in the vicinity of a nanofiber. Subsequently, we will use the framework presented in the previous section to identify the trap decoherence mechanisms affecting a nanofiber dipole trap and how some of these issues have been addressed by our scheme (based on [Lacroute12]).

Unlike dipole traps in free-space configuration, the evanescent field traps require relatively low power owing to the strong confinement of light. Trapping atoms in the evanescent field of a nanofiber was proposed in [Le Kien04] using a two-color trapping scheme. We know the characteristic decay length of evanescent field is proportional to the wavelength of the guided mode and this allows creation of potential wells close to the nanofiber by using nanofiber-guided red-detuned and blue-detuned beams. The red-detuned light through the nanofiber creates a dipole attractive potential while the blue-detuned light, naturally of shorter decay length, creates a repulsive potential and prevents atoms from falling onto the nanofiber surface. Combining these two-colors and adjusting the power of dipole beams, a potential minimum can be created at a few hundred nanometers from the surface. This confines the atoms radially. Longitudinal confinement is achieved using a pair of counter-propagating red-detuned beams to create a 1D optical lattice along the fiber axis  $z$ . The trapping geometry will further depend on the choice of polarization of guided modes.

If the polarizations of the dipole beams are quasi-circular, the atoms will rotate around the fiber due to the rotational invariance of the configuration. However, if

the dipole beams are quasi-linearly polarized along  $y$ , see Figure 2.2, we break the azimuthal symmetry and the atoms can be confined in 3D along the  $yOz$  plane. Therefore, by appropriately combining the two-colors, one can engineer arrays or chains of trapping sites in the vicinity of a nanofiber. The individual sites are arranged in two lines on both sides of the fiber.

**Collisional blockade** – Either zero or one atom can be loaded in each trapping site due to the effect of collisional blockade which does not allow two atoms to be loaded in microscopic traps like ours. This is because of the combined effect of light-assisted collisions of the MOT beams during the loading process of the dipole trap and the small trap volume, of subwavelength dimensions. The collision mechanisms, in the context of cold and ultracold atoms, are reviewed in [Weiner99] and how they impact loading of dipole traps and in particular microscopic traps can be found in [Kuppens00, Schlosser02]. This sets an upper limit to the filling factor  $f = 0.5$  in the nanofiber trap. The disorder resulting from finite filling factor will be analysed in chapter 3 in the context of our atomic Bragg mirror realization.

### 2.1.3 Light-shifts in a nanofiber trap

In subsection 2.1.1, we presented the general expression of the light shifts as a function of the specific atomic state and learnt about the different associated shifts- scalar, vector and tensor. These are true for any dipole trap including our nanofiber trap.

The experimental demonstration of nanofiber-trapped atoms [Vetsch10] in the group of Arno Rauschenbeutel in 2010, exhibited these aforementioned light shifts leading to several decoherence mechanisms in the trap. Using the trap parameters of [Vetsch10] i.e.  $\lambda_{red} = 1064$  nm,  $P_{red} = 2 \times 2.2$  mW and  $\lambda_{blue} = 780$  nm,  $P_{blue} = 25$  mW, the nanofiber trapping potential has been simulated in [Lacrout12, Ding12] and it shows the existence of these light shifts.

The scalar shift being independent of  $F$  (and  $m_F$ ) causes an equal shift of the ground state manifolds ( $6S_{1/2}$ ,  $F = 3$  and  $F = 4$ ) to the lowest order. At the next order (including hfs splitting in the perturbation) there will be a dependency of scalar polarizability on  $F$  which will lead to hyperfine decoherences. Coming to fine-structure levels  $|n J\rangle$ , the ground state ( $6S_{1/2}$ ) and the excited state ( $6P_{3/2}$ ) are shifted unequally leading to a differential scalar shift. For the parameters of [Vetsch10], the plot of the potential in [Lacrout12] shows that the ground state is trapped, with trap depth of a fraction of mK, whereas the excited states are not trapped at all except along the fiber axis  $z$ . For an atom excited, from a trapped ground state, to such untrapped levels will experience dipole-force fluctuations leading to heating in the trap.

The vector shift is proportional to the ellipticity of electric field which arises naturally for a nanofiber-guided mode (see section in chap 1). The longitudinal field component is cancelled out for the counter-propagating red-detuned beams making the polarization linear at the trap positions. However, since there is a single blue-detuned beam in the configuration of [Vetsch10], the ellipticity of the field mode has led to inhomogeneous broadening of the Zeeman sublevels. Due to spatially dependent vector shifts, these different sublevels trapped at different potentials will lead to phase decoherence. Even if the atoms are cooled to their motional ground state, the

spin-wave coherence time can be estimated in [Lacroute12] to be of the order of few  $\mu\text{s}$  for parameters of [Vetsch10].

The tensor shift vanishes for the ground state ( $J = 1/2, 6S_{1/2}$ ) of cesium. However, there is a non-zero tensor shift for the excited state ( $J = 3/2, 6_{3/2}$ ) of the  $D_2$  line.

### 2.1.4 Cancelling these shifts

We just learnt about the light-shifts that are detrimental to experiments in quantum-state engineering and manipulation of atomic states for implementation of quantum memory protocols. Hence, a state-insensitive, compensated trap was proposed by the group of Jeff Kimble [Lacroute12, Ding12] in 2012 to remove or alleviate some of these light-shifts. It was soon implemented experimentally by them [Goban12]. The implementation of our nanofiber trap is based on this proposal. Both the differential scalar shift and the vector shift are almost cancelled. The only remaining shift and broadening is due the tensor shift of the excited state.

As we saw in subsection 2.1.1, the ac Stark shifts for a two-level atom is equal and opposite for the ground and excited states. However, in a real alkali atom, the ground and excited states are coupled to several higher lying states. Considering the full Stark shift Hamiltonian in Eq.(2.1.3) (i.e. including counter-rotating terms and couplings to other levels), it maybe possible to find solutions where the ground and excited states have equal shifts with same sign, thanks to the multi-level structure. These situations arise when the atom is driven at particular wavelengths called “magic wavelengths”. This corresponds to having same scalar polarizabilities for ground and excited states i.e.,  $\alpha_{|g\rangle}^{(0)} = \alpha_{|e\rangle}^{(0)}$ . This will allow us to resonantly drive the optical transition.

For cesium  $D_2$  line, magic wavelengths [Le Kien13] are:  $\lambda_{red} = 935.2 \text{ nm}$  and  $\lambda_{blue} = 686.3 \text{ nm}$ .

The vector shift can be cancelled by using pairs of counterpropagating linearly polarized electric field. This can be achieved in our case for both red-detuned and blue-detuned beams by using pairs of counter-propagating beams. This is because the longitudinal field components cancel out for counter-propagating beams, so that there is linear polarization at position of atoms in the trapping sites. The vector shift vanishes for  $\pi$  (linearly) polarized light. This exactly happens for the red-detuned lattice, the frequency of forward propagating beam being same as that of backward propagating beam leading to zero vector shift. In case of blue-detuned beams, if the frequencies of forward and backward propagating beams are made equal, it would result in two superimposed lattices with different periods  $2\pi/\beta_{red}, 2\pi/\beta_{blue}$ . This is avoided, if we use a small offset  $\Delta_{blue}$  between the forward and backward frequencies such that the interference between the counter-propagating beams can be averaged over times much smaller than the motional or internal dynamics of a trapped atom i.e.  $\Delta_{blue} \gg (\omega_{trap}, \delta_{hfs})$ . where  $\omega_{trap}$  and  $\delta_{hfs}$  are trap angular frequency and ground state hyperfine splitting.

With  $\omega_{blue}^{(fwd, bwd)} = \omega_a + (\delta \pm \Delta_{blue})$  where  $\omega_a$  is the atomic transition frequency, the vector shift is cancelled for the blue-detuned light to the first order in  $1/\delta$ , as

$$H_1^{blue} \propto \frac{\Delta_{blue}}{\delta^2} \frac{F_y}{F}$$

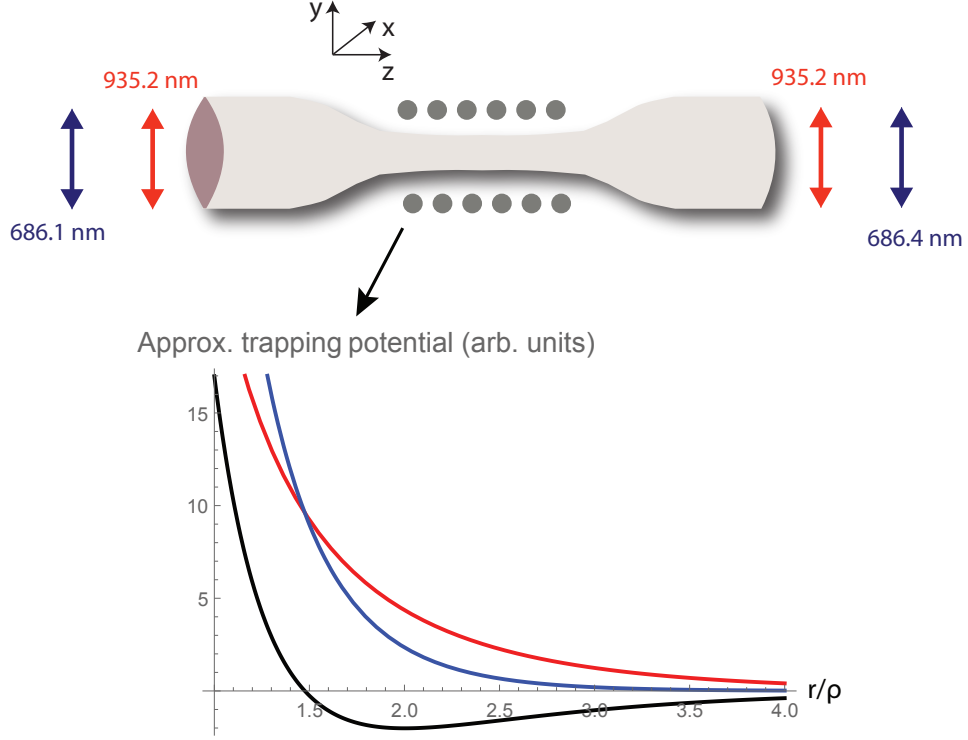


Figure 2.2 – State-insensitive dipole trap scheme. The magic wavelengths used are:  $\lambda_{red} = 935.2$  nm,  $\lambda_{blue1} = 686.1$  nm and  $\lambda_{blue2} = 686.4$  nm. This configuration cancels the differential scalar shift. Using both pairs of counter-propagating beams, the polarization of all dipole beams are linear at the nanofiber waist. This cancels the vector shift. As a result, atomic internal states are unaffected by the trap. The approximate potential experienced by the atoms are shown in the plot below. The intensities of red-detuned (red), blue-detuned (blue) beams as well as their negative sum (black) with their relative powers adjusted, are plotted as a function of distance from the center of nanofiber ( $\rho = 200$ ) nm. The potential minimum is approximately 200 nm from the fiber surface.

In our case,  $\lambda_{blue} = 686$  nm which gives the detuning from resonance  $\delta = 85$  THz. We know  $\delta_{hfs} = 9.2$  GHz and  $\omega_{trap}$  is on the order of hundred kHz. Therefore, we choose  $\Delta_{blue}$  to be  $\sim 100$  GHz. The typical values used in the experiment:  $\lambda_{blue1} = 686.1$  nm and  $\lambda_{blue2} = 686.4$  nm implying  $\Delta_{blue} = 191$  GHz. Thus, the vector shift is cancelled upto  $\Delta_{blue}/\delta = 2.2 \times 10^{-3}$  in the trap.

Figure 2.2 summarizes the state-insensitive, compensated nanofiber trap. The atoms are trapped in the lattice sites which are separated by a distance  $\lambda_{red}/2$ . The differential scalar shift is cancelled by using magic wavelengths for Cs. The vector shift is cancelled by using pairs of counter-propagating linearly polarized dipole beams. Only remaining shift is tensor shift for the excited state. This trap was demonstrated for

the first time in [Goban12] with each red-detuned beam power of 0.4 mW and each blue-detuned power of 5 mW. In their case, the nanofiber was 430 nm in diameter and the potential depth was estimated to be -0.27 mK at  $r_{min} = 215$  nm from the fiber surface. The radial, axial and azimuthal trap frequencies were estimated to be 199 kHz, 273 kHz, 35 kHz. We have similar characteristic trap parameters relative to them since we use the same scheme with close similarity in nanofiber diameter, power of dipole beams etc.

## 2.2 Experimental implementation

We have presented the theoretical framework and underlying concepts that are at the heart of a nanofiber-mediated dipole trap. We now go into its experimental realization. The experimental setup can be broadly classified into three parts: the vacuum system, the optical system for manipulation of cold atoms, and the optical system for dipole trapping. This section will be organized as follows. We will first describe the preparation of cold atoms (MOT) and subsequent interfacing of atomic cloud with the guided-light of a nanofiber. Then, we will discuss how to prepare our system by magnetic field cancellation for the interfaced atoms and alignment of polarization in the nanofiber. An overview of our laser systems and optical components will be presented thereafter. Finally, we detail the loading and implementation of the dipole trap, with its characterization.

**Controlling the experiment** – All the ingredients and different aspects of the experiment need to be precisely controlled and synchronized. In addition, we must be able to dynamically change parameters during an experimental run and be able to acquire data. All this is done in an efficient manner, thanks to field-programmable gate array FPGA (Digilent Nexys 3). The language used for programming is Python. There are two FPGAs in our experiment. The first one synchronizes the timing events and provides digital outputs (TTL signal) for turning on/off laser beams, magnetic field gradients or to trigger acquisition in various devices. The time resolution of our FPGA is 10 ns which is sufficient for our purposes now. The second FPGA is used for time-stamp acquisition from the single-photon counting modules (SPCM-AQR-14-FC). The synchronizer FPGA triggers a time window for digital acquisition of analog signals coming from single-photon counting modules. Before acquisition, the narrow pulses (width  $\sim 10$  ns) from our counters are shaped to a longer time interval so that all the pulses are recorded digitally. If the analog voltage is below a threshold value, 0 photon is registered but if the voltage is above the threshold, 1 photon is registered. The acquisition, done by this second FPGA, is retrieved and analyzed by a computer. Thus, combining these two FPGAs we can efficiently control the experiment and dynamically change pulse timings, frequencies of laser beams and many other parameters.

### 2.2.1 MOT and nanofiber

We have a typical vacuum system meant for cold atom experiments. We can reach ultra-high vacuum (UHV) regime of pressure less than  $10^{-8}$  mbar. In our case, the vacuum system needs to be ‘breakable’ for introducing nanofibers into the chamber.

The setting up of vacuum systems, the protocol of transfer of a nanofiber into the chamber and subsequent interfacing of cold atoms with the nanofiber-guided light including the first experiment of demonstrating an EIT-based memory, in this interface have been described in Baptiste Gouraud’s PhD thesis [Gouraud16]. We will give a summary here.

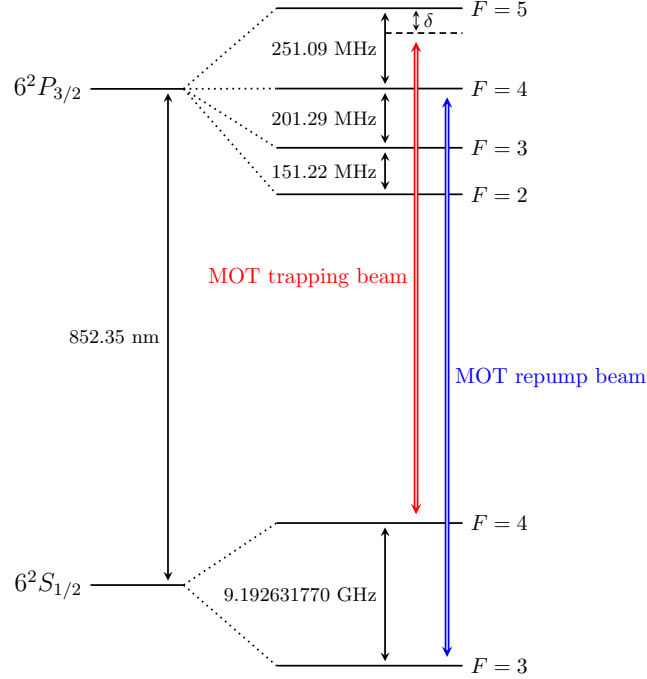


Figure 2.3 – The D<sub>2</sub> line of cesium atom showing transitions used for the MOT. The trapping/cooling beams are red-detuned by  $\delta = 10$  MHz relative to  $\{6S_{1/2}, F = 4\} \rightarrow \{6P_{3/2}, F' = 5\}$  transition. The repump beams are on  $\{6P_{3/2}, F = 3\} \rightarrow \{6P_{3/2}, F' = 4\}$  transition.  $6S_{1/2}$ ,  $F = 3$  and  $F = 4$  are the two hyperfine ground states,  $6P_{3/2}$  is the excited state with a spontaneous emission decay rate in free space  $\Gamma_0/2\pi=5.23$  MHz.

The first thing is to produce a cloud of cesium atoms at the center of the vacuum chamber by means of a conventional magneto-optical trap (MOT). There are 3 trapping beams (2 of them are mixed with the repump beams), all of which are collimated through the chamber and retro-reflected on the mirrors at the other side of the chamber. Figure 2.3 shows spectroscopic structure of the cesium D<sub>2</sub> line. The trapping or cooling beams are 10 MHz red-detuned from the cyclic  $\{6S_{1/2}, F = 4\} \rightarrow \{6P_{3/2}, F' = 5\}$  transition. Before the collimator, the power in each trapping beam is  $\sim 35$  mW. Atoms lost to  $F = 3$  ground state are rapidly pumped back to  $F = 4$  state by the repump beams, which is on  $\{6P_{3/2}, F = 3\} \rightarrow \{6P_{3/2}, F' = 4\}$  transition. The power, before the collimator, in each repump beam is  $\sim 5$  mW. After collimation, both trapping and repump beams are 1 inch in diameter.

The magnetic field is produced by a pair of coils in “anti-Helmholtz” configuration. The coils are rectangular in shape to produce a cigar-shaped, elongated atomic cloud parallel to the fiber to ensure an optimal overlap with the nanofiber. Typically, the

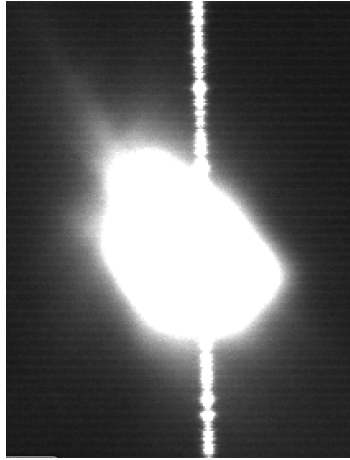


Figure 2.4 – Atomic cloud overlapped with the nanofiber in ultra-high vacuum.

length of our cloud is  $\sim 3$  mm, which is smaller than the nanofiber waist of  $\sim 1$  cm.

Once the nanofiber is inserted in the vacuum chamber, and ultrahigh vacuum established, we overlap the MOT and nanofiber. In our case, the nanofiber is fixed onto a vacuum fiber holder, so the atoms are to be slightly moved. This is done by tweaking the collimators that misaligns the MOT beams and in turn displacing the atoms. The real-time images of the 3 cameras help us to visualize the overlap. While this is being done, the absorption of a resonant probe through the nanofiber is monitored with a sensitive photodiode (Pacific Silicon Sensor AD-500-9-TO52; sensitivity  $\sim 0.36$  V/nW). The goal is to get as much absorption (or optical depth<sup>2</sup> OD) as possible with the alignment of MOT beams, though there is an upper limit to OD with cold atoms moving around in the vicinity of a nanofiber. With an optimal overlap of MOT and nanofiber, we get an OD of few units (OD  $\sim 3$  for  $\{6S_{1/2}, F = 4\} \rightarrow \{6P_{3/2}, F' = 4\}$  transition).

### 2.2.2 Polarization alignment of the nanofiber-guided light

Once we are able to interface the atoms via the evanescent field of a nanofiber, it is essential to know and precisely control the polarization of the guided light. The method of aligning polarization in the nanofiber is demonstrated in [Vetsch12, Goban12] and illustrated in Figure 2.5. Close to the nanofiber, a polarizer is set on  $xz$  plane with its axis along the  $x$  direction. A camera is placed on the other side of the polarizer to collect the light Rayleigh scattered by the imperfections and impurities on the nanofiber. The scatterers, being dipole emitters, will preserve the polarization and no light will be scattered along the direction that the dipole oscillates i.e., in our setup, the camera on  $y$ -axis will not detect any light for dipole oscillation along  $y$ -axis but will detect maximum light intensity for dipole oscillation along  $x$ -axis. For a guided mode quasi-linearly polarized along  $y$  or  $x$  the longitudinal component along  $z$  is filtered by the polarizer. Therefore, the collected light in the camera will be maximal (minimal)

<sup>2</sup>OD is defined as  $-\ln\left(\frac{I}{I_0}\right)$  where  $I/I_0$  is the ratio of measured power with atoms and without atoms on the photodiode.

for  $\phi = \pi/2$  ( $\phi = 0$ ) i.e., for guided light quasi-linearly polarized along  $x$ -axis ( $y$ -axis). Few hundred micro-watts of light sent through the nanofiber is enough to obtain a significant signal in the camera. The polarization in the nanofiber is aligned by

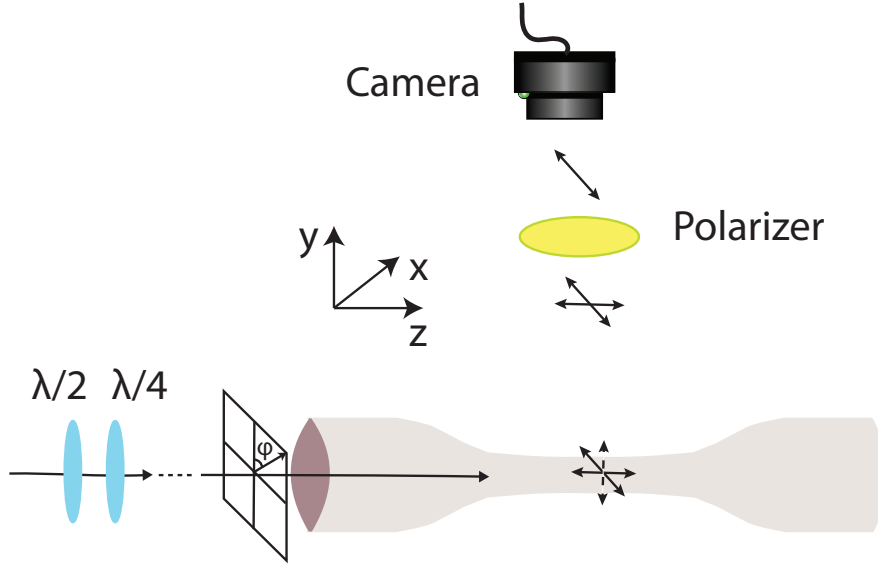


Figure 2.5 – Alignment of the guided mode polarization. The light in the guided mode is scattered by the dipole emitters on the nanofiber surface and is collected by a camera on  $y$ -axis. The polarizer filters the longitudinal component along the fiber axis  $z$ . The collected light intensity is maximum (minimum) for orientation of the electric field along  $\phi = \pi/2$  ( $\phi = 0$ ) i.e. for quasi-polarized light along  $x$ -axis ( $y$ -axis).

adjusting the quarter- and half-wave plates on the free-space beam before it is coupled into the fiber connecting the nanofiber. In our case, measuring the minimum light intensity in the camera will align the light vertically (along  $y$ -axis) in the nanofiber. Once aligned, we must avoid touching the ends of nanofiber or fibers connected to the nanofiber. This is because we are dealing with all non-polarization maintaining fibers and any bending or temperature change in the fiber will disturb the polarization state in the fiber due to the birefringence of the system.

### 2.2.3 Cancelling the residual magnetic field: Zeeman sublevel microwave spectroscopy

It is necessary to cancel the magnetic field because it is a major source of decoherence in quantum-memory like experiments. If the Zeeman sublevels are split due to spurious magnetic fields, field gradients or fluctuations (see Figure 2.6), it will result in inhomogeneous broadening and fast dephasing of the collective excitation or spin-wave. The cancellation is accomplished by adjusting the current of the three pairs of compensation coils (i.e., adding a B field offset and gradient) placed around the vacuum chamber. The process is summarized below.

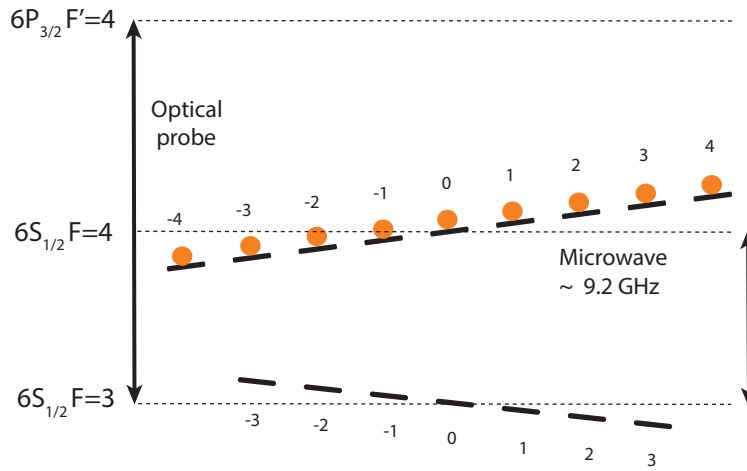


Figure 2.6 – Principle of Zeeman sublevel microwave spectroscopy. In the presence of magnetic field, the Zeeman sublevels of the two ground states are split in opposite direction. The atoms initially on  $\{6S_{1/2}, F = 4\}$  are transferred to  $\{6S_{1/2}, F = 3\}$  by microwave pulse. The absorption of a probe  $\{6S_{1/2}, F = 3\} \rightarrow \{6P_{3/2}, F' = 4\}$  is then recorded while the microwave frequency is scanned about the hyperfine splitting  $\omega_{hfs} = 9.2$  GHz.

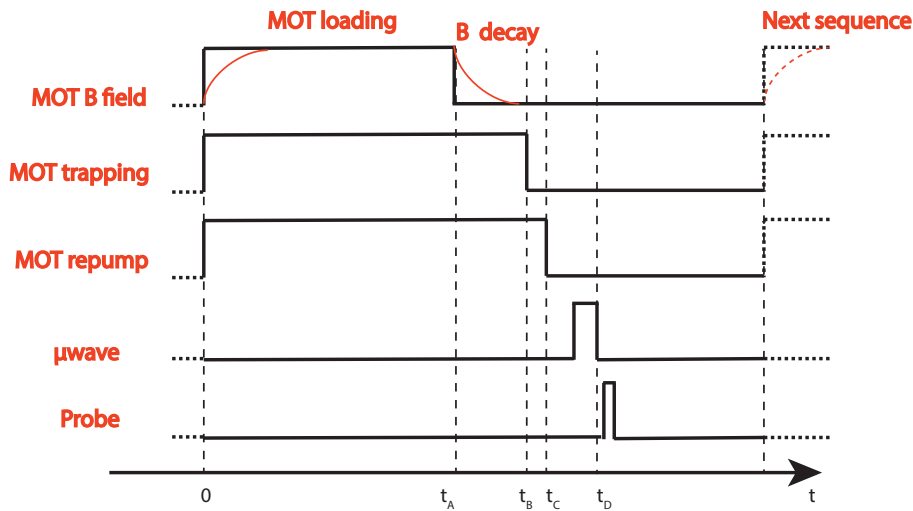


Figure 2.7 – Timing sequence for microwave spectroscopy. Typical numbers for B field cancellation at 4.5 ms after the MOT B field is shut-off: MOT loading time  $t_A = 120$  ms, MOT trapping beams off after  $t_B - t_A = 4.2$  ms, MOT repump beams off after  $t_C - t_B = 90 \mu\text{s}$ , microwave  $\pi$ -pulse of duration  $\sim 90 \mu\text{s}$  for optimal transfer to  $F = 3$  ground state. This is followed by the probe pulse at  $t_D - t_A = 4.5$  ms. The pulse delays can be modified for cancellation at other times.

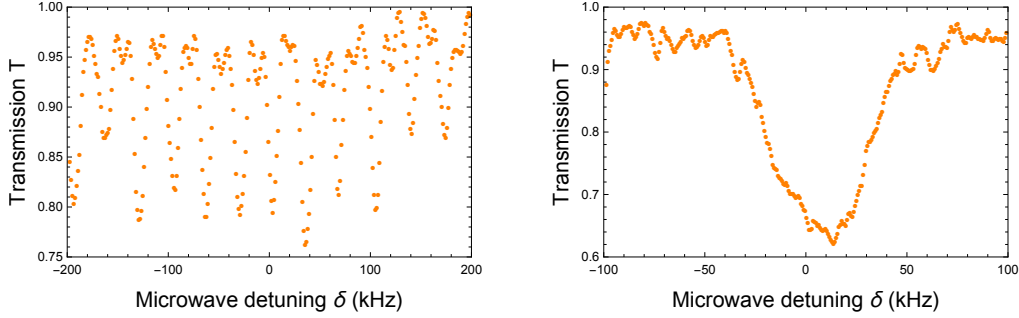


Figure 2.8 – Measurement for microwave spectroscopy. The transmission of the optical probe  $\{6S_{1/2}, F = 3\} \rightarrow \{6P_{3/2}, F' = 4\}$  as a function of microwave detuning from the ground state hyperfine splitting. When the B field is not cancelled (left), several peaks are visible, each of them corresponding to a  $\pi$  or a  $\sigma$  transition from  $F = 4 \rightarrow F = 3$ . When the B field is cancelled (right) only one central peak is visible, whose width here is 50 kHz implying the B field has been compensated down to 10 mG level.

Our B field cancellation is mainly limited by the decay of eddy currents in the metallic chamber. Figure 2.7 shows the timing sequence of our experiment. After the current in MOT coils is shut off, the eddy currents are left to decay for few milliseconds (waiting time: 4 ms found experimentally). Then the MOT trapping beams, followed by the repump beams, are turned off. The additional repump beam ( $\sim 90\mu\text{s}$ ) at the end pumps the atom to  $\{6S_{1/2}, F = 4\}$  state. Soon, a microwave  $\pi$  pulse (typically  $\sim 90\mu\text{s}$  pulse width in our case) with frequency  $\omega$  close to the hyperfine splitting  $\omega_{hfs} = 9.2$  GHz, is applied, via a basic antenna, from a microwave source (synthesizer level set at maximum 30 dBm). This pulse transfers atoms prepared in  $\{6S_{1/2}, F = 4\}$  to  $\{6S_{1/2}, F = 3\}$  level via a magnetic dipole transition. A probe pulse in free space resonant with  $\{6S_{1/2}, F = 3\} \rightarrow \{6P_{3/2}, F' = 4\}$  or  $\{6S_{1/2}, F = 3\} \rightarrow \{6P_{3/2}, F' = 2\}$  transition is then sent into the cloud to probe the presence of atoms in  $\{6S_{1/2}, F = 3\}$  while the detuning  $\delta = \omega - \omega_{hfs}$  of the microwave pulse is varied. Now, if the transmission of the probe is plotted as a function of the microwave frequency detuning  $\delta$ , absorption peaks can be observed, see Figure 2.8.

If there is a non-zero magnetic field, the Zeeman sublevels are non degenerate leading to the splitting of absorption peaks, each peak corresponding to a  $\sigma$  or a  $\pi$  transition. Infact, there are 15 absorption peaks in total: 7 are  $\pi$  transitions (with relatively more absorption) and the remaining 8 are  $\sigma$  transitions. Once, the magnetic field is cancelled (close to zero) there is only a central peak, whose width gives the precision up to which the B field is cancelled. The achievable minimal width of this peak is limited by the eddy currents in our metallic chamber. In our case, the width of central peak after cancellation is less than 100 kHz i.e. the fields are compensated down to 20 mG level. In best cases, we have been able to cancel the field upto 10 mG, corresponding to central peak-width of 50 kHz in Zeeman sub-level spectroscopy.

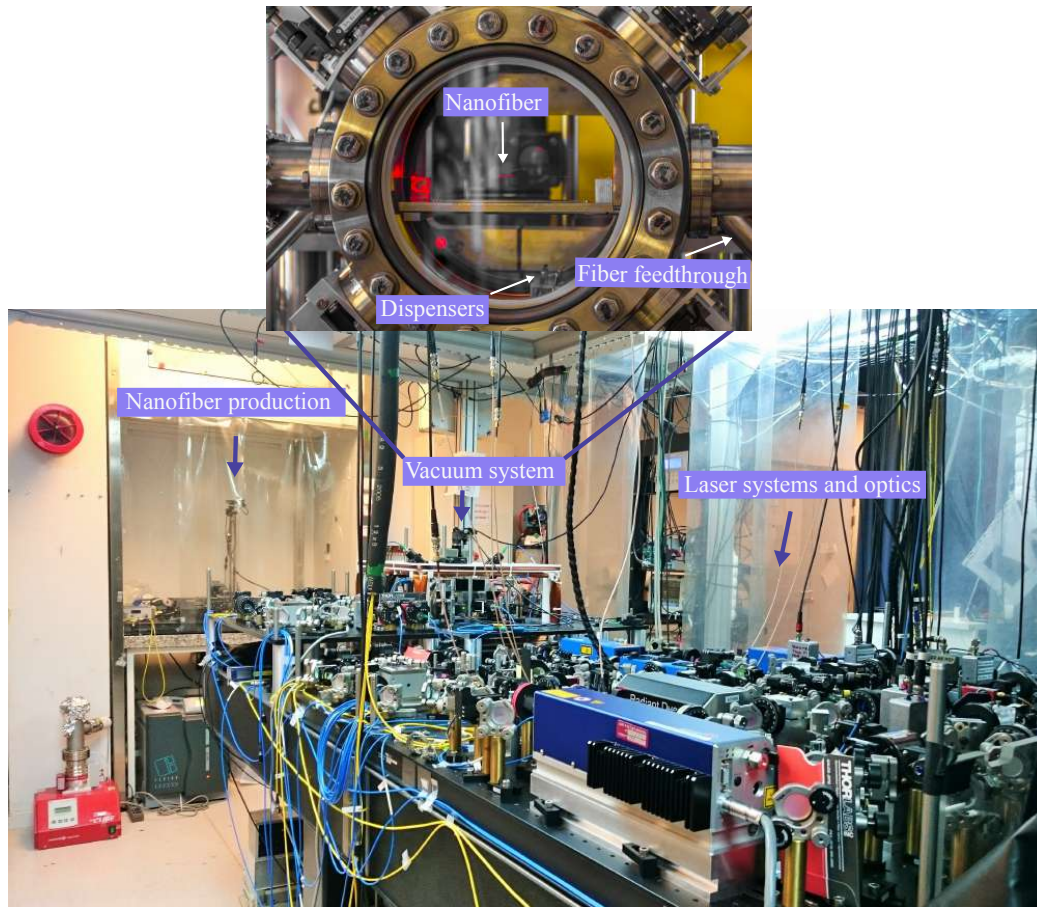


Figure 2.9 – Overview of the setup showing the nanofiber production bench, the vacuum system and the laser systems and optics. The last can be classified into two parts - laser systems for cold atoms manipulation and laser system for trapping atoms close to the nanofiber. The vacuum system is zoomed in showing the nanofiber (seen as red line because of 686 nm coupled into it) inside the vacuum chamber.

#### 2.2.4 Laser systems and optical components: an overview

In this section, we present an overview of the different laser systems, locking systems, various optical components and filtering elements used in our experiment. Figure 2.9 is a general lab view showing most of the elements. Figure 2.10 is a view of another optical table with the Ti:Sapphire laser and optics. We have tried to be compact in our design so that we can fit as much as possible in the limited space while keeping room and flexibility for future. We will explain our laser systems and different optical components used in our setup. The challenge here is to make all the required beams available with sufficient power and frequency tunability as well as ensuring long-term stability and flexibility. A lot of the optical components are quite sensitive to alignment, focusing and polarization and one has to re-align and re-adjust parts of the setup as and when required.

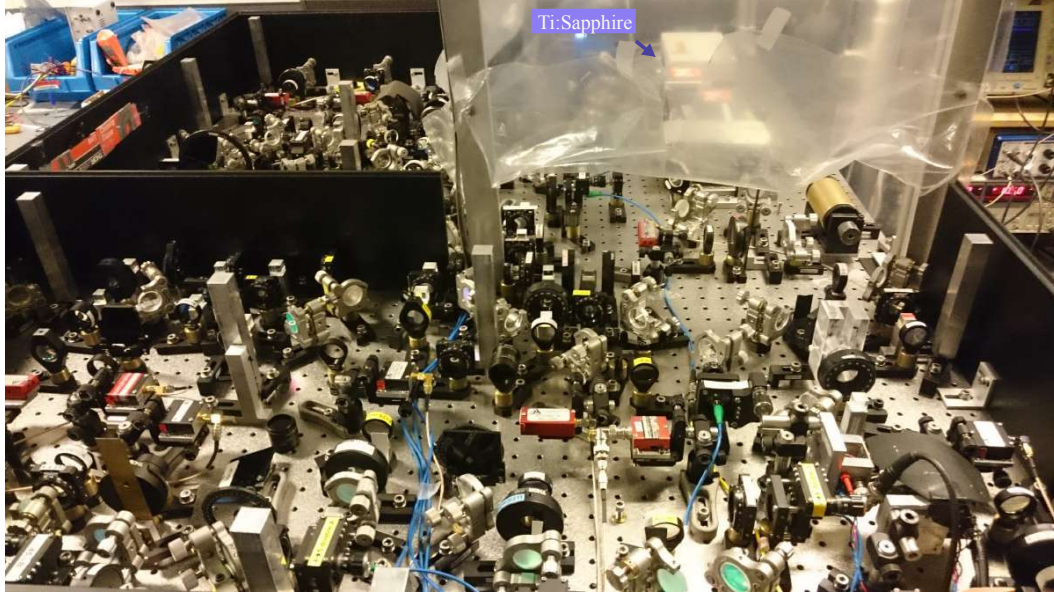


Figure 2.10 – Optical table containing Ti:Sapphire laser. This ultra-stable, low-linewidth laser is locked to an absorption peak in absorption profile of saturated absorption spectroscopy. It is then a reference and a source for various probe beams addressing  $\{6S_{1/2}, F = 4\} \rightarrow \{6P_{3/2}, F'\}$  transitions where  $F'$  can be any of the hyperfine levels in the excited state. Different paths, derived from Ti:Sapph, use acousto-optic modulators (AOMs) and other optics for preparing beams corresponding to particular transitions as required in the experiment.

The trapping beams and repump beams are coming from commercial external cavity diode lasers (Laser Labs), each with around 40-50 mW of power. The laser output is followed by anamorphic prism pairs for mode cleaning, optical isolators to prevent back-reflection into laser cavity and quarter- and half-wave plates for polarization control. The beams are divided into multiple paths for various purposes. Typically, for locking lasers we use **saturated absorption spectroscopy**, a setup that allows precise determination of atomic transition frequency. In this method, a probe and a relatively stronger pump (to saturate the transition) are made to counter-propagate in a vapor cell. When the laser is scanned around resonance, the absorption spectrum of the probe is composed of small absorption dips in a Doppler-broadened feature. The dips correspond, either to hyperfine resonances, which are transitions from the ground state  $6S_{1/2}$  to the excited state in the hyperfine manifold of  $6P_{3/2}$ , or to crossover lines in which the pump and the probe address different transitions as a result of thermal motion of the atoms. The absorption signal is recorded in the photodiode. The laser can be locked to one of these absorption lines. The locking is performed by modulating the laser current of the diode lasers. The absorption signal from photodiode is then demodulated by a built-in lock in amplifier to obtain the error signal, which is fed back on to the laser for a stable lock.

**Acousto-optic modulators (AOMs)** are commonly used tools in atomic physics

experiments. It uses acousto-optic effect to induce frequency shifts on the laser beam at multiples of the acoustic wave frequency. We typically use AOMs (AA Opto-Electronic) centered on 100 MHz and 200 MHz. Typically, 75-80 % of input light can be obtained at these frequencies in the first order diffraction and this is what we use in two configurations: single-pass and double-pass, where the first order beam is retro-reflected back and made to diffract a second time such that the total frequency shift is doubled compared to the first order. In our setup AOM is used for two purposes: fast turning on/off the beams at timescales of tens of nanoseconds and shifting the frequency of the beams from some reference spectroscopic line using a single/double pass. The RF frequencies generated from voltage controlled oscillator (VCO) drive the AOMs. A Mini-Circuit switch, added to the VCO, can turn on/off the RF signal and hence the VCO output based on a input TTL signal enabling us to generate light pulses in our experiment. The TTL signal comes from one of the digital outputs of FPGA.

**Tapered amplifier** (Toptica's BoosTA) is used for obtaining the desired high power needed for trapping beams. With around 16 mW input from one of the diode lasers, it amplifies the power to 400 mW. The beam is then passed through a double-pass AOM before being distributed through optical fibers as MOT trapping beams for the three directions.

For most of our experiments (Raman transitions or EIT experiments) we are addressing a three-level atomic transition. There is signal or probe field addressing the ground and excited states as well as there is an additional control field coupling the other hyperfine ground state to the excited state. It is important for both signal and control fields to have a narrow frequency linewidth and be phase-stable. This is achieved in our setup in the following way.

The signal (or probe) in our experiment, for transitions corresponding to  $\{6S_{1/2}, F = 4\} \rightarrow \{6P_{3/2}, F'\}$  ( $F'$  can be any of the hyperfine levels in excited state) in  $D_2$  line are generated from from Ti:Sapphire (Msquared), which is a frequency stable, low amplitude noise ( $\lesssim 0.05\%$ ) and low linewidth ( $\lesssim 50$  kHz) laser source. The power delivered by Ti:Sapph is close to 2 W. A very small fraction of Ti:Sapph is used for locking by means of saturated absorption spectroscopy. Here, we lock the laser by modulating the double-pass AOM before the saturated absorption setup. Therefore, all the beams derived from Ti:Sapph are free of modulation and has the same linewidth as that of the laser.

The control field's frequency needs to be maintained below the signal frequency at  $\omega_{hfs} = 9.2$  GHz or around in case the two-photon detuning has to be scanned. This is done by **phase-locking** a diode laser with the Ti:Sapph. In this technique, both lasers are mixed on a beam splitter and the output beam is detected with a high-speed photodiode. The beat-note frequency (after a division of the original beat frequency) is compared with a standard reference frequency of an electronic oscillator. The error signal generated is fed back to the diode laser. We use a commercial phase-locking system (Vescent photonics D2-135). The diode laser phase-locked with Ti:Sapph has now a narrow linewidth and its frequency can be easily tuned by changing the frequency of the reference oscillator.

The **red-detuned (935 nm)** and the **blue-detuned (686 nm)** dipole trapping beams are generated from three commercial diode lasers (Toptica DL Pro) - the two blue-detuned beams are derived from two different lasers whereas two red-detuned



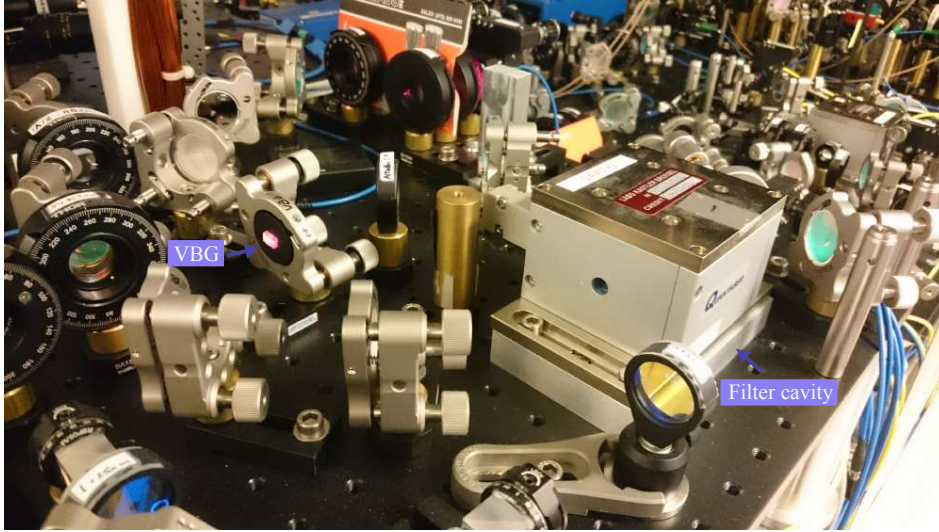


Figure 2.12 – Part of the breadboard where mixing and filtering of the dipole beams and the signal at 852 nm take place. The spectral filtering systems - Filter cavity and Volume Bragg grating (VBG) are shown.

and after mixing they will be coupled into non-polarization maintaining single-mode fiber, identical to the fiber used for nanofiber-fabrication. Our experiment requires that each dipole beam has an independent control of polarization. This is done by putting quarter- and half-wave plates on the path of each dipole beam before they are mixed on a dichroic mirror placed on each side of the nanofiber (see Figure 2.11). Following the dichroic mirror, the dipole beams are combined with the signal at 852 nm on a **Volume Bragg gratings** (VBG). In fact, there two VBGs used for spectral filtering at the fiber input. If we look closely at the system there are three beams coming out of nanofiber on either side. The blue-detuned and the red-detuned beams, combining several milliwatts of power, and the 852 nm signal nm usually at the single-photon level. VBGs help to separate out the weak signal from the strong dipole beams. It reflects the signal at 852 nm while being transparent to both the dipole beams. The signal after bouncing off two VBGs is usually connected to the input path on one side and to the detection system on the other side. Losses on 852 nm path are minimized as much as possible. Before the detection system, the signal is made to pass through a lens-based **filter cavity** to prevent contamination from control field ( $\omega_{hfs} = 9.2$  GHz away from the signal). In addition to this spectral filtering, polarization filtering, comprising of quarter-, half-wave plate and polarizing beam splitter (PBS), is also employed to filter the control field, which has orthogonal polarization to that of the signal in the context of EIT-type experiments. Both spectral filtering systems, namely - VBG and the filter cavity will be more specifically described in the next section.

### 2.2.5 Spectral filtering systems

**Volume Bragg grating (VBG)** – It is produced by modulation of refractive index in the volume of a photosensitive material (designed by Optigrate). It has around 95 % reflectivity at 852 nm with a bandwidth  $\sim 1$  nm. The transmissivity of blue-detuned and red-detuned wavelengths is  $> 85-90$  %. The suppression of the undesired wavelengths is on the order of 70 to 90 dB. Combining the two VBGs, we get a total rejection of  $> 120$  dB measured experimentally. This is enough for us to prevent any contamination of dipole beams when detecting single-photon signal pulses by avalanche photodiodes (APD). VBGs are a critical tool in our experiment for filtering out the strong dipole beams on the order of few milliwatts from the signal at the single-photon level.

**Filter cavity** – This is a commercially-available temperature-stabilized Fabry-Perot Etalon (FPE001B from Quantaser) meant for spectral filtering [Palittapongarnpim12] in experiments involving cesium. A plano-convex lens, with high reflectivity dielectric coating ( $R \sim 99\%$ ), is placed on the waist of a Gaussian beam wavefront. Depending on the thickness and refractive index of the lens, only a narrow band of wavelengths will be transmitted because of constructive interference of the light reflected multiple times between the cavity boundaries. All other wavelengths will be reflected because of destructive interference. To quote some cavity parameters: 75 % transmission on cavity resonance and an extinction of 38 dB can be obtained at 9.2 GHz (away from resonance). Cavity transmission bandwidth (FWHM) = 60 MHz, Free spectral range (FSR)=16 GHz.

A plano-convex lens ( $f=250$  mm) produces the required beam waist ( $\sim 57\mu\text{m}$ ) at the position of the etalon. The cavity transmission frequency can be tuned by adjusting the temperature by few mK, which changes the length of etalon. Figure 2.13 plots the cavity transmission of  $\text{TEM}_{00}$  mode over a FSR and the extinction is measured to be  $\sim 34$  dB over the background (marked with blue). This cavity has not only allowed us to filter out the control field from the signal but has enabled us to obtain a near-resonant trap to demonstrate - Bragg reflection from 1D chains (detailed in chapter 3), by filtering the red-detuned beams at  $\Delta\lambda = 0.1, 0.2$  nm away from the signal wavelength. VBGs have been ineffective since the red-detuned wavelengths are within its bandwidth ( $\sim 1$  nm).

With the knowledge of the dipole beams and filtering units, we will proceed now on to the actual trapping of atoms in the vicinity of a nanofiber - from loading the trap to obtaining high OD, in the next sections. We will also provide characterization of our trap.

### 2.2.6 Trap loading sequence

Loading far-off-resonance traps (FORTs), dipole traps created by focused Gaussian laser beams has been studied for instance in [Kuppens00]. A similar loading mechanism can be used in a microscopic, evanescent field trap like ours. In our case, the loading efficiency (or the filling factor) reaches a maximal value of  $1/2$  because of collisional blockade effect. For loading purposes, the temperature of the atomic cloud has to be lowered below the potential depth of the trap. This is done by cooling in short molasses

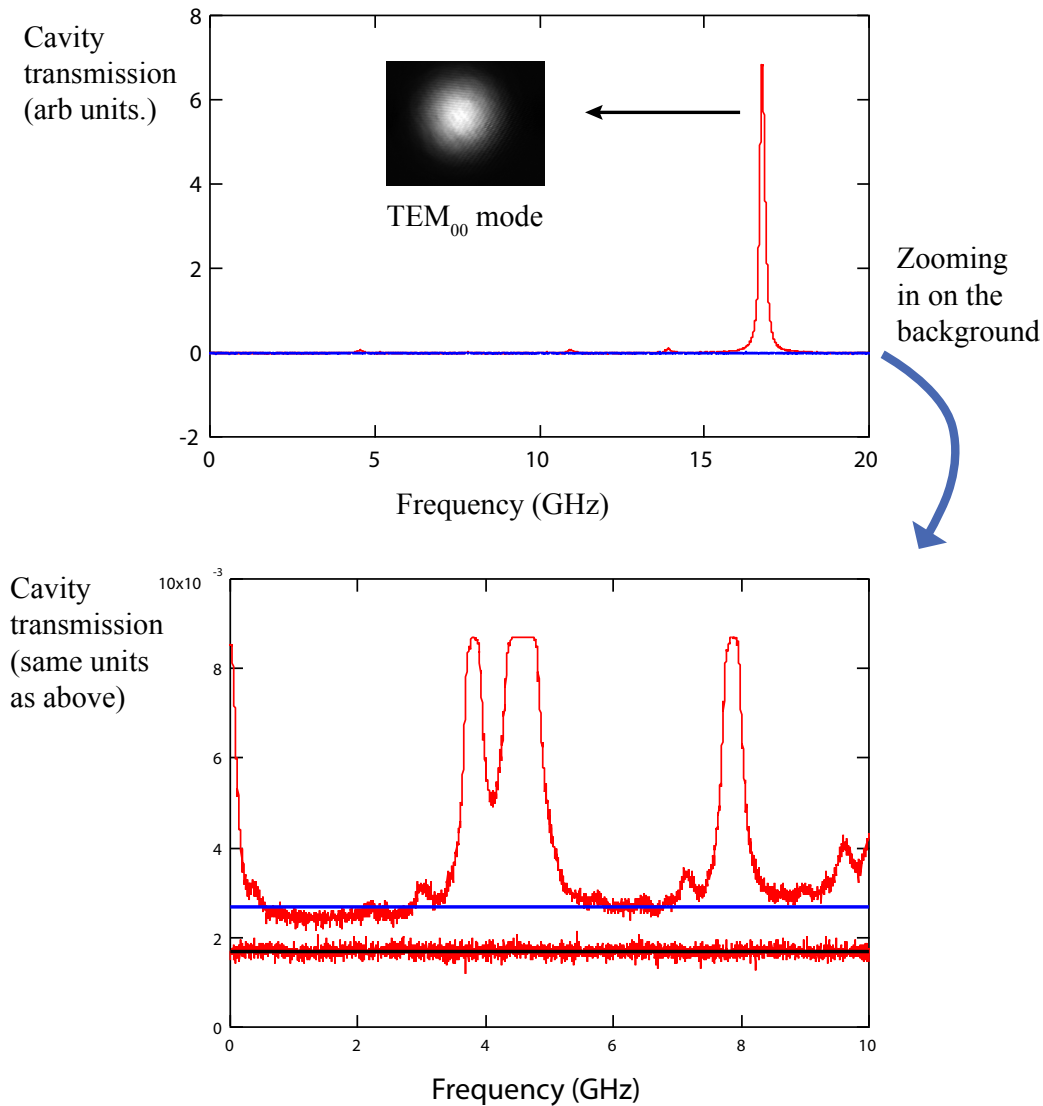


Figure 2.13 – Characterization of lens-based filter cavity. The frequency of the cavity is scanned over its free spectral range by tuning its temperature. A 75 % transmission (top) for TEM<sub>00</sub> (Gaussian) mode and a background suppression (below) of 34 dB are recorded.

phase before the atoms are loaded in the trapping sites. The cooling mechanism here is **polarization gradient (PG) cooling** (also called optical molasses) that can allow us to reach Sub-Doppler temperatures (on the order of  $\sim 10T_{rec}$  corresponding to few  $\mu K$  for cesium,  $T_{rec}$  being the recoil temperature). In this mechanism, the MOT B field is switched off (and the field decays) while the detuning of MOT trapping beams is increased from its initial value to tens of natural linewidth (of the spectral line) and its power is ramped down in time. The repump beam power has to ramped down as

well. The lower temperature of the cloud at the end of molasses phase can be checked by measuring the cloud temperature using time of flight measurements.

**Time of flight measurements** – If a resonant probe is sent into the released cloud and imaged by a standard CCD camera on the other side, one sees the cloud as a ‘ball-shaped’ dark entity on a lit background. Images are taken at regular time intervals for recording the fall and expansion of the cloud. From image analysis, one can find the expansion of cloud radius  $\sigma$  (given by Gaussian-fitted intensity profile) as a function of time  $t$  to deduce the temperature  $T$  of the cesium ( $M$  atomic mass) cloud from the relation:

$$\sigma^2(t) = \sigma^2(0) + \frac{k_B T}{M} t^2$$

Using this technique, we have measured cloud temperatures of 370  $\mu\text{K}$  and 15-20  $\mu\text{K}$  before and after the molasses phase.

The dipole trapping beams are left continuously on during the entire experiment, thanks to the efficient filtering systems. The trap loading sequence is illustrated in Figure 2.14. We have used two timings for molasses - the long 10 ms and the short 4 ms. The parameters for 4(10) ms are given here. First, the MOT is loaded with loading time typically  $> 60$  ms. At time  $t_A$  ms the MOT B field is shut-off. At the same time, the detuning of MOT trapping beams are increased from  $-2\Gamma$  to approximately  $-14\Gamma$  with a time constant 0.2 (2.2) ms. From  $t_A$  ms to  $t_B = t_A + 4(10)$  ms the MOT trapping and repumping beams are ramped down (following approximately exponential decay) in power with time constants 0.7 (2.2) ms. The decay time of repump is found insensitive in this loading scheme. At  $t_B$  ms, the MOT trapping beams are shut-off and the trap is considered to be loaded. An addition repump is added at  $t_B$  for  $t_C - t_B = 500 \mu\text{s}$  to have a clean system with all atoms populated in  $\{6S_{1/2}, F = 4\}$  state. The trap is ready to be probed at this stage.

There is ongoing work to optimize the decay constants, decay profiles of the trapping beams and repump beams as well as playing with other parameters in the loading process. The goal is to cool the atoms further down and improve the loading efficiency. There are other possibilities, in principle, to have high loading efficiencies by using a blue-detuned beam, with a small detuning chosen carefully [Lester15].

### 2.2.7 Procedure for obtaining the nanofiber trap

Along with the loading sequence mentioned in last section, we have to go through a series of steps to have a ready, functioning nanofiber trap. The steps are:

- On both sides of the nanofiber, fiber connectors are used to connect the nanofiber tails to regular single-mode fibers of same type. These connectors are opened on a regular basis to measure each of the dipole beam powers. The powers of the corresponding dipole beams are made equal on both sides of the nanofiber. If the filter cavities need to be aligned for the experiment, they should be done at this step.

Typical values for each beams: Red-detuned power - 500  $\mu\text{W}$ ; Blue-detuned power - 4 mW.

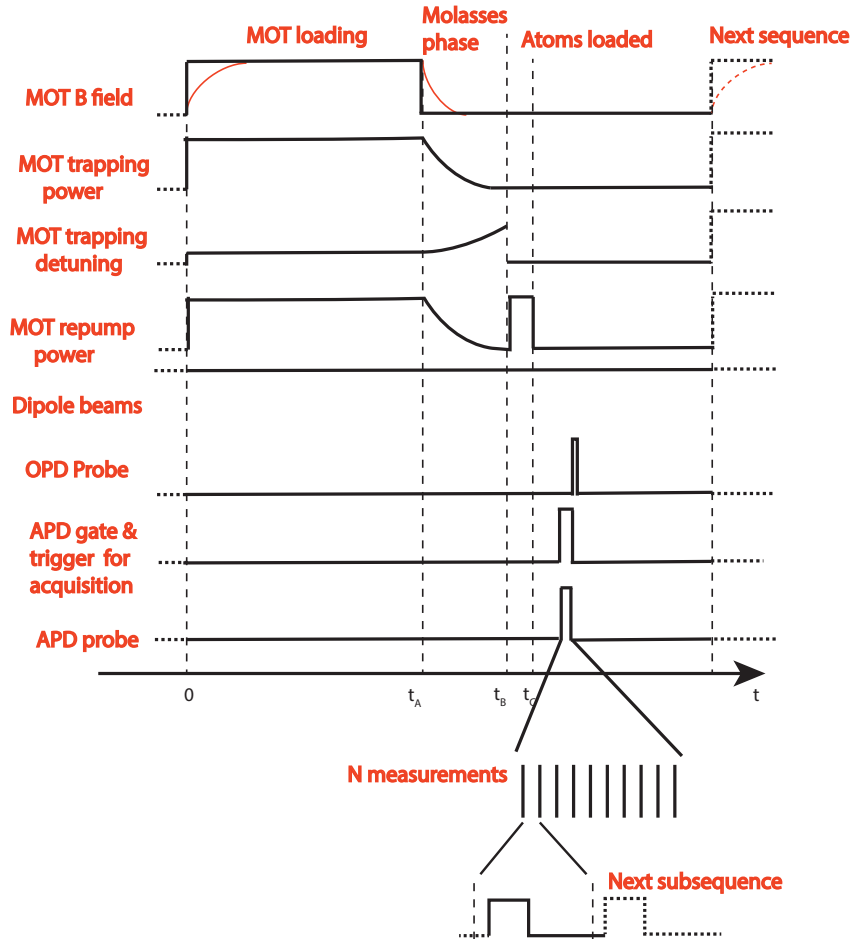


Figure 2.14 – Typical time sequence for experiments with trapped atoms. Once the MOT B field is turned off at  $t_A$ , the trap loading sequence or molasses phase starts. This involves ramping down the power of both the MOT trapping and repump beams. The detuning of the MOT beams is increased as well during this time. At time,  $t_B$  the dipole trap is loaded. An additional repump for  $t_C - t_B = 500 \mu\text{s}$  is added at  $t_B$  to have a clean system with all atoms populated in  $\{6S_{1/2}, F = 4\}$  state. The trap now could be probed either by a weak signal, typical duration of few tens of  $\mu\text{s}$ , to be detected by OPD (OPD probe) or by single-photon level pulses to be detected by APD (APD probe). The APD probe has a duration on the order of ms and it consists of  $N$  repeated measurements or subsequences, each subsequence comprises of a pulse (or pulses) with less than a photon per pulse. The length of each subsequence is chosen typically between  $1 \mu\text{s}$  and  $10 \mu\text{s}$  depending on the experiment. The APD gate trigger allows acquisition of data collected from  $N$  measurements over multiple MOT cycles to build statistics. OPD and APD stand for optical and avalanche photodiodes.

- Before putting back the fiber connectors, we have to carefully clean the fiber tips to ensure there is no transmission loss at the connectors. This is important to balance the power of dipole beams on both sides. The last two steps are crucial for obtaining state-insensitive, compensated trap and high optical depth (OD) in the trapped ensemble of atoms.
- Around 500-700  $\mu\text{W}$  (not more) of 852 nm probe ( $F = 4 \rightarrow F' = 5$ ) is sent into the nanofiber. The polarization of the probe is aligned vertically using the method outlined in subsection 2.2.2. Its polarization on the other side of nanofiber is also aligned by minimizing or maximizing the detected power. Therefore, the probe can now be sent into the nanofiber from either side with correct polarization. Following this, each of the dipole beams on either side are aligned vertically in the same way, remembering only one beam at a time has to be sent into the nanofiber.
- All the dipole beams and the probe, with their polarizations aligned, are now sent into the nanofiber with the probe being attenuated and pulsed. The dispensers are turned on. The MOT beams are locked to their respective transitions. The molasses sequence (involving ramping of the beams) is turned on. Waiting time of 10-15 minutes for the optimal release of atoms.
- The absorption of probe is checked in the sensitive photodiode. If the probe is absorbed completely on resonance, the absorption is checked at higher detunings  $\Gamma$ ,  $2\Gamma$ ,  $3\Gamma$  of the probe in steps. In order to increase absorption at each step, the polarization of the blue-detuned dipole beams and sometimes slightly the red-detuned beams have to be adjusted. In addition, the MOT beam colimators are tweaked or sometimes one has to walk the MOT beam/beams while monitoring the cloud in three cameras. The last few lines are repeated in a recursive way to reach high OD  $\gtrsim 50$  to OD  $\sim 100$ .

Thus, we have a trapped ensemble of atoms in the vicinity of the nanofiber. Now depending on the molasses phase, we can probe at  $t_C = t_A + 4.5(11)$  ms (for best possible optical depth) or at later times before the start of the next cycle, see Figure 2.14. If the magnetic field cancellation has been performed for  $t_C = t_A + 4.5$  ms, we can probe at this time in order to have the least decoherence effects coming from residual B field. We briefly explain the measurement of probe pulses before going into the characterization of the trap.

**Probe for OPD vs APD** – The probe pulses are detected with, either sensitive optical photodiode OPD or, avalanche photodiode APD (single-photon counting module) depending on their power. The probe for OPD has power on the order of 0.1 nW and a typical duration of ten or few tens of  $\mu\text{s}$ , see Figure 2.14. Pulses at the single-photon level are used as APD probe. There are N repeated measurements or subsequences within this duration, each subsequence has a pulse (or pulses) with less than a photon per pulse. The length of each subsequence is usually chosen between 1  $\mu\text{s}$  and 10  $\mu\text{s}$  depending on the experiment. Data collected from these N measurements over many MOT cycles are used to construct histograms from photo-detection events.

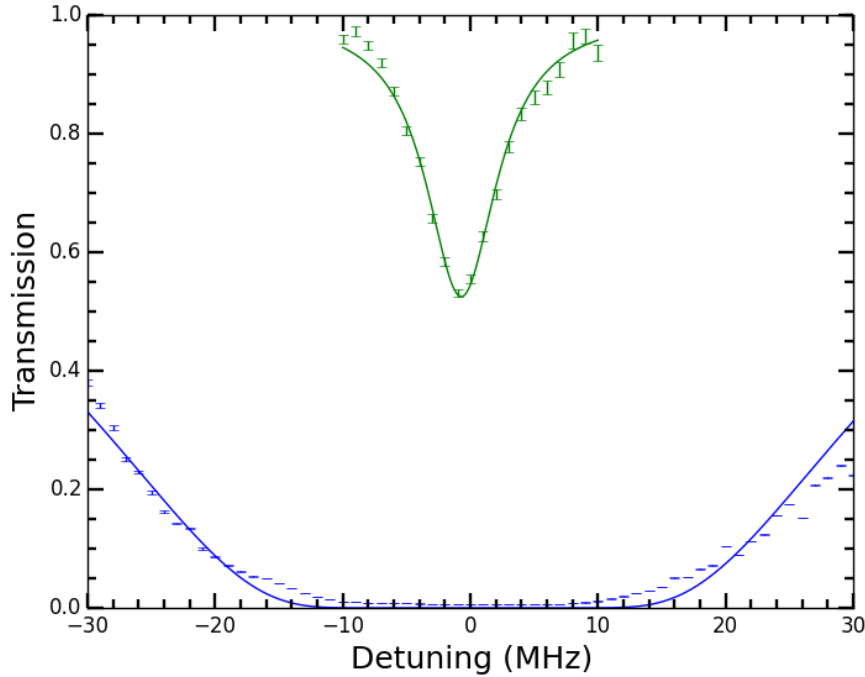


Figure 2.15 – Probe transmission spectra, for trapped atoms close to the nanofiber, as a function of detuning from the  $\{6S_{1/2}, F = 4\} \rightarrow \{6P_{3/2}, F = 5\}$  transition. The high OD curve (blue) is fitted with a Lorentzian profile giving OD=  $105 \pm 15$  for linewidth  $\Gamma/2\pi = 6$  MHz. This value of linewidth is obtained from the low OD curve (green).

The histogram then, gives the probability for a photon detection to occur as a function of time in a single subsequence.

### 2.2.8 Trap characterization

Once, the atoms are trapped close to the nanofiber, one can perform various experiments on this platform. In this section, we give some typical characteristics of our nanofiber trap.

We have changed the nanofiber few times in our setup and the trap obtained with each nanofiber had small differences in trap characteristics, compared to the other. We provide here the general characteristics and the parameters like OD, number of atoms and lifetime values are always on the same order of magnitude. The absorption linewidth or OD curve is based on a measurement with the nanofiber currently used in the experiment. The number of atoms and trap lifetime are measurements done on previous nanofibers.

**Absorption measurement and optical depth (OD)** – The trapping beams are quasi-linearly polarized along  $y$ , see Figure 2.11. The probe has to be aligned along  $y$  to achieve maximum OD. If the probe is aligned along  $x$  (orthogonal to atoms) we

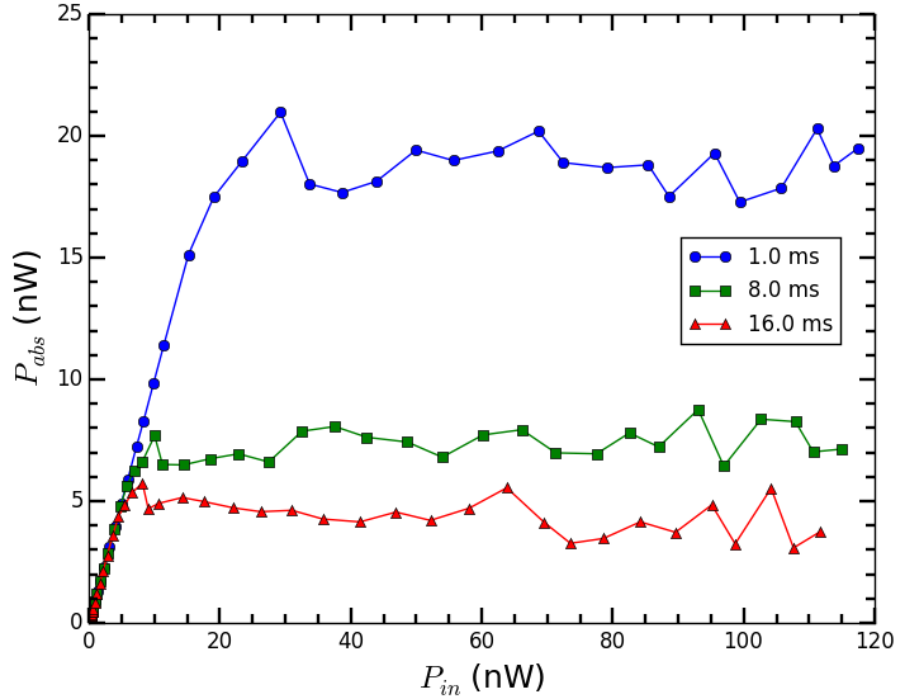


Figure 2.16 – Saturation of absorbed power for a probe on  $\{6S_{1/2}, F = 4\} \rightarrow \{6P_{3/2}, F = 5\}$  transition, for different hold times - 1, 8, 16 ms, as a function of the input power.

reach a relatively low OD, as the light-atom coupling is reduced because of the lower evanescent field intensity along  $y$  for a probe quasi-linearly polarized along  $x$ .

The absorption of a guided probe, addressing  $\{6S_{1/2}, F = 4\} \rightarrow \{6P_{3/2}, F' = 5\}$  transition is shown in Figure 2.15. The measurement done here is with APD for low probe powers (around a photon per pulse). The guided probe is sent as soon as the trap is ready to be probed i.e. at  $t_C = t_A + 4.5(11)$  ms in Figure 2.14. The absorption of a probe (green) at low OD is fitted by a Lorentzian to obtain the linewidth  $\Gamma/2\pi = 6$  MHz of trapped atoms. This value is then used to fit the high OD curve (blue). The OD, in this case, is found to be  $105 \pm 15$ . The absorption profiles are centered and the fact they can be fitted by Lorentzians implies very limited broadening arising from the trap mechanisms. These are the typical signatures of a state-insensitive, compensated trap.

The linewidth of nanofiber trapped atoms has been measured to be more than the linewidth in free space  $\Gamma_0/2\pi = 5.2$  MHz. This broadening of the linewidth is currently under investigation. One possibility is that the atoms are stuck on the nanofiber surface.

**Estimation of number of atoms** – For estimating the number of atoms, we have to saturate the ensemble of atoms with a resonant probe. This comes from the fact

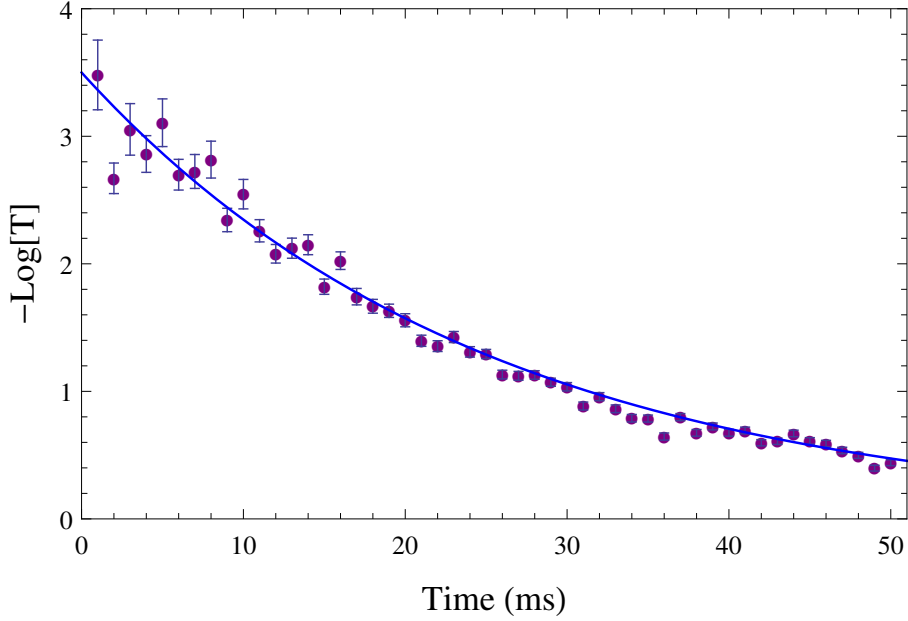


Figure 2.17 – Transmission of a probe plotted as a function of hold time. The probe is detuned by 15 MHz from  $\{6S_{1/2}, F = 4\} \rightarrow \{6P_{3/2}, F = 5\}$  transition. The blue curve is a fitted exponential decay with a time constant of 25 ms.

that a saturated atom can scatter only one photon at a time. Therefore, the number of atoms  $N$  is given by dividing the total absorbed power  $P_{abs}$  with the nominal power  $p$  radiated by a single atom as shown below,

$$P_{abs} = P_{in} - P_{out} = \frac{1}{2} \hbar \omega N \Gamma = pN$$

Figure 2.16 shows saturation profiles for  $\{6S_{1/2}, F = 4\} \rightarrow \{6P_{3/2}, F = 5\}$  probe measured as a function of input power  $P_{in}$  for different probing times. The saturation plot for 1 ms hold time (i.e., time since the trap is loaded) gives the number of trapped atoms. This is calculated from the total absorbed power and the nominal power,  $p = 3.8$  pW for Cs. The number of atoms is  $N = 4800 \pm 200$ . The OD per atom is  $d_1 \simeq 0.02$ . This implies around 2% of resonant light is absorbed by an atom. From other saturation profiles, we see the estimated numbers of atoms decays when probed at longer hold times as the atoms are lost from the trap.

**Lifetime of trap** – The loss of number of atoms in the trap naturally leads to less absorption of a resonant probe with time. However, owing to a high OD the probe will remain completely absorbed for longer times on resonance. Instead, if the absorption measurements are done with a detuned probe, a better signal to noise ratio can be obtained at high OD. Figure 2.17 shows the decay of absorption of a probe, detuned by 15 MHz from resonance, as a function of time after the trap is loaded i.e.,  $t - t_B$  in Figure 2.14. The data points are fitted by an exponential decay, which gives a trap lifetime of about 25 ms. There are two possible factors that can limit the lifetime of the

trap. We do not know which one or if both are in reality affecting our trap. The first one, is the noise coming from intensity and polarization fluctuations in the trapping beams. The second one, is the possibility that the frequency of one of the torsional modes in nanofiber is close to the trap frequency. This would lead to the ejection of atoms because of the excitation of the torsional oscillations [Wuttke13a].

We already observed coherent processes like EIT and realized an optical memory, with few percent efficiency, in our ensemble of trapped atoms (in [Gouraud15] the atoms were not trapped but were moving around in the evanescent field). A part of my PhD work has been to design an electronic circuit for fast switching of current in a pair of coils. The circuit is presented in Appendix C. The motivation behind this work is future implementation of gradient echo memory (GEM) [Sparkes13] in our system. In addition, it could also be used to demonstrate a controlled dephasing and rephasing for single collective excitation [Albrecht15] in future. These experiments, already demonstrated in free-space configuration, would have to be adapted for implementation in our 1D platform.

To conclude, we have shown the implementation of a waveguide QED platform - the state-insensitive nanofiber-mediated dipole trap. We have obtained high optical depth and long lifetime with few thousand trapped atoms that can enable implementation of quantum memory and quantum information protocols. One of the ongoing works is to pump atoms to a given Zeeman sublevel so as to suppress the decoherence coming from residual magnetic field and trap mechanisms.

## Chapter Conclusion

To summarize the chapter in few main points:

- We briefly review the theory of dipole trapping and ac Stark shifts, first for a two-level atom, and then for a multi-level atom. In general, the energy shift is given by different light-shifts, namely - scalar, vector and tensor. These light-shifts limit the coherence properties of an ensemble of trapped atoms.
- The principle of trapping atoms close to a nanofiber, by using a two-color dipole trap, are explained. The atoms are located at every  $\lambda_{red}/2$  distance in a 1D array on both sides of the nanofiber. The lattice sites are approximately 200 nm from the nanofiber surface. The nanofiber trap, like any dipole trap, can be affected by light-shifts that can render the trapped ensemble atoms unsuitable for implementation of quantum memory and information protocols.
- We detail our state-insensitive, compensated trapping scheme and how it helps to cancel some of these shifts. There are no differential scalar shifts because of using magic wavelengths - 686 nm and 935 nm. The vector shifts are nullified by using pairs of counter-propagating dipole trapping beams. This makes the polarization linear for atoms at the lattice sites.
- The description of the experimental interface for combining the cold atoms and the nanofiber is presented. We overlap the atomic cloud and the nanofiber, the polarization inside the nanofiber is aligned and the ensemble is prepared by cancellation of residual magnetic field. We are now ready to implement the dipole trap.
- We describe the various laser systems, optical components, locking systems, filtering systems in our setup. The mixing of different dipole beams and the signal at 852 nm, and the filtering of mW of dipole beams from the signal at single-photon level are the technical aspects crucial to realize and perform experiments on this platform.
- To implement the trap, the trap loading sequence is activated. 4 mW each of blue-detuned light and 500  $\mu$ W each of red-detuned light are coupled into the nanofiber with all their polarizations oriented along a particular axis. The probe is sent in along the same direction. A high optical depth (OD  $\sim$  100) and a long lifetime of  $\sim$  25 ms are obtained for an ensemble of few thousand trapped atoms.

In the next chapter, I will report an experiment performed on this platform. By using close-to-commensurate lattice, we realized an efficient Bragg atomic mirror - an effect arising from the spatial ordering of trapped atoms.

## Chapter 3

# Bragg Reflection from 1D arrays of emitters

In [chapter 2](#), we described the state-insensitive, compensated trapping of atoms near the nanofiber and how it can be useful for implementation of quantum information and quantum memory protocols. In this chapter, the atoms are trapped but without using the state-insensitive, compensated scheme. We are interested in realization of another important capability - the cooperative effects emerging from the spatial ordering of the atoms, when the lattice period is close-to-commensurate with the resonant wavelength. In other words, the wavelengths of red-detuned beams of the lattice are tuned close to the atomic transition to observe Bragg reflection from the 1D arrays.

Bragg reflection or scattering has been largely studied in crystals as well as in multilayer dielectric structures. When the spacing between the layers of scatterers or strings of scatterers are equal to the wavelength of light by which it is probed, then the light reflected from the in-phase scatterers interferes constructively. This is called Bragg condition and it results in a strongly reflected light. With increase in number of scatterers, the Bragg reflection increases initially till it saturates and almost all the incident light intensity will be coherently reflected by the medium.

Bragg reflection has also been observed with ordered cold atoms in free-space, either with three-dimensional [[Weidemuller95](#), [Birk195](#)] or one-dimensional optical lattices [[Slama05](#), [Schilke11](#)]. A reflectance as high as 80% was demonstrated in [[Schilke11](#)]. However, this observation required around  $10^7$  atoms distributed over 7700 layers to reach the regime of multiple reflections. In contrast, in our case we demonstrated that 2000 atoms are sufficient to achieve large reflectance in a waveguide-mediated scenario. This work has been published in [[Corzo16](#)].

In this chapter, we study Bragg reflection from chains of trapped atoms close to the nanofiber. First, we develop a simple model for analyzing the transport properties of an array of emitters. We also discuss how the several factors or mechanisms in the trap would affect our measurements. We explain the experiment and present the results. In the last section, we extend our model to three-level  $\Lambda$  configuration and propose a scheme for realization of controllable Bragg mirror and optical switching at the few-photon level.

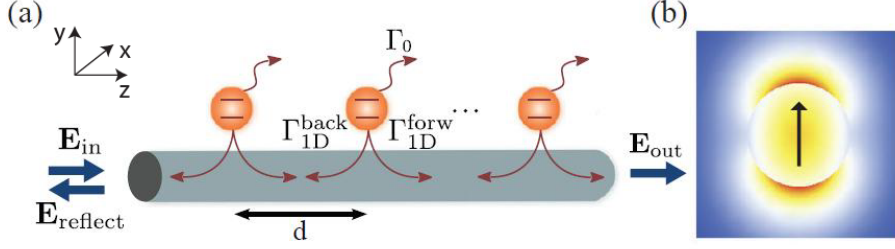


Figure 3.1 – Bragg reflection from atoms coupled to a one-dimensional waveguide. (a)  $N$  atoms, trapped near a waveguide, exhibit radiative decay rates  $\Gamma_{1D}^{\text{forw,back}}$  into the right- and left-propagating modes, and  $\Gamma' \simeq \Gamma_0$  into all the other modes. (b) Electric field distribution in the transverse plane of a nanofiber for a guided probe with a quasilinear polarization (indicated by the arrow).

### 3.1 Bragg reflection based on two-level atoms

We investigate the scattering properties and associated photon transport in a typical configuration as depicted in Figure 3.1.  $N$  atoms are trapped in the vicinity of a waveguide, with a lattice constant  $d$  close to  $\lambda_0/2$ , where  $\lambda_0$  corresponds to the wavelength of the D<sub>2</sub> line of cesium. Each atom exhibits a radiative decay rate  $\Gamma_{1D}^{\text{forw}}$  and  $\Gamma_{1D}^{\text{back}}$  into the right- and left-propagating mode respectively, and  $\Gamma' \simeq \Gamma_0$  into all the other modes.  $\Gamma_0$  is the radiative decay rate in free space. As already discussed in subsection 1.1.3 of chapter 1, the sub-wavelength variations of transverse field components in a nanofiber leads to a significant longitudinal component (relative  $\pi/2$  phase). Due to this complex polarization structure of tightly focused light, the spontaneous emission of atoms into the guided mode is in general not symmetric [Le Kien14a].

Specifically, for a guided probe field quasilinearly polarized along the  $x$ -direction, the two decay rates are equal,  $\Gamma_{1D}^{\text{back}} = \Gamma_{1D}^{\text{forw}} = \Gamma_{1D}/2$ . We call this the symmetric case. For an orientation along the  $y$ -direction, i.e. pointing towards the atoms, the couplings to the waveguide become strongly asymmetric  $\Gamma_{1D}^{\text{back}} \neq \Gamma_{1D}^{\text{forw}}$ . We call this the chiral case. In the case of asymmetric coupling, the forward decay rate is increased by 3-fold while the backward decay rate is suppressed by about one order of magnitude. The two cases can be treated independently since it has been shown that when the ground state Zeeman levels are equally populated, the two  $x$ - and  $y$ -polarization are not coupled to each other by the linear coherent scattering [Le Kien14b].

In the following sections, we study photon transport in a one-dimensional waveguide coupled to a two-level emitter. The expressions for single-atom transmission  $t$  and reflection coefficient  $r$ , for both symmetric and chiral cases are derived following [Shen05]. We then use the transfer matrix formalism to obtain the reflection and transmission spectra for the atomic chains.

#### 3.1.1 Single-atom reflection and transmission coefficients

The transport properties for a two-level system coupled to a 1D continuum will be studied here. This approach is given in [Shen05] and we give the steps here. The

emitter has ground state  $|g\rangle$  and excited state  $|e\rangle$ , with  $\Gamma' \simeq \Gamma_0$  being the spontaneous decay rate into all modes (mainly vacuum modes), except the waveguide mode. The atomic Hamiltonian can be written as:

$$H_{atom}/\hbar = (\omega_e - \omega_g - i\Gamma_0/2) |e\rangle \langle e| = (\omega_0 - i\Gamma_0/2) |e\rangle \langle e|$$

with  $\omega_0 = \omega_e - \omega_g$  being the energy difference between the excited and ground states. The interaction between photons of 1D waveguide and a two-level emitter coupled to the waveguide is described by Dicke Hamiltonian [Dicke54] when expressed in real space with the assumption that the atomic resonance energy is away from the cutoff frequency of the dispersion relation. The dispersion relation of the photon in the waveguide can be linearized with  $\omega \sim v_g|\mathbf{k}|$ ,  $v_g$  being the group velocity of the photons. We define:  $\sigma = |g\rangle \langle e|$  and  $\sigma^\dagger = |e\rangle \langle g|$  as atomic lowering and raising operators respectively. The full Hamiltonian including the atomic part  $H_{atom}$  and the interaction part is then given by,

$$\begin{aligned} \frac{H}{\hbar} = \int dx \left( -iv_g a_R^\dagger \frac{\partial}{\partial x} a_R(x) + iv_g a_L^\dagger \frac{\partial}{\partial x} a_L(x) + V_R \delta(x) [a_R^\dagger(x)\sigma + a_R(x)\sigma^\dagger] \right. \\ \left. + V_L \delta(x) [a_L^\dagger(x)\sigma + a_L(x)\sigma^\dagger] \right) + (\omega_0 - i\Gamma_0/2)\sigma^\dagger\sigma, \end{aligned} \quad (3.1.1)$$

where the bosonic operator  $a_R^\dagger(x)[a_L^\dagger(x)]$  creates a right-going (left-going) photon at  $x$ .  $V_L(V_R)$  is the coupling between the atom and the left-travelling (right-travelling) photons.

Let us suppose the atom is prepared in its ground state. A photon travelling in the waveguide may be absorbed by the atom or scattered into the left- or the right-guided mode of the waveguide. Therefore, the scattering eigenstates of the Hamiltonian (3.1.1) have the form:

$$|\psi\rangle = \int dx [\phi_R(x)a_R^\dagger(x) + \phi_L(x)a_L^\dagger(x)] |0,g\rangle + \phi_e \sigma^\dagger |0,g\rangle,$$

where  $|0,g\rangle$  indicates the vacuum state and atom in ground state  $|g\rangle$ ,  $\phi_e$  is the probability amplitude of the atom to be in the excited state  $|e\rangle$ . By assuming the incident, reflected and transmitted fields to be plane waves one can write,

$$\begin{aligned} \phi_R(x) &= t e^{ikx} \theta(x) + e^{ikx} \theta(-x) \\ \phi_L(x) &= r e^{-ikx} \theta(-x) \end{aligned}$$

where  $t(r)$  is the relevant transmission (reflection) amplitude and  $\theta(x)$  is a step function. The problem can be solved by using the following eigenvalue equation:

$$H |\psi\rangle = \hbar\omega |\psi\rangle = \hbar v_g k |\psi\rangle. \quad (3.1.2)$$

We have commutation relations:  $[a_L(x'), a_L(x)] = \delta(x' - x)$ ,  $[\frac{\partial}{\partial x'} a_L(x'), a_L(x)] = \delta(x' - x)$ . Similar commutation relations hold for right-going  $R$  photons. We write the contributing terms in  $H |\psi\rangle$  as:

$$H |\psi\rangle = (O_1 + O_2 + O_3 + O_4) |0,g\rangle, \quad (3.1.3)$$

where

$$\begin{aligned}
O_1 &= iv_g \int dx \frac{\partial}{\partial x} [\phi_L(x)] a_L^\dagger(x) - iv_g \int dx \frac{\partial}{\partial x} [\phi_R(x)] a_R^\dagger(x) \\
O_2 &= V_L \int dx \phi_L(x) \delta(x) a_L(x) a_L^\dagger(x) \sigma^\dagger + V_R \int dx \phi_R(x) \delta(x) a_R(x) a_R^\dagger(x) \sigma^\dagger \\
O_3 &= V_L \int dx \delta(x) \phi_e a_L^\dagger(x) + V_R \int dx \delta(x) \phi_e a_R^\dagger(x) \\
O_4 &= \phi_e (\omega_0 - i\Gamma_0/2) \sigma^\dagger.
\end{aligned}$$

We look at terms in the sum of  $O_1$  and  $O_3$ . Grouping the terms for propagation to the right and to the left separately we have,

$$\begin{aligned}
& -iv_g \frac{\partial}{\partial x} [\phi_R(x)] + V_R \delta(x) \phi_e \\
&= -iv_g [ik(e^{ikx}\theta(-x) + te^{ikx}\theta(x)) - e^{ikx}\delta(x) + te^{ikx}\delta(x)] + V_R \delta(x) \phi_e \\
&= kv_g \phi_R(x) - iv_g t e^{ikx} \delta(x) + iv_g e^{ikx} \delta(x) + V_R \delta(x) \phi_e
\end{aligned} \tag{3.1.4}$$

and

$$\begin{aligned}
& iv_g \frac{\partial}{\partial x} [\phi_L(x)] + V_L \delta(x) \phi_e \\
&= iv_g [-ikre^{-ikx}\theta(-x) - re^{-ikx}\delta(x)] + V_L \delta(x) \phi_e \\
&= kv_g \phi_L(x) - iv_g r e^{-ikx} \delta(x) + V_L \delta(x) \phi_e.
\end{aligned} \tag{3.1.5}$$

The first term of Eq. (3.1.4) and Eq. (3.1.5) when added together looks like

$$\begin{aligned}
& kv_g \left[ \int dx \phi_L(x) a_L^\dagger(x) + \int dx \phi_R(x) a_R^\dagger(x) \right] |0, g\rangle \\
&= \omega |\psi\rangle - \omega \phi_e \sigma^\dagger |0, g\rangle.
\end{aligned}$$

This gives eigenvalue equation Eq. (3.1.2) minus the term  $\omega \phi_e \sigma^\dagger |0, g\rangle$ , which is taken care of later in Eq. (3.1.8). The rest of the terms in Eq. (3.1.4) and Eq. (3.1.5) should add up to zero as they create right-travelling (left-travelling) photons, thereby altering the eigenstate  $|0, g\rangle$ . This yields

$$-iv_g t e^{ikx} \delta x + iv_g e^{ikx} \delta(x) + V_R \delta(x) \phi_e = -iv_g r e^{-ikx} + V_L \delta(x) \phi_e = 0$$

Integrating with respect to  $x$ ,

$$\begin{aligned}
& -iv_g t + iv_g + V_R \phi_e = 0 \\
\Rightarrow \quad t &= 1 - \frac{iV_R \phi_e}{v_g},
\end{aligned} \tag{3.1.6}$$

$$\begin{aligned}
& -iv_g r + V_L \phi_e = 0 \\
\Rightarrow \quad r &= -\frac{iV_L \phi_e}{v_g}.
\end{aligned} \tag{3.1.7}$$

Equating the coefficients of  $\sigma^\dagger$  on both sides of Eq. (3.1.3)

$$O_2 + (\omega_0 - i\frac{\Gamma_0}{2})\phi_e = \omega\phi_e \quad (3.1.8)$$

$$V_R \left( \frac{1+t}{2} \right) + V_L \frac{r}{2} + (\omega_0 - i\frac{\Gamma_0}{2})\phi_e = \omega\phi_e, \quad (3.1.9)$$

since

$$\begin{aligned} O_2 &= V_R \int dx \delta(x) [te^{ikx}\theta(x) + e^{ikx}\theta(-x)] + V_L \int dx \delta(x)\theta(-x)re^{-ikx} \\ &= V_R \left( \frac{1+t}{2} \right) + V_L \frac{r}{2} \quad (\text{with } \theta(0) = 1/2). \end{aligned} \quad (3.1.10)$$

Substituting Eq. (3.1.6) and Eq. (3.1.7) into Eq. (3.1.9), we can find  $\phi_e$  and hence derive expressions for  $t$  and  $r$ .

The atom effectively has two channels of decay  $\Gamma = \Gamma_{1D} + \Gamma'$  that can be associated with the guided mode  $\Gamma_{1D}$  and the radiation modes  $\Gamma' \sim \Gamma_0$  where  $\Gamma_0$  is the radiative decay in free-space. The decay to the guided mode can occur in forward  $\Gamma_{1D}^{forw}$  and backward  $\Gamma_{1D}^{back}$  directions. The atom-waveguide coupling constants  $V_L$  and  $V_R$  are proportional to dipole matrix elements of the transition, which can be related to the spontaneous decay rates into the waveguide. We now detail the two specific cases:

**Symmetric case** – In this case, the coupling of atom to the waveguide is same in both directions, left and right i.e.  $V_R = V_L = V$ . We recognize the spontaneous emission rate into the waveguide as

$$\frac{\Gamma_{1D}}{2} = \frac{V^2}{v_g}.$$

Using Eq. (3.1.6), Eq. (3.1.7) and Eq. (3.1.9) we get,

$$\phi_e = \frac{V}{(\omega - \omega_0 + i\Gamma_0/2) + i\Gamma_{1D}/2}.$$

Therefore, the reflection and transmission coefficients are expressed as:

$$\begin{cases} r(\delta) = \frac{-\Gamma_{1D}}{\Gamma - 2i\delta}, \\ t(\delta) = \frac{\Gamma_0 - 2i\delta}{\Gamma - 2i\delta} = 1 + r(\delta), \end{cases} \quad (3.1.11)$$

where  $\Gamma = \Gamma_0 + \Gamma_{1D}$  and  $\delta = \omega - \omega_0$  is the detuning from atomic resonance.

**Chiral case** – In this case, the coupling of atom to waveguide is different in two directions, i.e.  $V_L$  and  $V_R$  for left and right propagation respectively. We recognize the forward and backward spontaneous emission rates into waveguide as

$$\Gamma_{1D}^{forw} = \frac{V_R^2}{v_g}; \quad \Gamma_{1D}^{back} = \frac{V_L^2}{v_g}.$$

In a similar way,

$$\phi_e = \frac{2V_R}{2(\omega - \omega_0 + i\Gamma_0/2) + i\Gamma_{1D}^{forw} + i\Gamma_{1D}^{back}}.$$

Similarly, the coefficients are expressed as:

$$\begin{cases} r(\delta) = \frac{-2\sqrt{\Gamma_{1D}^{forw} \cdot \Gamma_{1D}^{back}}}{\Gamma - 2i\delta}, \\ t(\delta) = 1 - \frac{2\Gamma_{1D}^{forw}}{\Gamma - 2i\delta} \neq 1 + r(\delta), \end{cases}$$

where  $\Gamma = \Gamma_0 + \Gamma_{1D}^{forw} + \Gamma_{1D}^{back}$  and  $\delta = \omega - \omega_0$  is the detuning from atomic resonance.

The single-atom transmission and reflection coefficients derived here are valid for a two-level atom. Our experiment, however does not resemble this situation as we do not split the Zeeman sublevels by an external magnetic field in order to have an effective two-level atom. Thus, we need a full microscopic treatment taking into account all Zeeman energy sublevels and such a treatment has been carried out in [Le Kien14b]. In this involved approach, atoms are distributed in different Zeeman sublevels and all possible transitions are considered, for example a photon emitted because of decay of an atom from an excited Zeeman sublevel can cause excitation of another atom in a different Zeeman sublevel and so on. The single-atom transmission and reflection coefficients obtained from this treatment are same as derived here for the symmetric case but different for the chiral case. The coefficients for the chiral case are written as:

$$\begin{cases} r(\delta) = \frac{-2\sqrt{\Gamma_{1D}^{forw} \cdot \Gamma_{1D}^{back}}}{\Gamma - 2i\delta}, \\ t(\delta) = 1 - \frac{(\Gamma_{1D}^{forw} + \Gamma_{1D}^{back})}{\Gamma - 2i\delta} \neq 1 + r(\delta). \end{cases} \quad (3.1.12)$$

### 3.1.2 Spectra simulation

After having defined the single-atom reflection and transmission coefficients, we now investigate the light propagation through a one-dimensional chain, as illustrated in Figure 3.1. It can be described by the transfer matrix formalism [Deutsch95]. For an atom at position  $z$  one can introduce the matrix  $M_a$  that relates components of the backward- and forward-traveling electric field on the right side  $E_R^{back}$  and  $E_R^{forw}$  to the ones on the left side  $E_L^{back}$  and  $E_L^{forw}$ :

$$\begin{pmatrix} E_L^{back} \\ E_L^{forw} \end{pmatrix} = M_a \cdot \begin{pmatrix} E_R^{back} \\ E_R^{forw} \end{pmatrix}. \quad (3.1.13)$$

From Figure 3.2, for each atomic plane we have:

$$E_R^{forw} = rE_R^{back} + tE_L^{forw} \quad (3.1.14)$$

$$E_L^{back} = tE_R^{back} + rE_L^{forw}, \quad (3.1.15)$$

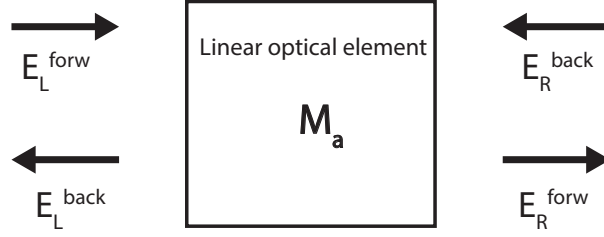


Figure 3.2 – Transfer matrix  $M_a$  relates the forward and backward propagating waves on the left side of an arbitrary linear optical element to those on the right side. This provides a simple method to calculate the propagation of waves through a series of such optical elements by taking into account multiple reflections and interference effects. The reflection and transmission coefficients associated with the entire element can be expressed in terms of the transfer matrix elements.

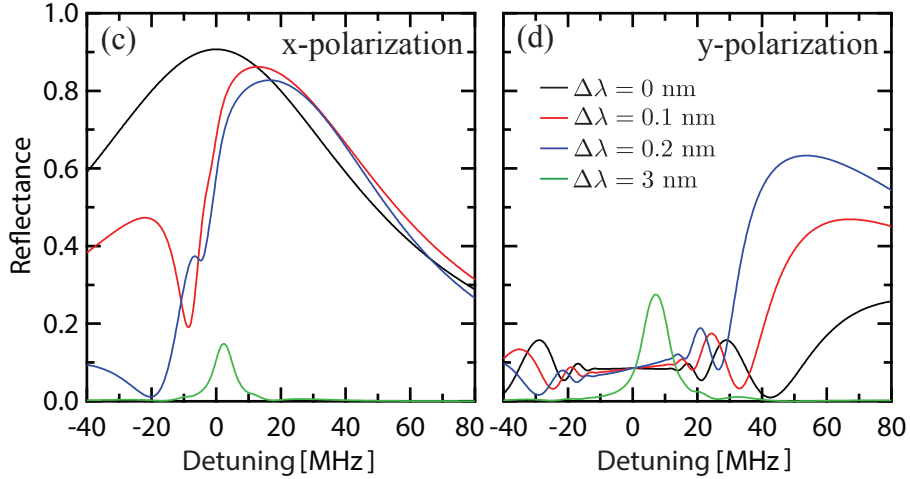


Figure 3.3 – (a) Theoretical reflection spectra for a probe quasilinearly polarized along the  $x$ -direction (symmetric decay rates) and (d) along the  $x$ -direction (asymmetric decay rates). The spectra are given for different distances  $d$  between the atoms, with values close to the commensurate case.  $\Delta\lambda$  stands for the trap detuning to resonance, with  $d = \lambda_0/2 + \Delta\lambda/2$ . ( $N = 2000$ ,  $\Gamma_{1D}/\Gamma_0 = 0.01$ ,  $\Gamma_{1D}^{\text{forw}} = 2.8\Gamma_{1D}$ ,  $\Gamma_{1D}^{\text{forw}}/\Gamma_{1D}^{\text{back}} = 12$ ). Theoretical values of the couplings are taken from [Le Kien14a].

where  $t$  and  $r$  are single-atom transmission and reflection coefficients respectively. Rearranging Eq. (3.1.14) and Eq. (3.1.15) we get,

$$E_L^{\text{forw}} = \frac{-r}{t} E_R^{\text{back}} + \frac{1}{t} E_R^{\text{forw}}$$

$$E_L^{\text{back}} = \frac{(t^2 - r^2)}{t} E_R^{\text{back}} + \frac{r}{t} E_R^{\text{forw}}.$$

Therefore, we obtain the following expression for the matrix  $M_a$  defined in Eq. (3.1.13),

$$M_a = \frac{1}{t} \begin{pmatrix} t^2 - r^2 & r \\ -r & 1 \end{pmatrix}. \quad (3.1.16)$$

The transfer matrix  $M_p$  for propagation between neighboring atoms is simply given by

$$M_p = \begin{pmatrix} e^{ikd} & 0 \\ 0 & e^{-ikd} \end{pmatrix},$$

where  $d$  is the distance between the two atoms. The transfer matrix for the full ensemble is obtained as a product of matrices  $M_a$  and  $M_p$  as follows:

$$M = \begin{pmatrix} M_{11} & M_{12} \\ M_{21} & M_{22} \end{pmatrix} = (M_a \cdot M_p)^N.$$

The transmission and reflection coefficients of the atomic chain are finally given by:

$$\begin{aligned} T &= \left| \frac{1}{M_{22}} \right|^2 \\ R &= \left| \frac{M_{12}}{M_{22}} \right|^2. \end{aligned}$$

In the symmetric case, the reflection and transmission coefficients are given by Eq. (3.1.11). In accordance with Eq. (3.1.16) the explicit expression of the transfer matrix  $M_a$  can be written as follows:

$$M_a = \frac{1}{\Gamma_0 - 2i\delta} \begin{pmatrix} \frac{(\Gamma_0 - 2i\delta)^2 - \Gamma_{1D}^2}{\Gamma - 2i\delta} & -\Gamma_{1D} \\ \Gamma_{1D} & \Gamma - 2i\delta \end{pmatrix}.$$

In the asymmetric case, the reflection and transmission coefficients are given by Eq. (3.1.12). These expressions finally provide the transfer matrix  $M_a$ :

$$M_a = \frac{1}{\Gamma_0 - 2i\delta} \begin{pmatrix} \frac{(\Gamma_0 - 2i\delta)^2 - 4\Gamma_{1D}^{forw} \cdot \Gamma_{1D}^{back}}{\Gamma - 2i\delta} & -2\sqrt{\Gamma_{1D}^{forw} \cdot \Gamma_{1D}^{back}} \\ 2\sqrt{\Gamma_{1D}^{forw} \cdot \Gamma_{1D}^{back}} & \Gamma - 2i\delta \end{pmatrix},$$

Using these transfer matrices, we simulate the reflectance (or reflection coefficient) of the full atomic chain of 2000 atoms as a function of the detuning  $\delta$  from the atomic resonance. Figure 3.3(a) and Figure 3.3(b) provide theoretical reflection spectra for different small wavelength detunings  $\Delta\lambda$  of the trap wavelength to atomic resonance and for the two orthogonal polarizations. For atoms separated exactly by  $\lambda_0/2$ , the reflection spectrum is a broadened Lorentzian in the symmetric coupling case while the reflectance is strongly suppressed in the chiral one. Indeed, the amount of chirality and number of atoms result in a finite bandwidth around resonance where reflection is suppressed, as detailed in [Le Kien14b]. For close-to-commensurate traps i.e.,  $\Delta\lambda = 0.1, 0.2$  nm as studied here, the Bragg condition is fulfilled out of resonance. This leads to a maximum reflectance shifted to the blue [Schilke11] but also results in an increased reflectance for the chiral case. Large reflectance values can then be obtained for both polarizations as the single-atom reflection coefficients are similar in our configuration.

## 3.2 Simulating the factors that affect Bragg reflection

We now include various factors or parameters in our model, that can affect the transport properties of the trapped chain of atoms. We explore how these parameters will affect the Bragg reflection and in turn help us understand the experimental data presented in the subsequent section.

### 3.2.1 Effect of inhomogeneous broadening

As already mentioned in this specific experiment, the atoms are not trapped by a state-insensitive compensated trapping scheme. As a result, the dipole trapping of the atoms can result in a resonance shift and an inhomogeneous broadening. This effect is limited in the reported experiment: the shift has been measured equal to 3 MHz and the broadening to  $\sigma_\delta \sim 3$  MHz. To study the effect of these parameters, we vary randomly the detuning for each atom of the chain,  $\delta_i = \delta + \delta_{b_i}$  in accordance with the Gaussian distribution:

$$f(\delta_b) = \frac{1}{\sqrt{2\pi\sigma_\delta^2}} e^{-\frac{\delta_b^2}{2\sigma_\delta^2}}$$

where  $\sigma_\delta$  is the standard deviation. Each atom has an individual transfer matrix  $M_{a_i}$  and the total transfer matrix for the chain can be read as:

$$M = (M_{a_1} \cdot M_p) \cdot (M_{a_2} \cdot M_p) \cdot \dots \cdot (M_{a_N} \cdot M_p).$$

Figure 3.4 provides the simulations of the reflexion spectra for different broadenings  $\sigma_\delta$ . The measured broadening has indeed small effect, below what can be measured given the precision of our measurements.

### 3.2.2 Effect of disorder induced by the filling factor

The filling factor of the trapping sites can induce randomness in the distribution of the atoms across the lattice. We consider here two parallel lines of atoms, as obtained with a nanofiber, with at most one atom per site. Given a filling factor per site  $f$ , at each trapping axial position, there are either no atom at all, one atom on the upper chain, one atom on the lower chain or one atom in both upper and lower chains. This situation can be simulated by a single random array of  $N/2f$  lattice sites ( $N$  is number of atoms), for each site, either no atom (probability  $(1 - f)^2$ ), one atom (probability  $2f(1 - f)$ ) or two atoms (probability  $f^2$ ).

As shown in Figure 3.5, a filling factor of 50%, which is the ideal case in the collisional blockade regime, leads here to the same spectrum than a full single array for the same number of atoms. When the filling factor decreases, the spectrum is narrower and the maximum reflection decreases.

### 3.2.3 Trapping potential and effect of disorder induced by imperfect axial localization

Following the calculation presented in [Lacroute12, Le Kien13] and in collaboration with A. Goban, we calculated the trapping potential and trapping frequency in the axial

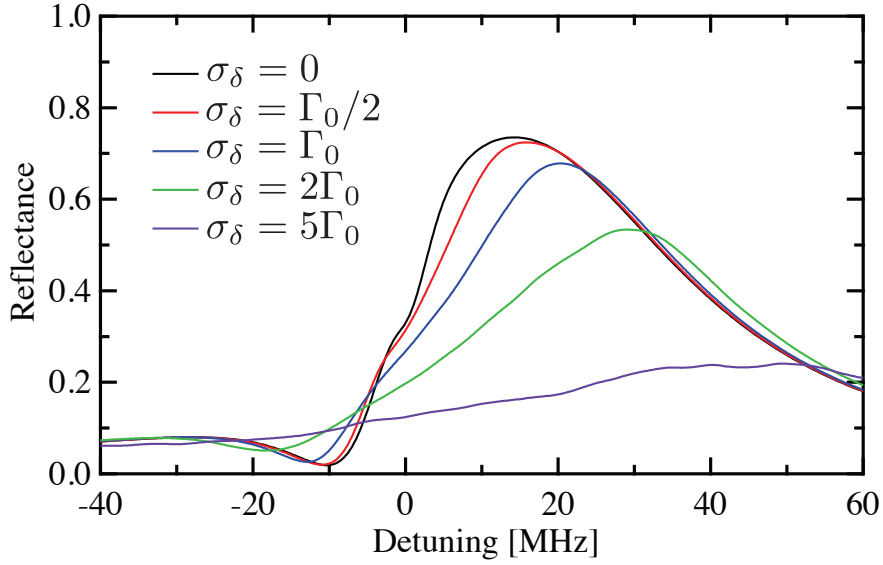


Figure 3.4 – Simulated reflection spectra for a probe quasilinearly polarized along the  $x$ -direction (symmetric decay rates) and different inhomogeneous broadening  $\sigma_\delta$ . The trap detuning is  $\Delta\lambda = 0.2$  nm, the number of atoms  $N = 2000$  and the decay rate  $\Gamma_{1D}/\Gamma_0 = 0.007$ . The spectra are averaged over 15 realizations.

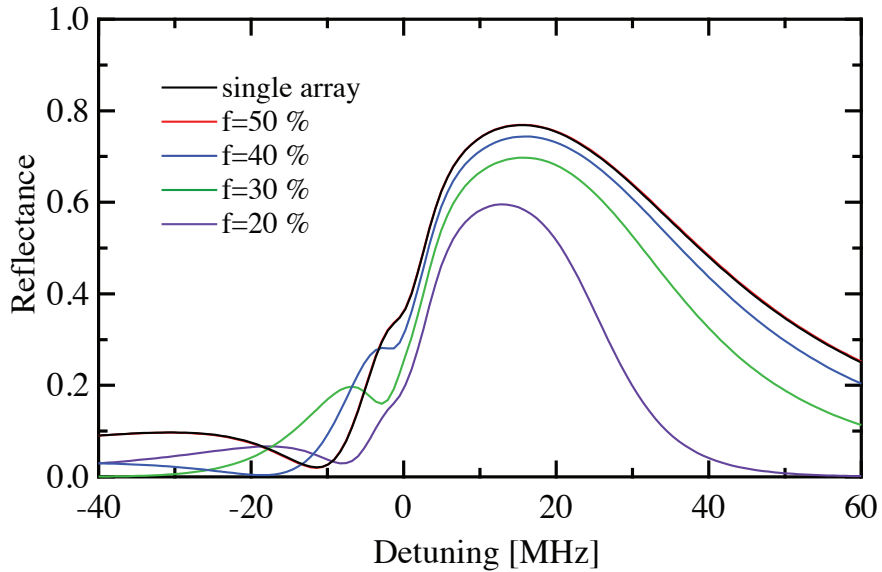


Figure 3.5 – Simulated reflection spectra for a probe quasilinearly polarized along the  $x$ -direction (symmetric decay rates) and a given filling factor  $f$  of each trapping site. We consider two parallel arrays. The trap detuning is  $\Delta\lambda = 0.2$  nm, the number of atoms  $N = 2000$  and the decay rate  $\Gamma_{1D}/\Gamma_0 = 0.007$ . The spectra are averaged over 15 realizations.

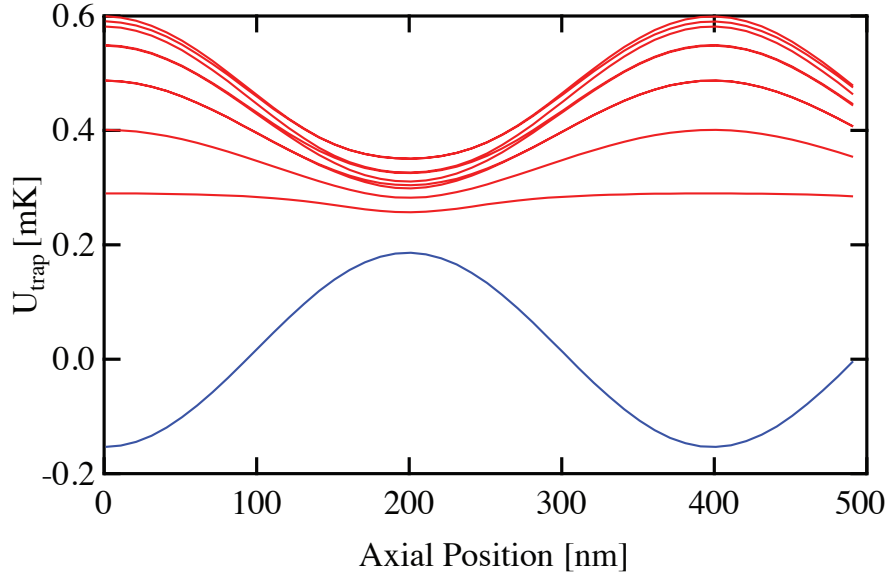


Figure 3.6 – Adiabatic trapping potential  $U_{trap}(z)$  for the near resonant trap for Cs atoms outside a cylindrical waveguide of 200 nm radius. Here,  $\Delta\lambda = 0.2$  nm and the red-detuned trapping power is  $2 \times 1.9\mu\text{W}$ . The power of each blue-detuned fields at 686.1 nm and 686.5 nm is 4 mW. Blue line corresponds to the axial potential for the ground state manifold  $6S_{1/2} F = 4$ , while the red lines correspond to the substates of the excited state  $6P_{3/2} F' = 5$ .

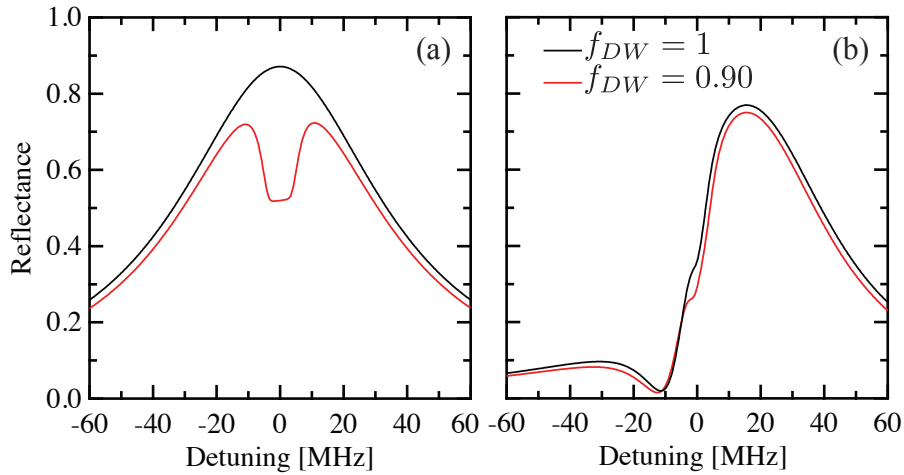


Figure 3.7 – Simulated reflection spectra for a probe quasilinearly polarized along the  $x$ -direction (symmetric decay rates) with and without spread of the atoms in the potential wells. (a) corresponds to on-resonance trap while (b) corresponds to our experimental case with  $\Delta\lambda = 0.2$  nm. The Debye-Waller factor of 0.9 corresponds here to  $\sigma_z \sim 22$  nm, as estimated from the temperature of the atoms and the simulated trap axial frequency. The number of atoms is  $N = 2000$  and the decay rate is  $\Gamma_{1D}/\Gamma_0 = 0.007$ . The spectra are averaged over 15 realizations.

direction. Figure 3.6 shows the axial dependence of the trapping potential  $U_{\text{trap}}(x_0, y = 0, z)$  for atoms trapped at a distance  $x_0 = 234$  nm from the fiber surface. The  $U_{\text{trap}}$  values for the  $\{6S_{1/2}, F = 4\}$  ground state manifold and  $\{6S_{1/2}, F' = 5\}$  excited state manifold are plotted as blue and red lines respectively. For this calculation, we use  $\Delta\lambda = 0.2$  nm and a power of  $2 \times 1.9$   $\mu\text{W}$  for the red detuned beams, and a power of  $2 \times 4$  mW for the blue detuned beams. The potential depth at minimum is  $U_{\text{min}} = -0.15$  mK and the trap frequency in the axial direction is  $\nu_z/2\pi = 258$  kHz.

In the case of  $\Delta\lambda = 0.12$  nm and a trapping power of  $2 \times 1$   $\mu\text{W}$ , the potential depth at minimum is  $U_{\text{min}} = -0.1$  mK and the axial trap frequency is reduced to  $\nu_z/2\pi = 215$  kHz. Both axial frequencies for this near resonant trap are comparable with previous nanofiber-based traps [Goban12, Vetsch12].

Using these calculated frequencies, we compute the root mean square of the spatial spread in the axial direction in the harmonic approximation:

$$\sigma_z = \sqrt{(k_B T)/(m_{Cs} \nu_z^2)},$$

where  $k_B$  is Boltzmann constant,  $T$  is the temperature,  $m_{Cs}$  is the Cesium atomic mass and  $\nu_z$  is the axial frequency of the trap. In our case, the temperature of the atomic cloud is estimated to  $T = 20$   $\mu\text{K}$  from a time-of-flight measurement. Thus,  $\sigma_z$  is equal to 22 nm and 26 nm for  $\Delta\lambda = 0.2$  nm and  $\Delta\lambda = 0.12$  nm respectively. For atoms cooled in the ground state, the axial spread would be 12 nm and 13 nm.

The reduction of Bragg reflected intensity due the spread of the atomic position in the potential wells is usually estimated by a so-called Debye-Waller factor [Ashcroft76, Deutsch95]. This factor is given by  $f_{DW} = e^{-4k^2\sigma_z^2}$ , where  $k$  is the guided mode wavenumber. In our case, we find values of 0.89 and 0.85 for  $\Delta\lambda = 0.2$  nm and  $\Delta\lambda = 0.12$  nm respectively (0.96 for atoms cooled to the motional ground state). In Figure 3.7, we provide the simulated spectra taking into account a Gaussian spread  $\sigma_z$  for the atom position. As it can be seen, this close-to-unity Debye Waller factor has a very limited effect in our configuration where Bragg reflection is obtained out of resonance while it would be an important factor close to resonance [Slama06]. If the reduction in Bragg reflection would be equal to the Debye-Waller factor, it would imply we are in the single-scattering regime. However, we note that the reduction at resonance is larger than the Debye-Waller factor in our simulated spectra. This implies we begin to be in the multiple-scattering regime. The dip on resonance for the Bragg reflection spectra can be explained as follows.

The local axial disorder translates into a residual absorption that can manifest close to resonance by a dip in the spectra. Because of absorption only atoms at the beginning of the chain (not the full atomic chain) contributes to the Bragg reflection and hence the dip. However, for Bragg reflection out of resonance, the local disorder, which is few tens of nanometers, is a minor disorder compared to the phase mismatch accumulated over few hundred nanometers between the first atoms and last atoms of the chain. Therefore, imperfect axial localization does not have much effect in the Bragg reflection spectra for close-to-commensurate arrays.

After calculating the achievable reflectance and the effect of various experimental parameters, we now turn to the experimental realization.

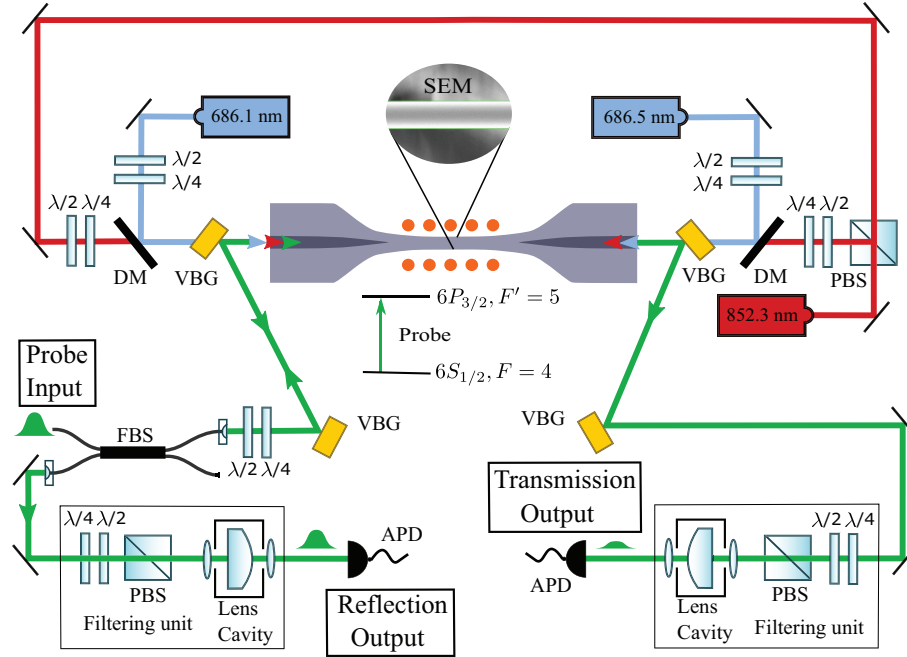


Figure 3.8 – Experimental setup for Bragg reflection. Cesium atoms, around 2000, are trapped in two parallel 1D arrays in the evanescent field of a nanofiber. The lattice is realized by a pair of close-to-resonance red-detuned counterpropagating beams. An additional pair of blue-detuned beams with slightly different wavelengths gives a repulsive contribution. The atoms are prepared in the  $|g\rangle = \{6S_{1/2}, F = 4\}$  ground state and the probe addresses the transition  $|g\rangle \rightarrow |e\rangle = \{6P_{3/2}, F' = 5\}$ . Reflection and transmission spectra are measured with avalanche photodiodes (APDs) after polarization and frequency filterings. DM stands for dichroic mirror, FBS for fiber beamsplitter and VBG for volume Bragg grating.

### 3.3 Experimental setup

The experimental setup is similar to what has been described in subsection 2.2.4 of chapter 2. We mention only the additional changes made to the setup for the implementation of Bragg reflection. The nanofiber used in this experiment is produced from the single-mode fiber OZ Optics SMF-780-5/125 compared to the usual Thorlabs SM800-5.6-125. A fiber beam splitter (FBS) is used for the separation of probe input from the reflected pulse as shown in Figure 3.8. The filtering units before the detection system at the transmission and reflection outputs are crucial for this experiment. This is because the red-detuned dipole beams, detuned  $\Delta\lambda = 0.12, 0.2$  nm away from the atomic resonance, are only partly filtered by VBGs. Milliwatts of red-detuned dipole beams are filtered out efficiently from the probe at the single photon level thanks to the filter cavities. The weak probe pulse arriving on the atoms has a mean photon number of  $2 \pm 0.05$ . A power of  $2 \times 1 \mu\text{W}$  and  $2 \times 1.9 \mu\text{W}$  for  $\Delta\lambda = 0.12$  nm and  $\Delta\lambda = 0.2$  nm respectively are used for the counter-propagating red detuned beams. A power of  $2 \times 4$  mW is used for the counter-propagating blue detuned beams with slightly

different wavelengths, namely 686.1 nm and 686.5 nm, are used to trap the atoms in the nanofiber vicinity. Simulation of the trapping potential was given previously in subsection 3.2.3.

To measure the reflection and transmission spectra, a probe pulse first passes through the FBS and without atoms will be detected at the transmission-output APD. With atoms, the pulse will be reflected back in the same mode through the FBS detected at the reflection-output APD. The reflectance values are obtained by comparing the reflected pulse when atoms are trapped to the transmitted pulse without atoms, and by correcting for the different losses in the system. These losses, which are detuning-dependent due to the filtering cavities, are calibrated before and after each measurement. The transmittance values are obtained by comparing the transmitted pulse with and without trapped atoms. Error bars in the data include the calibration uncertainties.

### 3.4 Experimental results

We first characterize the reflection and transmission spectra for a probe quasilinearly polarized along the  $x$ -direction. In this configuration, the radiative decay rates are expected to be symmetric. The measurements are given in Figure 3.9 for the two different detunings of the dipole trap. For  $\Delta\lambda = 0.12$  nm, as shown in Figure 3.9(a), we observe a broad reflection spectrum, with a maximum reflectance of  $(0.65 \pm 0.05)$  for a detuning of 25 MHz. For  $\Delta\lambda = 0.2$  nm, the reflection peak is narrower and the maximum reflectance  $(0.65 \pm 0.04)$  is shifted to a lower frequency, see Figure 3.9(b).

The spectra resulting from the two trapping distances are well explained by our simple theoretical model, as presented in Figure 3.9(c) and Figure 3.9(d). The model has been described in section 3.1. In this model, we take into account the disorder in the distribution of the atoms along the two parallel arrays due to a limited filling factor  $f$  of the individual trapping sites, as explained in subsection 3.2.2. The coupling to the waveguide  $\Gamma_{1D}/\Gamma_0 = 0.007$  and the filling factor  $f = 0.3$  have been adjusted to provide the best fit to the spectra of Figure 3.9(a). Larger  $f$  values would lead to a pronounced dip on the reflection spectrum while smaller values result in a strongly reduced reflectance and a narrowing of the spectra width. The simulations take also into account the shift induced by the dipole trapping. Inhomogeneous broadening is not included as the limited broadening  $\sigma$  leads to a negligible modification of the spectra, as discussed in subsection 3.2.1.

The trap loading sequence is same as described in subsection 2.2.6 of chapter 2. After 10 ms molasses phase, the trap is loaded. The measurements described above were performed 1 ms after loading the trap. We now investigate the reflection for longer trapping time (i.e. probing at 2, 3, 4, ... ms after the trap is loaded) and compare its decay with the trap lifetime. Figure 3.10 shows the maximal reflectance and optical depth of the medium as a function of the hold time. Using exponential fits, we obtain a decay time of 2.7 ms and 1.9 ms respectively. From the measured optical depth, we then estimate the number of remaining trapped atoms at each time. The inset in Figure 3.10 provides the maximal reflectance as a function of this inferred atom number. The green line takes into account a random loss of the atoms from the initial

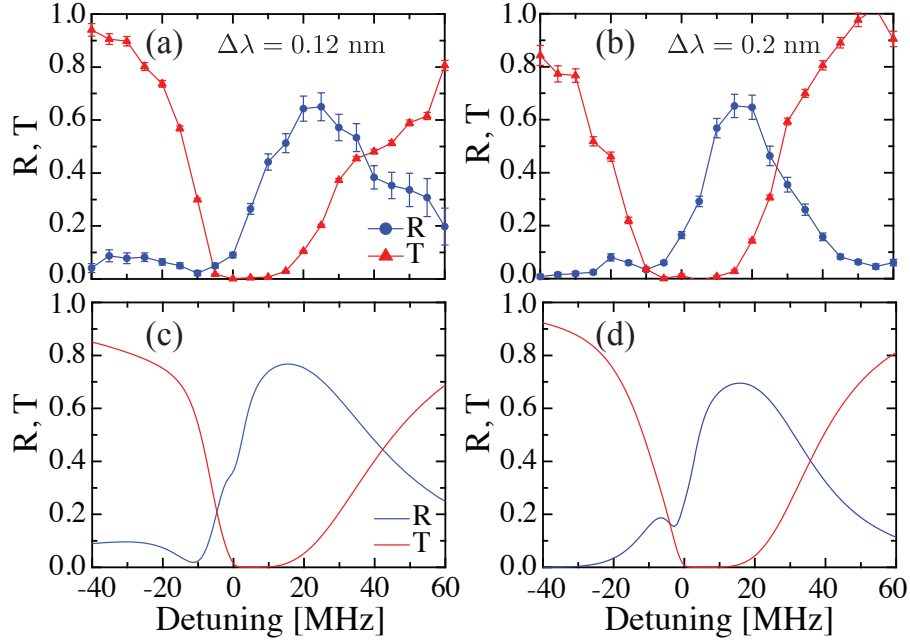


Figure 3.9 – Reflection and transmission spectra for a probe quasilinearly polarized along the  $x$ -direction. (a) and (b) Experimental results for  $\Delta\lambda = 0.12$  nm and  $\Delta\lambda = 0.2$  nm. (c) and (d) Simulated spectra for  $N = 2000$  atoms,  $\Gamma_{1D}/\Gamma_0 = 0.007$  and a filling factor of the lattice sites  $f = 0.3$ . The coupling value and filling factor have been adjusted to fit the measured spectra reported in (a).

arrays with a total atom number of 2000 and a filling factor  $f = 0.3$ . The random loss of atoms from the initial array of trapped atoms has been modelled by introducing a loss factor  $\eta$  that will decrease the filling factor. For the simulation, we started from two parallel arrays with a filling factor  $f$  and subsequently added random loss of the atoms. If one denotes  $1 - \eta$  the probability for an atom to be lost, the new probability for having one atom is  $2\eta f(1 - \eta f)$  and for two atoms  $\eta^2 f^2$ . This model agrees well with the data.

The trap lifetime here is few milliseconds less than the lifetime 20-25 ms (remember Figure 2.17) obtained for state-insensitive, compensated trapping. In this scheme, we reached sufficiently high optical depth ( $OD \approx 35$ ), in other words we trapped enough atoms, for observing a strong Bragg reflection. We see the maximal reflectance, inset in Figure 3.10, already reaches a plateau with number of trapped atoms increased. This implies, Bragg reflection will not be enhanced by adding more atoms to the atomic chains.

Finally, we investigate the effect of the chiral character of the waveguide. The previous measurements were realized with the  $x$ -polarization, which leads to symmetric decay rates for the backward and forward scattering. We now consider the asymmetric case. This situation can be obtained with a probe quasilinearly polarized along the  $y$ -direction. The measured reflection spectra for both probe polarizations are compared in Figure 3.11(a). The trap detuning is fixed at  $\Delta\lambda = 0.2$  nm. As it can be seen, the spectrum is significantly shifted and broadened in the asymmetric case. These features

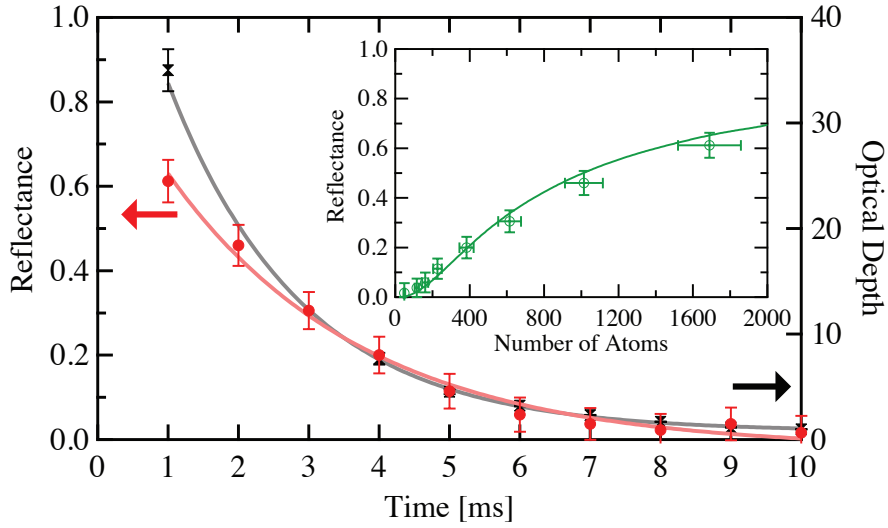


Figure 3.10 – Decay of the reflectance with trapping time and atom number. The largest measured reflectance (red) and the optical depth of the medium at resonance (black) are given as a function of the trapping time. The solid lines are exponential decay fits. The inset provides the reflectance as a function of the remaining number of trapped atoms. The green line is given by a simple model taking into account an initial filling factor  $f = 0.3$  and subsequent random loss ( $\Delta\lambda = 0.2$  nm,  $\Gamma_{1D}/\Gamma_0 = 0.007$ ).

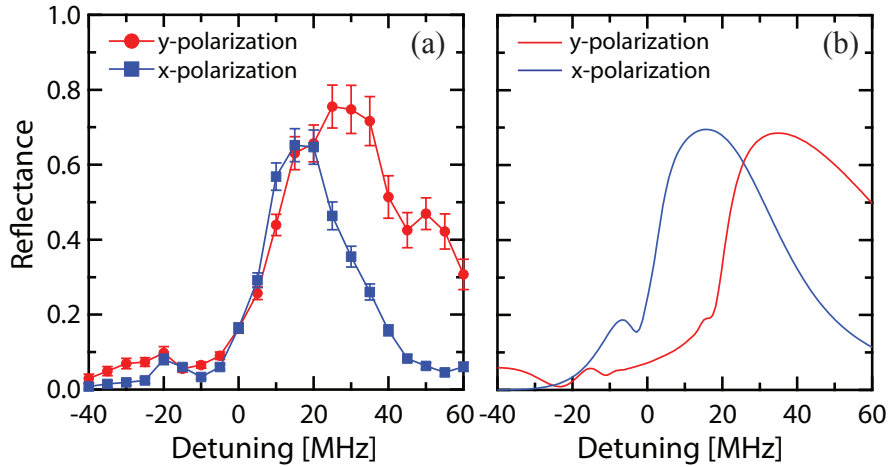


Figure 3.11 – Effect of the chiral character of the waveguide on Bragg reflection. (a) Measured reflection spectra for  $x$ - and  $y$ -quasilinear polarization, with  $\Delta\lambda = 0.2$  nm. (b) Theoretical simulations ( $N = 2000$ ,  $\Gamma_{1D}/\Gamma_0 = 0.007$ ,  $\Gamma_{1D}^{\text{forw}} = 2.8\Gamma_{1D}$ ,  $\Gamma_{1D}^{\text{forw}}/\Gamma_{1D}^{\text{back}} = 12$ ,  $f = 0.3$ ).

are compelling signatures of the chiral character of the waveguide on the reflection, as confirmed by the associated simulations in [Figure 3.11\(b\)](#). The maximal observed reflectance of  $(0.75 \pm 0.06)$  is obtained in this asymmetric case, at a probe detuning of 25 MHz.

Let us note that a related experiment was performed at the same time by Sorensen *et al.* [Sørensen16]. In that experiment, the lattice period, characterized by the wavelength of red-detuned trapping beams, is far away from that of the resonant probe. So instead the lattice is structured by a structuring pulse so that atoms only spaced by a distance close to the probe wavelength will be addressed. 12 % Bragg reflection from 1000 atoms has been reported in this study.

Our experimental work was based on a two-level system. We now explore the possibility of adding a classical driving field in a three-level atomic configuration. This would enable us to dynamically control transport properties of the guided light through 1D arrays.

### 3.5 Bragg Reflection from arrays of three-level emitters

In this section, we derive the transmission and reflection coefficients for the three-level case based on the approach given in [Witthaut10]. For a  $\Lambda$ -type configuration shown in Figure 3.12, with  $|g\rangle$  and  $|s\rangle$  being two hyperfine ground states and  $|e\rangle$  the excited state, the atomic Hamiltonian can be expressed within the rotating wave approximation as:

$$H_{atom}/\hbar = (\omega_0 - i\Gamma_0/2) |e\rangle \langle e| + (\omega_0 - \Delta) |s\rangle \langle s| + \frac{\Omega_c}{2} (|s\rangle \langle e| + |e\rangle \langle s|),$$

where  $|e\rangle$  is coupled to  $|s\rangle$  by a classical laser beam with Rabi frequency  $\Omega_c$  and single-photon detuning  $\Delta$ . We define the following:  $\omega_0 = \omega_e - \omega_g$ ,  $\sigma = |g\rangle \langle e|$  and  $\sigma^\dagger = |e\rangle \langle g|$  are atomic lowering and raising operators respectively,  $\sigma_s = |g\rangle \langle s|$  and  $\sigma_s^\dagger = |s\rangle \langle g|$  are operators transferring an atom from  $|s\rangle \rightarrow |g\rangle$  and  $|g\rangle \rightarrow |s\rangle$  respectively. The dispersion relation for photons can be linearized as before:  $\omega \sim v_g |\mathbf{k}|$  where  $v_g$  is the group velocity of the photons. The bosonic operator  $a_R^\dagger(x)[a_L^\dagger(x)]$  creates a right-going (left-going) photon at  $x$ ,  $V_L(V_R)$  is the coupling between the atom and the left-travelling (right-travelling) photons.

Adding the atomic part  $H_{atom}$  to the interaction part gives the full Hamiltonian:

$$\begin{aligned} \frac{H}{\hbar} = & \int dx \left( -iv_g a_R^\dagger \frac{\partial}{\partial x} a_R(x) + iv_g a_L^\dagger \frac{\partial}{\partial x} a_L(x) + V_R \delta(x) [a_R^\dagger(x) \sigma + a_R(x) \sigma^\dagger] \right. \\ & \left. + V_L \delta(x) [a_L^\dagger(x) \sigma + a_L(x) \sigma^\dagger] \right) + (\omega_0 - i\Gamma_0/2) \sigma^\dagger \sigma + (\omega_e - \Delta) \sigma_s^\dagger \sigma_s \\ & + \frac{\Omega_c}{2} (\sigma^\dagger \sigma_s + \sigma_s^\dagger \sigma). \end{aligned} \quad (3.5.1)$$

We take a similar approach as we did for the case of two-level atom in subsection 3.1.1. With the atom initially prepared in its ground state  $|g\rangle$ , a photon travelling in the waveguide may be absorbed by the atom or scattered into the left- or the right-guided mode of the waveguide or the atom can be adiabatically transferred to the hyperfine state  $|s\rangle$ . The scattering eigenstates of the Hamiltonian (3.5.1) have the form:

$$|\psi\rangle = \int dx \left[ \phi_R(x) c_R^\dagger(x) + \phi_L(x) c_L^\dagger \right] |0, g\rangle + \phi_e \sigma^\dagger |0, g\rangle + \phi_s \sigma_s^\dagger |0, g\rangle,$$

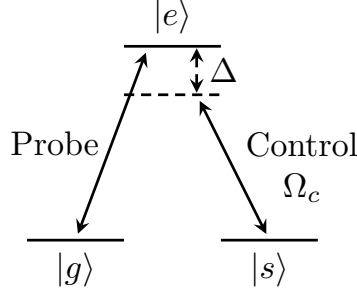


Figure 3.12 – Level diagram for a three-level  $\Lambda$ -type configuration involving a probe and a control with Rabi frequency  $\Omega_c$  and single-photon detuning  $\Delta$ . For simplicity, the hyperfine splitting is neglected.

where  $|0,g\rangle$  indicates the vacuum state and atom in ground state  $|g\rangle$ ,  $\phi_e$  and  $\phi_s$  are the probability amplitudes of the atom to be in the excited state  $|e\rangle$  and ground state  $|s\rangle$  respectively. By assuming plane waves, one can write:

$$\begin{aligned}\phi_R(x) &= te^{ikx}\theta(x) + e^{ikx}\theta(-x) \\ \phi_L(x) &= re^{-ikx}\theta(-x),\end{aligned}$$

where  $t(r)$  is the relevant transmission (reflection) amplitude and  $\theta(x)$  is a step function. As before, the eigenvalue equation is given by:

$$H|\psi\rangle = \hbar\omega|\psi\rangle.$$

We write down the terms in  $H|\psi\rangle$ .

$$H|\psi\rangle = (O_1 + O_2 + O_3 + O_4 + O_5)|0,g\rangle, \quad (3.5.2)$$

where

$$\begin{aligned}O_1 &= iv_g \int dx \frac{\partial}{\partial x} [\phi_L(x)] a_L^\dagger(x) - iv_g \int dx \frac{\partial}{\partial x} [\phi_R(x)] a_R^\dagger(x) \\ O_2 &= V_L \int dx \phi_L(x) \delta(x) a_L(x) a_L^\dagger(x) \sigma^\dagger + V_R \int dx \phi_R(x) \delta(x) a_R(x) a_R^\dagger(x) \sigma^\dagger \\ O_3 &= V_L \int dx \delta(x) \phi_e a_L^\dagger(x) + V_R \int dx \delta(x) \phi_e a_R^\dagger(x) \\ O_4 &= \phi_e (\omega_0 - i\Gamma_0/2) \sigma^\dagger + \frac{\Omega_c}{2} \phi_s \sigma^\dagger \\ O_5 &= (\omega_e - \Delta) \phi_s \sigma_s^\dagger + \frac{\Omega_c}{2} \phi_e \sigma_s^\dagger.\end{aligned}$$

Equating the coefficients of  $\sigma_s^\dagger$  on both sides of Eq. (3.5.2):

$$\begin{aligned}(\omega_0 - \Delta) \phi_s + \frac{\Omega_c}{2} \phi_e &= \omega \phi_s \\ \Rightarrow \phi_s &= \frac{\Omega_c}{2(\omega - \omega_0 + \Delta)} \phi_e.\end{aligned} \quad (3.5.3)$$

Eq. (3.1.4) to Eq. (3.1.7) in the two-level case will be the same here and we have,  $t = 1 - iV_R\phi_e/v_g$  and  $r = -iV_L\phi_e/v_g$ .

Equating the coefficients of  $\sigma^\dagger$  on both sides of Eq. (3.5.2) and using Eq. (3.1.10):

$$\begin{aligned} O_2 + \frac{\Omega_c}{2}\phi_s + (\omega_0 - i\frac{\Gamma_0}{2}) &= \omega\phi_e \\ V_R\left(\frac{1+t}{2}\right) + V_L\frac{r}{2} + \frac{\Omega_c}{2}\phi_s + (\omega_0 - i\frac{\Gamma_0}{2}) &= \omega\phi_e. \end{aligned} \quad (3.5.4)$$

Substituting Eq. (3.5.3) and expressing  $t$  and  $r$  as a function of  $\phi_e$  in Eq. (3.5.4), we can find  $\phi_e$  and hence expressions for the coefficients  $t$  and  $r$ .

**Chiral case** – With  $\Gamma_{1D}^{forw} = V_R^2/v_g$ ;  $\Gamma_{1D}^{back} = V_L^2/v_g$ , from Eq. (3.5.4) we get the expression:

$$\phi_e = \frac{V_R(\omega - \omega_0 + \Delta)}{(\omega - \omega_0 + \Delta)(\omega - \omega_0 + i\Gamma_0/2 + i\Gamma_{1D}^{forw}/2 + i\Gamma_{1D}^{back}/2) - \Omega_c^2/4}.$$

Therefore, with  $\delta = \omega - \omega_0$  the detuning from atomic resonance,

$$\left\{ \begin{aligned} r(\delta) &= \frac{-i\sqrt{\Gamma_{1D}^{forw}\Gamma_{1D}^{back}}(\delta + \Delta)}{(\delta + \Delta)(\delta + i\Gamma_0/2 + i\Gamma_{1D}^{forw}/2 + i\Gamma_{1D}^{back}/2) - \Omega_c^2/4} \\ t(\delta) &= 1 - \frac{-i\Gamma_{1D}^{forw}(\delta + \Delta)}{(\delta + \Delta)(\delta + i\Gamma_0/2 + i\Gamma_{1D}^{forw}/2 + i\Gamma_{1D}^{back}/2) - \Omega_c^2/4}. \end{aligned} \right. \quad (3.5.5)$$

Similar to the two-level case, a full microscopic treatment considering multi-level structure of atom, where atoms are distributed in all Zeeman sublevels, is essential for deriving the transmission and reflection coefficients in this three-level  $\Lambda$  configuration. Therefore, the expressions, given by Eq. (3.5.5), we have derived will have to be corrected by the full microscopic approach. Therefore, we know these expressions are only valid under approximation (no Zeeman sublevels) and do not resemble the real experimental situation.

**Symmetric case** – With  $V_R = V_L = V$  and  $\Gamma_{1D} = 2V^2/v_g$ , similarly we get the expression:

$$\phi_e = \frac{V(\omega - \omega_0 + \Delta)}{(\omega - \omega_0 + \Delta)(\omega - \omega_0 + i\Gamma_0/2 + i\Gamma_{1D}/2) - \Omega_c^2/4}$$

Therefore, with  $\delta = \omega - \omega_0$  the detuning from atomic resonance,

$$\left\{ \begin{aligned} t(\delta) &= \frac{(\delta + \Delta)(\delta + i\Gamma_0/2) - \Omega_c^2/4}{(\delta + \Delta)(\delta + i\Gamma_0/2 + i\Gamma_{1D}/2) - \Omega_c^2/4} \\ r(\delta) &= \frac{-(i/2)\Gamma_{1D}/\Gamma_0(\delta + \Delta)}{(\delta + \Delta)(\delta + i\Gamma_0/2 + i\Gamma_{1D}/2) - \Omega_c^2/4}. \end{aligned} \right. \quad (3.5.6)$$

Similar to the two-level case, the expressions for coefficients in case of symmetric coupling, given by Eq. (3.5.6), applies to a real experimental situation. The control field can be shined from outside into the atomic array or coupled into the nanofiber along with the probe. We can now study the Bragg reflection spectrum for three-level  $\Lambda$  configuration using realistic parameters.

### 3.5.1 Controllable Bragg mirror and optical switching

We follow the transfer matrix formalism, similar to subsection 3.1.2, to simulate the reflectance for the full atomic chain of 2000 atoms. Figure 3.13(a) gives the Bragg reflection spectrum for different wavelength detunings  $\Delta\lambda$  under EIT condition i.e. single-photon detuning  $\Delta = 0$ . The control field Rabi frequency of  $\Omega_c/\Gamma_0 = 1$  and the Purcell factor  $\Gamma_{1D}/\Gamma_0 = 0.01$  are used in the plot. We see a narrow transparency window on the order of hundreds of kilohertz depending on the control beam intensity for the perfectly commensurate array  $\Delta\lambda = 0$ . For the same parameters, in the case of close-to-commensurate arrays  $\Delta\lambda = 0.1, 0.2$  nm, the transparency window is relatively widened in an asymmetric way i.e., there is an additional dip along with the zero-detuning ( $\delta = 0$ ) dip. The additional dip occurs within 1 MHz towards the blue-detuned side.

We are interested in finding a transparency window for close-to-commensurate arrays at the detuning  $\delta$  where the reflectance without control field is maximum. From Figure 3.9, we see that the simulated Bragg reflection peak occurs at  $\sim 15$  MHz for  $\Delta\lambda = 0.2$  nm. In order to create a transparency window at around this detuning we can play with the single-photon detuning  $\Delta$ . Putting  $\Delta/\Gamma_0 = -3$  i.e. the control field blue-detuned with respect to the resonance by 15.5 MHz we see a transparency dip when there is a Bragg reflection peak (without control), as shown in Figure 3.13(b). The curve in blue is Bragg reflection spectrum without a control field i.e. the result in two-level case is recovered. The curves in green, red are with control Rabi frequency  $\Omega_c/\Gamma_0 = 1, 2$  respectively. The transparency window can be made narrower by reducing control field intensity as usual.

Thus, a blue-detuned Raman transition with single-photon detuning on the order of tens of MHz can create a situation where the Bragg reflection from the atomic arrays can be drastically changed by adding/removing the control field. This is effectively a controllable Bragg mirror since the probe can be reflected by the ‘atomic mirrors’ or transmitted when the ‘atomic mirrors’ are made transparent by shining a control field. If the control field is sent into the nanofiber, then the required Rabi frequency for opening a transparency window could possibly be achieved by few tens of photons. In that case, a control field pulse at few-photon level can be used to reflect or transmit a weak probe pulse at a few photon level. It will enable us to realize a ‘switch’ at few-photon level, with the control field providing ‘button’ of the switch. Thus, implementing such a scheme will be a step towards experiments in quantum non-linear optics (QNLO). We have plans in our group for experimental implementation in future.

In conclusion, we have realized an efficient Bragg atomic mirror based on a nanoscale one-dimensional waveguide coupled to about 2000 atoms. The effect of the chiral character of the waveguide on the reflection features has also been observed. Bragg scattering can also be used as a tool for optical lattice analysis like characterization of temperature, positional spread of atoms, etc. In addition, these observations demonstrate key ingredients for the exploration of a variety of emerging and potentially rich protocols based on 1D reservoirs coupled to atoms. To enable an exact commensurate array of trapped atoms, and therefore an enhanced reflection closer to resonance, a bichromatic optical superlattice, whose trap periodicity is given by the tunable beat frequency of the trapping lasers [Gorlitz01, Campos03], can be developed. Such a

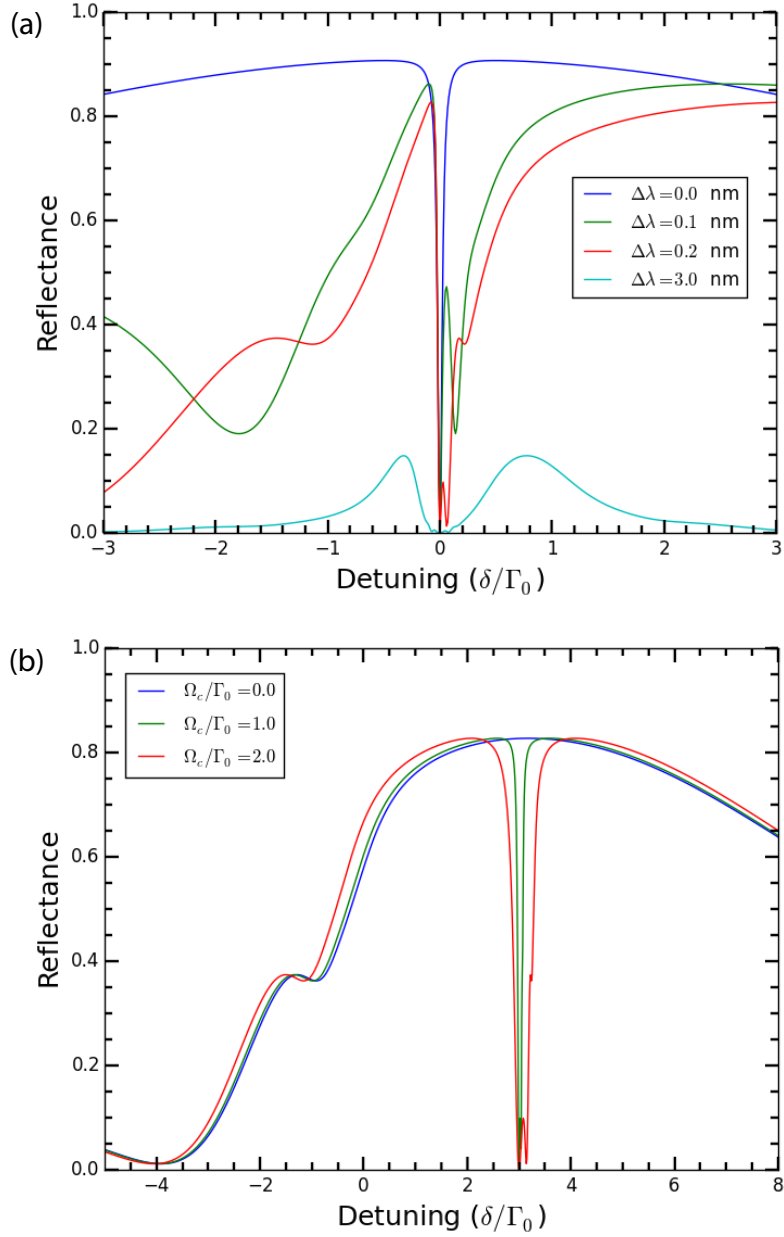


Figure 3.13 – Bragg reflection in three-level atom. (a) Spectrum for different wavelength detunings  $\Delta\lambda = 0, 0.1, 0.2, 3$  nm under EIT condition i.e. single-photon detuning  $\Delta = 0$ . The control Rabi frequency is set to  $\Omega_c/\Gamma_0 = 1$  and the coupling to  $\Gamma_{1D}/\Gamma_0 = 0.01$ . Transparency window is seen at resonance or very close to resonance (b) Spectrum for close-to-commensurate trap  $\Delta\lambda = 0.2$  nm with varying control Rabi frequencies  $\Omega_c/\Gamma_0 = 0, 1, 2$ . The single-photon detuning is set to  $\Delta/\Gamma_0 = -3$  (i.e. 15.5 MHz blue-detuned) and the coupling to  $\Gamma_{1D}/\Gamma_0 = 0.01$ . Transparency window and Bragg reflection peak (without control) occurs at around 15 MHz.

trapping scheme, which has been demonstrated in free space, would need to be adapted to the evanescent field configuration around a nanofiber. This superlattice could also include a double primitive cell enabling a richer photonics spectrum [Rist09]. In addition, a classical driving field in a three-level atomic configuration would enable us to dynamically control transport properties by realizing a controllable Bragg mirror - a novel scheme for quantum non-linear optics at few-photon level.

### Chapter Conclusion

To summarize the chapter in few main points:

- The theoretical aspects of Bragg reflection from close-to-commensurate 1D atomic arrays coupled to a nanoscale waveguide are explained. The derivation for single-atom reflection and transmission coefficients is provided and a simple model, involving transfer matrix formalism, for spectra simulation of atomic arrays is introduced.
- The effect of several experimental parameters or trap mechanisms on the Bragg reflection has been studied. The simulation of the trapping potential is provided.
- The experimental setup and results of Bragg reflection are described. The experimental plots appear in agreement with the simulated spectra.
- The reflection spectra is dependent on the orientation of probe polarization relative to the atomic chains. This effect, called chirality, has been observed in our experiment for this particular application.
- Our model has been extended to three-level  $\Lambda$ -type atomic configuration. The single-atom transmission and reflection coefficients are derived. For close-to-commensurate arrays, a Raman transition blue-detuned by tens of MHz can open a transparency window at the same detuning where the Bragg reflection peak, without control field, occurs. This can help us realize a controllable Bragg mirror enabling switching of optical pulses at few-photon level - a step towards quantum non-linear optics.

# Conclusion

In this thesis, we have presented a nanofiber-based platform for light-matter interaction mediated by a 1D waveguide. An ensemble of atoms are trapped in two parallel 1D arrays on each side of a nanofiber. This system lets us reach high optical depth ( $OD \sim 100$ ) and long lifetimes ( $\sim 25$  ms) with few thousand atoms. In this platform, we have demonstrated an efficient Bragg atomic mirror which reflects 75 % of the input light when the lattice period is made close-to-commensurate with the resonant wavelength. In addition, we observed chiral effect - the dependency of orientation of probe polarization relative to the atomic arrays, on the reflection spectrum. This opens the door for further exploration of collective and cooperative effects.

For further applications, we now need to improve the characteristics of our trap. The length of the MOT cloud now is  $\sim 3$  mm, which is smaller than  $\sim 1$  cm waist of the nanofiber. We plan to at least double the size of MOT beams by replacing the 1 inch collimators with 2 inch collimators. Also, the power would be increased in each of the MOT trapping and repump beams. This would enable us to get a larger, elongated cloud and in turn more number of atoms could be trapped in 1D arrays. It would lead to a significant increase in the optical depth of the ensemble. In addition, by exploring light-assisted collisions in our trap, the loading process could be made more efficient i.e. a higher filling factor could be targeted. For example, a blue-detuned beam with a chosen small detuning can be used to reach this high loading efficiencies [Grunzweig10, Lester15].

An ongoing work in our lab is to pump atoms to a given Zeeman sublevel. Such optical pumping has been studied, in a similar setting as ours, in [Mitsch14a, Albrecht16]. Once achieved, it will eliminate the effects of inhomogeneous broadening resulting from residual and ‘fictitious’ magnetic fields, the latter arising due to the remaining light-shifts in the trap. Hence, it will allow long coherence times in the system ideal for implementation of quantum memory and quantum information protocols. In this case, the developed nanofiber platform is a promising system to combine high efficiency and long lifetime that has been demonstrated so far in different systems. The other goal is to cool the trapped atoms to their motional ground state. Cooling an atom to its motional ground state has been demonstrated for optical tweezers in [Kaufman12]. Recently, cooling of nanofiber-trapped atoms by Raman sideband cooling has been reported in [Østfeldt17]. An atom cooled to its ground state will be more localized at the bottom of the potential wells that can potentially minimize the dephasing of a collective state. This can prolong the trap lifetime. The lifetime of the trap, on the other hand, could also be improved by reducing the fluctuations in power and polarization of the dipole beams. To reduce intensity fluctuations, the power of the laser beams for

dipole trap could be locked.

Alongside implementation of improved storage and generation of collective excitation in the atomic ensemble, the focus in our group is also to implement a controllable Bragg atomic mirror, as proposed in [chapter 3](#). This will enable to push the nonlinearities down to a few-photon level. Some recent interesting developments have been the study of chiral light-matter interaction and quantum many-body physics based on this platform. The many-body effects arise because of interaction, termed as long-range interactions, between distant atoms via the waveguide. The interference of light scattered by the atoms coupled to the waveguide can lead to phase transition of the atomic spatial order depending on the intensity of an external pump field. This is an evidence of self-organization studied theoretically in [[Chang13](#)] and yet to be explored experimentally.

The emerging field of hybrid quantum systems, reviewed in [[Xiang13](#), [Kurizki15](#)], combine various available platforms - atomic, Rydberg, ionic, photonic, superconducting circuits and solid state - for making use of the best available interaction strength and coherence properties in each of them for computing tasks, like processing, storage and reversible mapping of quantum information. Waveguide QED systems, like our trapped atoms close to a nanofiber can be a promising tool towards realization of such future quantum hybrid technologies.

# Appendix A

## Python interface for fiber-pulling

We present the screenshots of the python interface used for flame-width measurement and fiber-pulling. They have been developed by Maxime Joos.

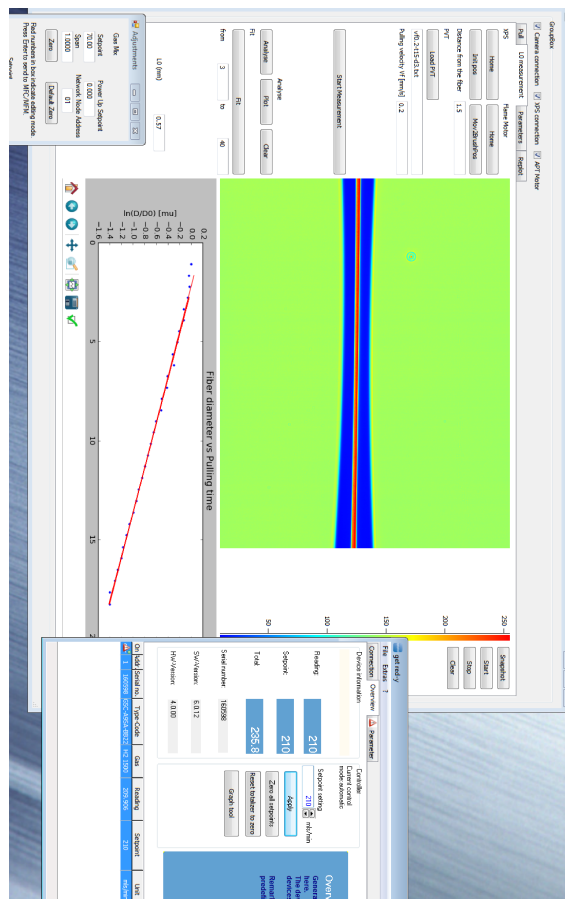


Figure A.1 – Flame-width measurement interface and two other interfaces (small) for flowmeters. The stages are moved apart with constant velocity and exponential thinning of fibers is captured in camera as a function of time. This helps to extract the flame-width  $L_0$ .

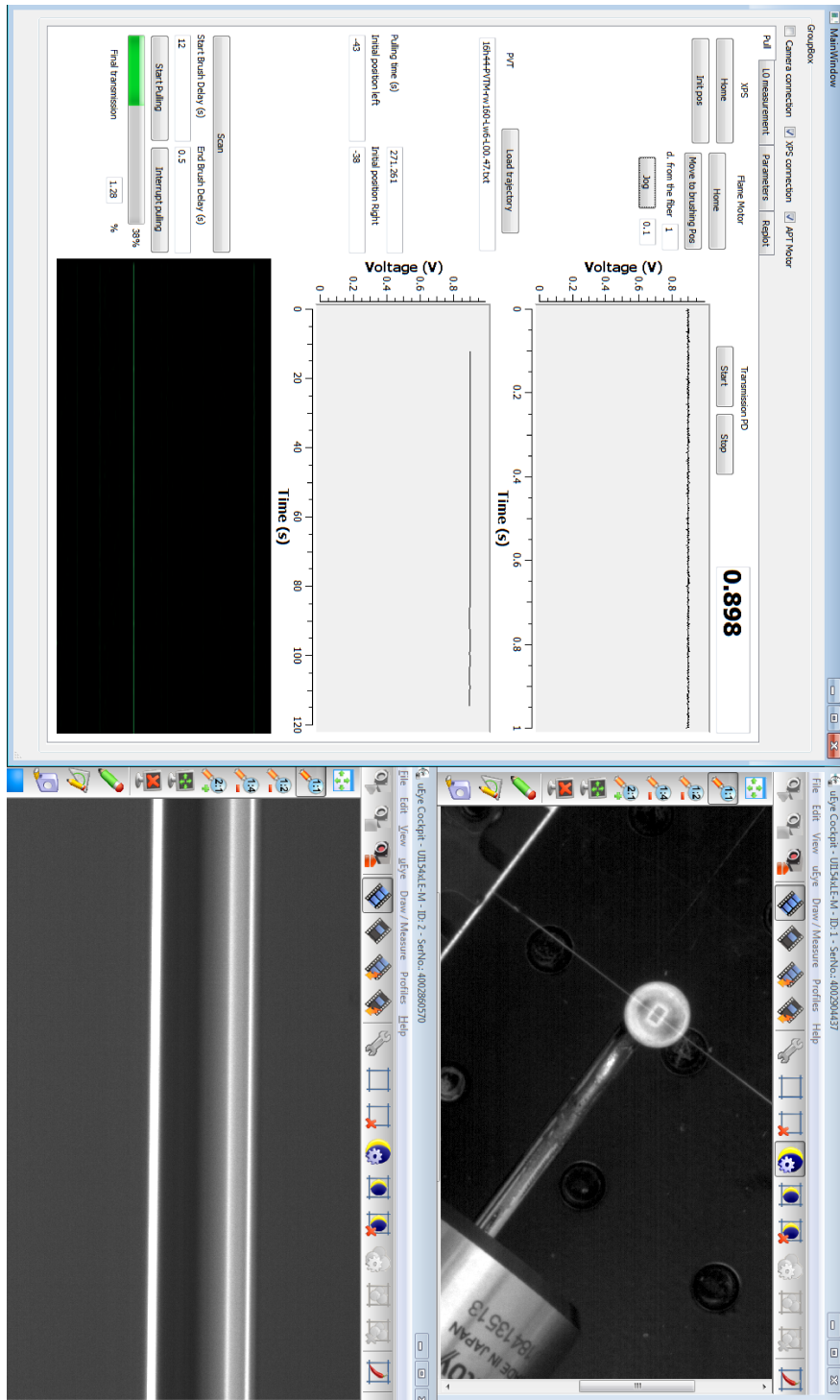


Figure A.2 – Fiber-pulling interface along and images of the fiber as seen from the two cameras during a fiber-pull. The fiber transmission, images and FFT spectra of taper are updated in real time.

# Appendix B

## Electron Microscopy

It is crucial for our experiment to have a precise knowledge of the nanofiber diameter. We fabricate a set of nanofibers with pre-defined pulling parameters. Then, measuring the samples by scanning electron microscope (SEM), we get an idea of the nanofiber diameter with statistical variations. The process could be repeated with another set of pulling parameters.

### Sample preparation

The nanofibers were glued and well tightened side by side on a piece of steel which is directly mounted on a specific specimen holder, see [Figure B.1](#), suited for microscopy. In order to observe the nanofibers, a thin conductive layer (few nm) is needed, preventing charging effects, reducing thermal damage and also improving the secondary electron signal (better signal/noise ratio). The nanofibers were coated using the high vacuum coater system from Leica, EMSCD 500 at IMPMC. Initially, we've tried carbon coating but few nanofibers inflated and then broke under beam irradiation. To avoid this artefact, we choose platinum. For platinum deposition, a sputtering technique was used. The sample to be coated is placed in a the vacuum chamber containing an inert gas - here argon - and a negative charge is applied to a target source material – here platinum - that will be deposited onto the substrate causing the plasma to glow. By applying an electrical field into the chamber, Ar atoms become positively charged ions attracted to the negatively charged target material at a very high velocity that “Sputters off” atomic size particles from the target platinum source. These particles cross the vacuum deposition chamber of the sputter coater and are deposited as a thin film of material on the surface of the substrate to be coated. From our experience, a coating of 10 nm thickness works pretty well. The parameters are: For thickness - 10 nm of Pt, Current - 60 mA and Timer value - 30s.

### SEM Observations

Scanning electron microscopy observations are performed at IMPMC using a Zeiss Ultra 55 SEM (CarlZeiss AG, Oberkochen, Germany) equipped with a field emission gun (Gemini column). The resolution of a SEM is about 10 nm. Images are acquired with the microscope operating at 3 or 1 kV, and a working distance of  $\sim 4$  mm in



Figure B.1 – Nanofibers glued on steel on a specimen (SEM) holder.

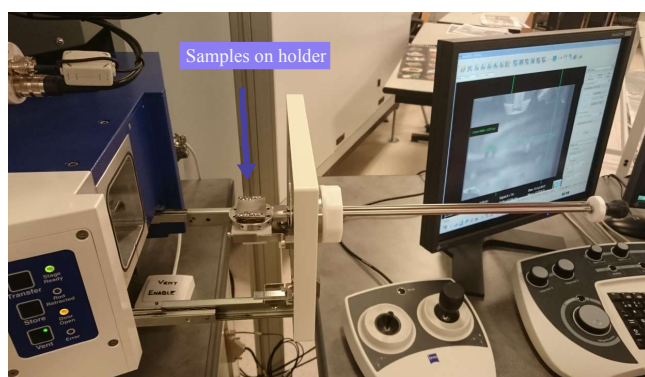


Figure B.2 – Vacuum airlock introducing system to transfer holders into the SEM chamber.

secondary electron mode using the SE2 detector or InLens detector. The aperture is chosen to be 20 or 30  $\mu\text{m}$ .

The first step is to identify the regions on the sample where the fibers are glued. We start by locating the mounds of glue at one of the edges of the specimen holder. Once a fiber is located, its coordinates are saved. Then, we traverse along the length of the fiber and make measurements when we are on its waist or close to its waist. Note, when are zoomed in on a fiber, we must be careful not to stay at a particular position for too long with the SEM process in running mode. This is because the electron beam impinging on the fiber can burn and even break it at that point.

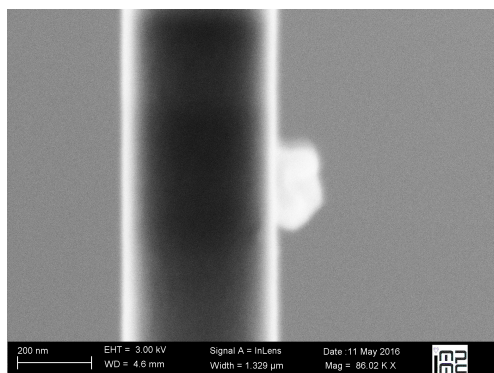
For getting clear, sharp and focussed images, we have to adjust the focus along with the following:

- The gun alignment is checked and centered. The noise reduction is enabled.
- The wobble, for alignment of the electron beam with the optical imaging system, is adjusted by fine-tuning aperture X and aperture Y to remove the oscillations in two perpendicular directions on the plane of the sample.
- At the position of measurement, to correct for astigmatism, stigmators X, Y are adjusted to get a sharp, focussed image.

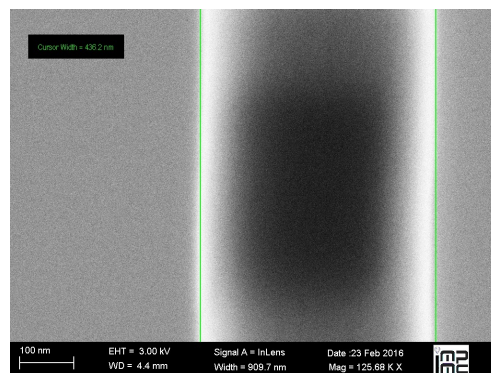
We perform line averaging over few traces (between 6 and 10). Finally, the scanning speed is reduced to minimum for the best possible image. Measurements were per-

formed by imaging the fibers vertically without any beam rotation of the scan. It should be noted that the SEM is not a proper tool for metrology.

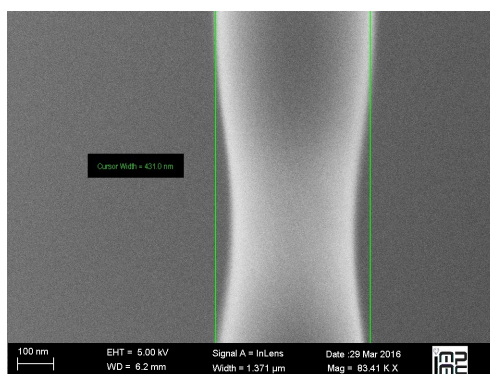
Now, I present some SEM images of nanofibers measured with the protocol above. One can see dust of sub-micron dimensions stuck on the nanofiber in [Figure B.3a](#). In other cases, the electron beam has either burnt ([Figure B.3b](#)) or reduced ([Figure B.3c](#)) the diameter of fiber during the measurement.



(a) A dust particle stuck on the nanofiber surface.



(b) The burnt region on the nanofiber is formed by overexposure of the electron beam. This can happen if we measure at a particular position for too long.



(c) The diameter has been reduced by the electron beam leading to this curved shape. This can happen if the metallization is not done at all or done inadequately prior to electron microscopy.

Figure B.3 – Images from SEM.



# Appendix C

## Electronics for fast current reversal

The electronic circuit, presented here, allows fast reversal of current in coils. A pair of coils are placed on either side of our chamber with the axis of the coils coinciding with the longitudinal axis of the fiber. The coils are in anti-Helmholtz configuration. The typical values in our configuration are: distance between the coils  $\sim 34$  cm, radius of the coils  $\sim 12$  cm, number of turns = 15, current through the coils  $\sim 2$  A. This produces a magnetic field gradient of about 70 mG/cm at the nanofiber waist where the atoms are interfaced. The goal is to flip the gradient from 70 mG/cm to -70 mG/cm as fast as possible. This is done by reversing the current from about 2A to -2A using a power opamp (PA107 from Apex Microtechnology) set up as voltage-to-current converter, see [Figure C.1](#). Suitable values of the passive components - capacitors, inductors and resistors have to be chosen to provide an optimal feedback and hence a stable output. The evaluation kit EK16 (from Apex Microtechnology) provides a platform for the opamp PA107 and the various circuit components, some of which are pre-wired in the board.

An input square pulse  $V_{in}$  (from 1.5 V to -1.5 V) swings the output voltage of the opamp from +92 V to -92 V, which is the maximum voltage swing allowed by  $\pm V_s = \pm 100$  V. Because of the high inductive load, the current reverses from 1.8A to -1.8A in about 140  $\mu$ s, as shown in [Figure C.2](#). The reversal time is limited by the large inductance  $L \sim 410$   $\mu$ H of our coils. The inductance of coils, fixed by design, is given by its radius and number of turns.

We have to be careful not to overstress the opamp. This is because, changing the current rapidly in an inductor comes at an expense of a lot of energy. The heat produced is dissipated by using silicon thermal paste and heat sink radiators. In order to prevent the output voltage of opamp from overshooting the  $\pm 100$  V limit, we have used fast recovery diodes  $D1$  and  $D1$  (recovery time  $\sim 50$  ns) for protection of the opamp. Another important point is: the input square pulse has to be used with a small duty cycle i.e. only for around  $1/50^{\text{th}}$  of a cycle there should be input pulses (1.5 V to -1.5 V) during which the opamp drives high current but for the rest of the cycle zero input ensures the opamp does no work. This allows to keep the power dissipation below the maximum power rating of the opamp.

An alternative circuit design that is expected to reduce the reversal time by a factor of 2 or 3 is shown in [Figure C.3](#). However, this has not been implemented, since from simulation, we see that the output voltage briefly overshoots the maximum allowed

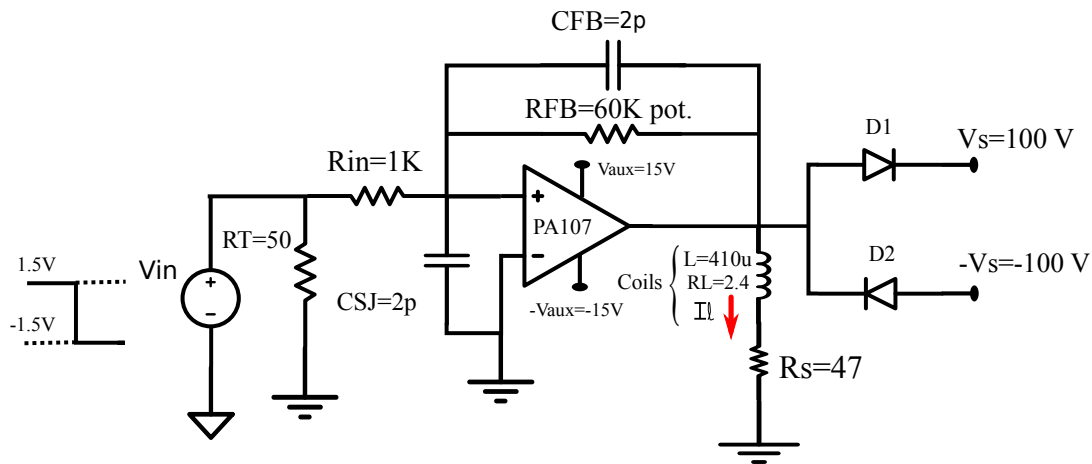


Figure C.1 – The circuit for fast current reversal in an inductive load given by  $L \sim 410 \mu\text{H}$ . The opamp is set up as a voltage-to-current converter. The input voltage, feedback impedances ( $R_{\text{FB}}$ ,  $C_{\text{FB}}$ ) and coupling junction capacitance ( $C_{\text{SJ}}$ ) are chosen optimally to reverse the current in the coils. All impedances are in SI units - ohm, farad, henry.

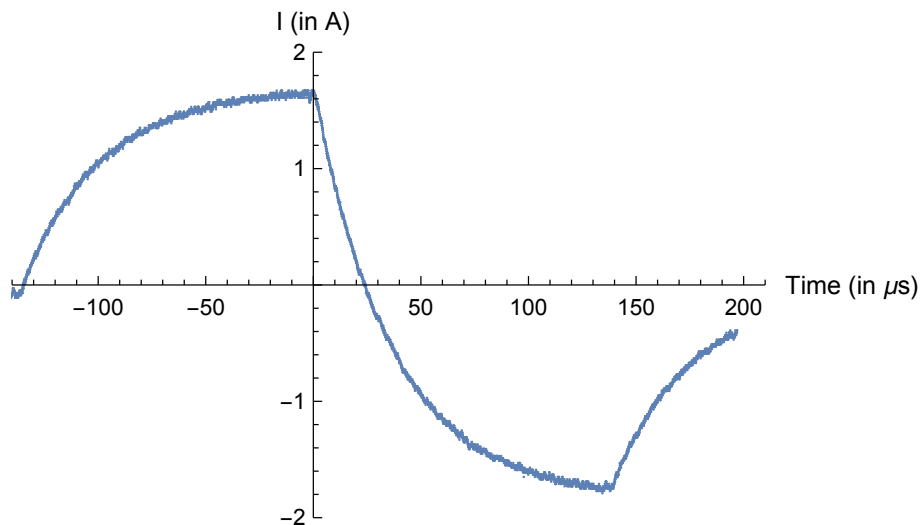


Figure C.2 – Measured current in the coils as a function of time. At time  $t = 0$ , a reversal in current is triggered by input pulse  $V_{\text{in}}$  to the opamp. The reversal is achieved in about  $140 \mu\text{s}$ .

voltage  $\pm 100 \text{ V}$  during the reversal time. Even though we have protection diodes, there may be a potential chance of breaking the opamp if such a circuit is used continuously. It could be carefully tested in future with more expert knowledge, for short times intervals and then for longer times.

We list the turning on/off sequence for the electronics used here. This is crucial for protection of this device, which involves a sensitive and expensive opamp.

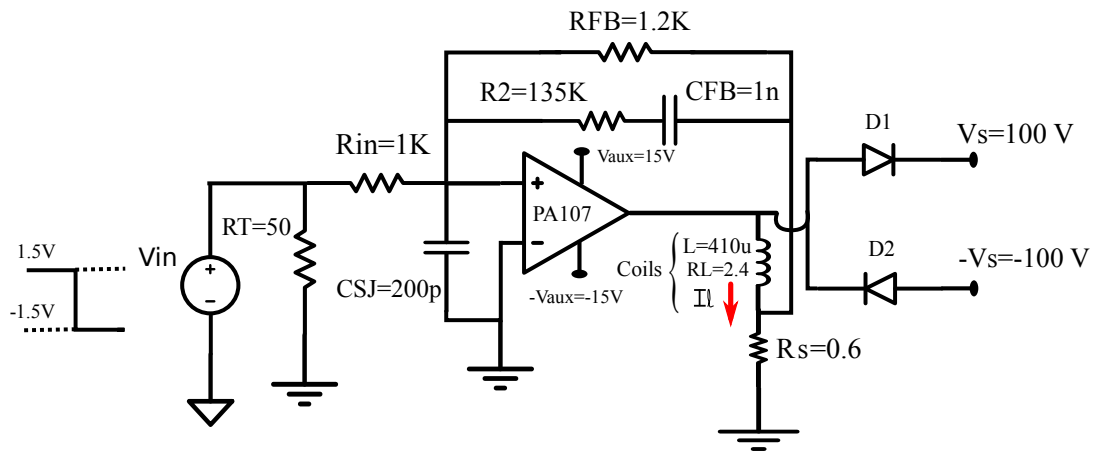


Figure C.3 – The alternative circuit, which is expected to reverse current faster than Figure C.1. The feedback loop in this case is connected to the output path after the current coils. However, output voltage could overshoot the maximum allowed voltage  $\pm 100$  V during the time reversal that might damage the opamp. All impedances are in SI units - ohm, farad, henry.

Turning on:

- Make sure there is load at OUT of the opamp.
- $\pm 15$  V supply for  $\pm V_{aux}$ .
- $\pm 100$  V supply for  $\pm V_s$ .
- Input pulse  $V_{in}$  to the opamp.

Turning off:

- Input pulse  $V_{in}$  to the opamp.
- $\pm 100$  V supply for  $\pm V_s$ .
- $\pm 15$  V supply for  $\pm V_{aux}$ .



# Bibliography

- [Acín07] A. Acín, J. I. Cirac, and M. Lewenstein. Entanglement percolation in quantum networks. *Nature Physics*, 3(4):256–259, 2007. 0612167, URL <http://dx.doi.org/10.1038/nphys549>. (cited in p. 2)
- [Akimov07] A. V. Akimov, A. Mukherjee, C. L. Yu, D. E. Chang, A. S. Zibrov, P. R. Hemmer, H. Park, and M. D. Lukin. Generation of single optical plasmons in metallic nanowires coupled to quantum dots. *Nature*, 450(7168):402–406, 2007. arXiv:0706.4335v1, URL <http://dx.doi.org/10.1038/nature06230>. (cited in p. 5)
- [Albrecht15] B. Albrecht, P. Farrera, G. Heinze, M. Cristiani, and H. de Riedmatten. Controlled Rephasing of Single Collective Spin Excitations in a Cold Atomic Quantum Memory. *Phys. Rev. Lett.*, 115:160501, Oct 2015. URL <http://dx.doi.org/10.1103/PhysRevLett.115.160501>. (cited in p. 67)
- [Albrecht16] B. Albrecht, Y. Meng, C. Clausen, A. Dureau, P. Schneeweiss, and A. Rauschenbeutel. Fictitious magnetic-field gradients in optical microtraps as an experimental tool for interrogating and manipulating cold atoms. *Physical Review A*, 94(6), 2016. 1608.02517, URL <http://dx.doi.org/10.1103/PhysRevA.94.061401>. (cited in p. 91)
- [Aoki06] T. Aoki, B. Dayan, E. Wilcut, W. P. Bowen, A. S. Parkins, T. J. Kippenberg, K. J. Vahala, and H. J. Kimble. Observation of strong coupling between one atom and a monolithic microresonator. *Nature*, 443(7112):671–674, October 2006. URL <http://dx.doi.org/10.1038/nature05147>. (cited in p. 4)
- [Arcari14] M. Arcari, I. Söllner, A. Javadi, S. Lindskov Hansen, S. Mahmoodian, J. Liu, H. Thyrrerstrup, E. H. Lee, J. D. Song, S. Stobbe, and P. Lodahl. Near-Unity Coupling Efficiency of a Quantum Emitter to a Photonic Crystal Waveguide. *Phys. Rev.*

- Lett.*, 113:093603, Aug 2014. URL <http://dx.doi.org/10.1103/PhysRevLett.113.093603>. (cited in p. 5)
- [Ashcroft76] N. Ashcroft and N. Mermin. *Solid State Physics*. Saunders College, Philadelphia, 1976. (cited in p. 80)
- [Babinec10] T. M. Babinec, B. J. M. Hausmann, M. Khan, Y. Zhang, J. R. Maze, P. R. Hemmer, and M. Lončar. A diamond nanowire single-photon source. *Nature Nanotechnology*, 5(3):195–199, 2010. 0908.0233, URL <http://dx.doi.org/10.1038/nnano.2010.6>. (cited in p. 5)
- [Bajcsy09] M. Bajcsy, S. Hofferberth, V. Balic, T. Peyronel, M. Hafezi, A. S. Zibrov, V. Vuletic, and M. D. Lukin. Efficient all-optical switching using slow light within a hollow fiber. *Physical Review Letters*, 102(20), 2009. arXiv:0901.0336v1, URL <http://dx.doi.org/10.1103/PhysRevLett.102.203902>. (cited in p. 5)
- [Balykin04] V. I. Balykin, K. Hakuta, F. Le Kien, J. Q. Liang, and M. Morinaga. Atom trapping and guiding with a subwavelength-diameter optical fiber. *Physical Review A*, 70(1):011401, July 2004. URL <http://dx.doi.org/10.1103/PhysRevA.70.011401>. (cited in p. 7)
- [Béguin14] J.-B. Béguin, E. M. Bookjans, S. L. Christensen, H. L. Sørensen, J. H. Müller, E. S. Polzik, and J. Appel. Generation and Detection of a Sub-Poissonian Atom Number Distribution in a One-Dimensional Optical Lattice. *Phys. Rev. Lett.*, 113:263603, Dec 2014. URL <http://dx.doi.org/10.1103/PhysRevLett.113.263603>. (cited in p. 7)
- [Béguin17] J. B. Béguin, J. H. Müller, J. Appel, and E. S. Polzik. Observation of quantum spin noise in a 1D light-atoms quantum interface. pages 1–6, 2017. 1708.08387, URL <http://arxiv.org/abs/1708.08387>. (cited in p. 7)
- [Bilodeau88] F. Bilodeau, K. O. Hill, S. Faucher, and D. C. Johnson. Low-loss highly overcoupled fused couplers: Fabrication and sensitivity to external pressure. *Journal of Lightwave Technology*, 6(10):1476–1482, 1988. URL <http://dx.doi.org/10.1109/50.7904>. (cited in p. 23)
- [Birk195] G. Birkel, G. M., Deutsch, I.H., R. S.L., and P. W.D. Bragg Scattering from Atoms in Optical Lattices. *Phys. Rev. Lett.*, 75:2823, 1995. URL <http://journals.aps.org/prl/abstract/10.1103/PhysRevLett.75.2823>. (cited in p. 69)

- [Birks92] T. A. Birks and Y. W. Li. The Shape of Fiber Tapers. *Journal of Lightwave Technology*, 10:4, April 1992. (cited in p. 21)
- [Black91] R. Black, S. Lacroix, F. Gonthier, W. Henry, W. Stewart, and J. Love. Tapered single-mode fibres and devices. *IEEE Proceedings*, 138:5, October 1991. (cited in p. 20)
- [Bliokh14] K. Y. Bliokh, A. Y. Bekshaev, and F. Nori. Extraordinary momentum and spin in evanescent waves. 5:3300, March 2014. URL <http://dx.doi.org/10.1038/ncomms4300>. (cited in p. 16)
- [Boone15] K. Boone, J. P. Bourgoïn, E. Meyer-Scott, K. Heshami, T. Jennewein, and C. Simon. Entanglement over global distances via quantum repeaters with satellite links. *Physical Review A - Atomic, Molecular, and Optical Physics*, 91(5), 2015. 1410.5384, URL <http://dx.doi.org/10.1103/PhysRevA.91.052325>. (cited in p. 1)
- [Brambilla04] G. Brambilla, V. Finazzi, and D. Richardson. Ultra-low-loss optical fiber nanotapers. *Opt. Express*, 12(10):2258–2263, May 2004. URL <http://dx.doi.org/10.1364/OPEX.12.002258>. (cited in p. 9)
- [Briegel98] H.-J. Briegel, W. Dür, J. I. Cirac, and P. Zoller. Quantum Repeaters: The Role of Imperfect Local Operations in Quantum Communication. *Physical Review Letters*, 81(26):5932–5935, 1998. 9803056v1, URL <http://dx.doi.org/10.1103/PhysRevLett.81.5932>. (cited in p. 2)
- [Camposeo03] A. Camposeo, M. Anderlini, D. Ciampini, J. H. Müller, D. Wilkowski, E. Arimondo, and H. Ritsch. One-dimensional bichromatic standing-wave cooling of cesium atoms. *Journal of Optics B: Quantum and Semiclassical Optics*, 5(2):S29, 2003. URL <http://dx.doi.org/10.1088/1464-4266/5/2/355>. (cited in p. 88)
- [Chang13] D. E. Chang, J. I. Cirac, and H. J. Kimble. Self-organization of atoms along a nanophotonic waveguide. *Physical Review Letters*, 110(11), 2013. 1211.5660, URL <http://dx.doi.org/10.1103/PhysRevLett.110.113606>. (cited in p. 92)
- [Chang14] D. E. Chang, V. Vuletic, and M. D. Lukin. Quantum nonlinear optics - photon by photon. *Nat Photon*, 8(9):685–694, September 2014. URL <http://dx.doi.org/10.1038/nphoton.2014.192>. (cited in p. 2)

- [Choi08] K. S. Choi, H. Deng, J. Laurat, and H. J. Kimble. Mapping photonic entanglement into and out of a quantum memory. *Nature*, 452(7183):67–71, March 2008. URL <http://dx.doi.org/10.1038/nature06670>. (cited in p. 4)
- [Chou04] C. W. Chou, S. V. Polyakov, A. Kuzmich, and H. J. Kimble. Single-Photon Generation from Stored Excitation in an Atomic Ensemble. *Phys. Rev. Lett.*, 92:213601, May 2004. URL <http://dx.doi.org/10.1103/PhysRevLett.92.213601>. (cited in p. 4)
- [Claudon10] J. Claudon, J. Bleuse, N. S. Malik, M. Bazin, P. Jaffrennou, N. Gregersen, C. Sauvan, P. Lalanne, and J.-M. Gérard. A highly efficient single-photon source based on a quantum dot in a photonic nanowire. *Nature Photonics*, 2010. URL <http://dx.doi.org/10.1038/nphoton.2009.287>. (cited in p. 5)
- [Corzo16] N. V. Corzo, B. Gouraud, A. Chandra, A. Goban, A. S. Sheremet, D. V. Kupriyanov, and J. Laurat. Large Bragg Reflection from One-Dimensional Chains of Trapped Atoms Near a Nanoscale Waveguide. *Physical Review Letters*, 117(13):4–7, 2016. 1604.03129, URL <http://dx.doi.org/10.1103/PhysRevLett.117.133603>. (cited in p. 7, 32, and 69)
- [Dalibard85] J. Dalibard and C. Cohen-Tannoudji. Dressed-atom approach to atomic motion in laser light: the dipole force revisited. *J. Opt. Soc. Am. B*, 2(11):1707–1720, Nov 1985. URL <http://dx.doi.org/10.1364/JOSAB.2.001707>. (cited in p. 43)
- [Darquié05] B. Darquié. *Manipulation of Atoms in Microscopic Dipole Traps and Controlled Emission of Photons by a Single Atom*. Theses, Université Paris Sud - Paris XI, November 2005. URL <https://pastel.archives-ouvertes.fr/tel-00011604>. (cited in p. 3)
- [Dayan08] B. Dayan, A. S. Parkins, T. Aoki, E. P. Ostby, K. J. Vahala, and H. J. Kimble. A Photon Turnstile Dynamically Regulated by One Atom. *Science*, 319(5866):1062–1065, 2008. URL <http://dx.doi.org/10.1126/science.1152261>. (cited in p. 4)
- [Deutsch95] I. Deutsch, R. J. C. Spreeuw, S. Rolston, and W. Phillips. Photonic band gaps in optical lattices. *Phys. Rev. A*, 52:1394, 1995. URL <http://journals.aps.org/pr/abstract/10.1103/PhysRevA.52.1394>. (cited in p. 74 and 80)

- [Deutsch98] I. H. Deutsch and P. S. Jessen. Quantum-state control in optical lattices. *Physical Review A*, 57(3):1972–1986, 1998. 9801023, URL <http://dx.doi.org/10.1103/PhysRevA.57.1972>. (cited in p. 44)
- [Dicke54] R. H. Dicke. Coherence in Spontaneous Radiation Processes. *Phys. Rev.*, 93:99–110, Jan 1954. URL <http://dx.doi.org/10.1103/PhysRev.93.99>. (cited in p. 71)
- [Ding12] D. Ding, A. Goban, K. S. Choi, and H. J. Kimble. Corrections to our results for optical nanofiber traps in Cesium. *ArXiv e-prints*, December 2012. 1212.4941. (cited in p. 45 and 46)
- [Duan01] L.-M. Duan, M. D. Lukin, J. I. Cirac, and P. Zoller. Long-distance quantum communication with atomic ensembles and linear optics. *Nature*, 414(6862):413–418, November 2001. URL <http://dx.doi.org/10.1038/35106500>. (cited in p. 4)
- [Englund10] D. Englund, B. Shields, K. Rivoire, F. Hatami, J. Vučković, H. Park, and M. D. Lukin. Deterministic coupling of a single nitrogen vacancy center to a photonic crystal cavity. *Nano Letters*, 10(10):3922–3926, 2010. 1005.2204, URL <http://dx.doi.org/10.1021/nl101662v>. (cited in p. 4)
- [Fatemi17] F. K. Fatemi, J. E. Hoffman, P. Solano, E. F. Fenton, G. Beadie, S. L. Rolston, and L. A. Orozco. Modal interference in optical nanofibers for sub-Angstrom radius sensitivity. 4(1), 2017. URL <http://dx.doi.org/10.1364/OPTICA.4.000157>. (cited in p. 18)
- [Fleischhauer05] M. Fleischhauer, A. Imamoglu, and J. P. Marangos. Electromagnetically induced transparency: Optics in coherent media. *Rev. Mod. Phys.*, 77:633–673, Jul 2005. URL <http://dx.doi.org/10.1103/RevModPhys.77.633>. (cited in p. 4)
- [Geremia06] J. M. Geremia, J. K. Stockton, and H. Mabuchi. Tensor polarizability and dispersive quantum measurement of multilevel atoms. *Physical Review A - Atomic, Molecular, and Optical Physics*, 73(4), 2006. 0501033, URL <http://dx.doi.org/10.1103/PhysRevA.73.042112>. (cited in p. 43)
- [Goban12] A. Goban, K. S. Choi, D. J. Alton, D. Ding, C. Lacroûte, M. Pototschnig, T. Thiele, N. P. Stern, and H. J. Kimble. Demonstration of a State-Insensitive, Compensated Nanofiber Trap. *Phys. Rev. Lett.*, 109:033603, Jul 2012. URL <http://dx.doi.org/10.1103/PhysRevLett.109.033603>. (cited in p. 7, 46, 48, 50, and 80)

- [Goban15] A. Goban. *Strong atom-light interactions along nanostructures: Transition from free-space to nanophotonic interfaces*. Ph.D. thesis, California Institute of Technology, 2015. (cited in p. 44)
- [Gorlitz01] A. Gorlitz, T. Kinoshita, T. W. Hansch, and A. Hemmerich. Realization of bichromatic optical superlattices. *Phys. Rev. A*, 64:011401, Jun 2001. URL <http://dx.doi.org/10.1103/PhysRevA.64.011401>. (cited in p. 88)
- [Gorniaczyk14] H. Gorniaczyk, C. Tresp, J. Schmidt, H. Fedder, and S. Hofferberth. Single-Photon Transistor Mediated by Interstate Rydberg Interactions. *Phys. Rev. Lett.*, 113:053601, Jul 2014. URL <http://dx.doi.org/10.1103/PhysRevLett.113.053601>. (cited in p. 4)
- [Gouraud15] B. Gouraud, D. Maxein, A. Nicolas, O. Morin, and J. Laurat. Demonstration of a Memory for Tightly Guided Light in an Optical Nanofiber. *Phys. Rev. Lett.*, 114:180503, May 2015. URL <http://dx.doi.org/10.1103/PhysRevLett.114.180503>. (cited in p. 7, 32, and 67)
- [Gouraud16] B. Gouraud. *Optical Nanofibers Interfacing Cold atoms: A Tool for Quantum Optics*. Ph.D. thesis, LKB, UPMC (Jussieu), 2016. (cited in p. 18, 32, and 49)
- [Grunzweig10] T. Grunzweig, A. Hilliard, M. McGovern, and M. F. Andersen. Near-deterministic preparation of a single atom in an optical microtrap. *Nat Phys*, 6(12):951–954, December 2010. URL <http://dx.doi.org/10.1038/nphys1778>. (cited in p. 91)
- [Han10] Y. Han, B. He, K. Heshami, C. Z. Li, and C. Simon. Quantum repeaters based on Rydberg-blockade-coupled atomic ensembles. *Physical Review A - Atomic, Molecular, and Optical Physics*, 81(5), 2010. 1003.2353, URL <http://dx.doi.org/10.1103/PhysRevA.81.052311>. (cited in p. 4)
- [Har06] *Exploring the Quantum: Atoms, Cavities, and Photons..* Oxford Univ. Press, 2006. (cited in p. 3)
- [Hendrickson09] S. M. Hendrickson, T. B. Pittman, and J. D. Franson. Non-linear transmission through a tapered fiber in rubidium vapor. *J. Opt. Soc. Am. B*, 26(2):267–271, Feb 2009. URL <http://dx.doi.org/10.1364/JOSAB.26.000267>. (cited in p. 7)
- [Heshami16] K. Heshami, D. G. England, P. C. Humphreys, P. J. Bustard, V. M. Acosta, J. Nunn, and B. J. Sussman. Quantum memories: emerging applications and recent advances. *Journal of*

- Modern Optics*, 63(20):2005–2028, 2016. <http://dx.doi.org/10.1080/09500340.2016.1148212>, URL <http://dx.doi.org/10.1080/09500340.2016.1148212>. (cited in p. 4)
- [Hétet11] G. Hétet, L. Slodička, M. Hennrich, and R. Blatt. Single Atom as a Mirror of an Optical Cavity. *Phys. Rev. Lett.*, 107:133002, Sep 2011. URL <http://dx.doi.org/10.1103/PhysRevLett.107.133002>. (cited in p. 3)
- [Hoffman14a] J. Hoffman. *Optical nanofiber fabrication and analysis towards coupling atoms to superconducting qubits*. Ph.D. thesis, University of Maryland, 2014. (cited in p. 34 and 35)
- [Hoffman14b] J. E. Hoffman, S. Ravets, J. A. Grover, P. Solano, P. R. Kordell, J. D. Wong-Campos, L. A. Orozco, and S. L. Rolston. Ultrahigh transmission optical nanofibers. *AIP Advances*, 4(6):067124, 2014. URL <http://dx.doi.org/http://dx.doi.org/10.1063/1.4879799>. (cited in p. 6, 18, and 26)
- [Hoffman15] J. E. Hoffman, F. K. Fatemi, G. Beadie, S. L. Rolston, and L. A. Orozco. Rayleigh scattering in an optical nanofiber as a probe of higher-order mode propagation. *Optica*, 2(5):416–423, May 2015. URL <http://dx.doi.org/10.1364/OPTICA.2.000416>. (cited in p. 18 and 20)
- [Hoi12] I. C. Hoi, T. Palomaki, J. Lindkvist, G. Johansson, P. Delsing, and C. M. Wilson. Generation of nonclassical microwave states using an artificial atom in 1D open space. *Physical Review Letters*, 108(26), 2012. 1201.2269, URL <http://dx.doi.org/10.1103/PhysRevLett.108.263601>. (cited in p. 5)
- [Julsgaard04] B. Julsgaard, J. Sherson, J. I. Cirac, J. Fiurášek, and E. S. Polzik. Experimental demonstration of quantum memory for light. *Nature*, 432(7016):482–486, 2004. 0410072, URL <http://dx.doi.org/10.1038/nature03064>. (cited in p. 1)
- [Junge13] C. Junge, D. O’Shea, J. Volz, and A. Rauschenbeutel. Strong Coupling between Single Atoms and Nontransversal Photons. *Phys. Rev. Lett.*, 110:213604, May 2013. URL <http://dx.doi.org/10.1103/PhysRevLett.110.213604>. (cited in p. 4 and 17)
- [Karapetyan12] K. Karapetyan. *Single optical microfibres-based modal interferometer*. Ph.D. thesis, Rheinische FriedrichWilhelms-Universität Bonn, 2012. (cited in p. 21)

- [Kato15] S. Kato and T. Aoki. Strong Coupling between a Trapped Single Atom and an All-Fiber Cavity. *Phys. Rev. Lett.*, 115:093603, Aug 2015. URL <http://dx.doi.org/10.1103/PhysRevLett.115.093603>. (cited in p. 7)
- [Kaufman12] A. M. Kaufman, B. J. Lester, and C. A. Regal. Cooling a Single Atom in an Optical Tweezer to Its Quantum Ground State. *Phys. Rev. X*, 2:041014, Nov 2012. URL <http://dx.doi.org/10.1103/PhysRevX.2.041014>. (cited in p. 91)
- [Kenny91] R. Kenny, T. Birks, and K. Oakley. Control of optical fibre taper shape. *Electronics Letters*, 27(18):1654, 1991. URL <http://dx.doi.org/10.1049/el:19911034>. (cited in p. 23)
- [Khoon08] T. M. Khoon, Z. Chen, S. A. Aljunid, B. Chng, G. Maslennikov, and C. Kurtsiefer. Strong interaction between light and a single trapped atom without a cavity. In *Conference on Quantum Electronics and Laser Science (QELS) - Technical Digest Series*. 2008. 0802.3005, URL <http://dx.doi.org/10.1109/QELS.2008.4553171>. (cited in p. 3)
- [Kimble08] H. J. Kimble. The quantum internet. *Nature*, 453(7198):1023–1030, 2008. 0806.4195, URL <http://dx.doi.org/10.1038/nature07127>. (cited in p. 2)
- [Kómár14] P. Kómár, E. M. Kessler, M. Bishof, L. Jiang, A. S. Sørensen, J. Ye, and M. D. Lukin. A quantum network of clocks. *Nature Physics*, 10(8):582–587, jun 2014. arXiv:1310.6045v1, URL <http://dx.doi.org/10.1038/nphys3000>. (cited in p. 1)
- [Kuppens00] S. J. M. Kuppens, K. L. Corwin, K. W. Miller, T. E. Chupp, and C. E. Wieman. Loading an optical dipole trap. *Phys. Rev. A*, 62:013406, Jun 2000. URL <http://dx.doi.org/10.1103/PhysRevA.62.013406>. (cited in p. 45 and 59)
- [Kurizki15] G. Kurizki, P. Bertet, Y. Kubo, K. Mølmer, D. Petrosyan, P. Rabl, and J. Schmiedmayer. Quantum technologies with hybrid systems. *Proceedings of the National Academy of Sciences*, 112(13):3866–3873, March 2015. URL <http://www.pnas.org/content/112/13/3866>. (cited in p. 92)
- [Lacroute12] C. Lacroute, K. S. Choi, A. Goban, D. J. Alton, D. Ding, N. P. Stern, and H. J. Kimble. A state-insensitive, compensated nanofiber trap. *New Journal of Physics*, 14(2):023056, 2012. URL <http://stacks.iop.org/1367-2630/14/i=2/a=023056>. (cited in p. 44, 45, 46, and 77)

- [Le Kien04] F. Le Kien, V. I. Balykin, and K. Hakuta. Atom trap and waveguide using a two-color evanescent light field around a subwavelength-diameter optical fiber. *Physical Review A*, 70(6):063403, December 2004. URL <http://dx.doi.org/10.1103/PhysRevA.70.063403>. (cited in p. 44)
- [Le Kien05] F. Le Kien, S. D. Gupta, V. I. Balykin, and K. Hakuta. Spontaneous emission of a cesium atom near a nanofiber: Efficient coupling of light to guided modes. *Physical Review A*, 72(3):032509, September 2005. URL <http://dx.doi.org/10.1103/PhysRevA.72.032509>. (cited in p. 10)
- [Le Kien13] F. Le Kien, P. Schneeweiss, and A. Rauschenbeutel. Dynamical polarizability of atoms in arbitrary light fields: general theory and application to cesium. *The European Physical Journal D*, 67(5):92, 2013. URL <http://dx.doi.org/10.1140/epjd/e2013-30729-x>. (cited in p. 44, 46, and 77)
- [Le Kien14a] F. Le Kien and A. Rauschenbeutel. Anisotropy in scattering of light from an atom into the guided modes of a nanofiber. *Physical Review A*, 90(2):023805, August 2014. URL <http://dx.doi.org/10.1103/PhysRevA.90.023805>. (cited in p. 70 and 75)
- [Le Kien14b] F. Le Kien and A. Rauschenbeutel. Propagation of nanofiber-guided light through an array of atoms. *Phys. Rev. A*, 90:063816, Dec 2014. URL <http://dx.doi.org/10.1103/PhysRevA.90.063816>. (cited in p. 70, 74, and 76)
- [Leon-Saval04] S. G. Leon-Saval, T. A. Birks, W. J. Wadsworth, P. S. Russell, and M. W. Mason. Supercontinuum generation in sub-micron fibre waveguides. *Opt. Express*, 12(13):2864–2869, Jun 2004. URL <http://dx.doi.org/10.1364/OPEX.12.002864>. (cited in p. 9)
- [Lester15] B. J. Lester, N. Luick, A. M. Kaufman, C. M. Reynolds, and C. A. Regal. Rapid Production of Uniformly Filled Arrays of Neutral Atoms. *Phys. Rev. Lett.*, 115:073003, Aug 2015. URL <http://dx.doi.org/10.1103/PhysRevLett.115.073003>. (cited in p. 61 and 91)
- [Lloyd96] S. Lloyd. Universal Quantum Simulators. *Science*, 273(5278):1073–1078, 1996. URL <http://dx.doi.org/10.1126/science.273.5278.1073>. (cited in p. 2)
- [Lodahl17] P. Lodahl, S. Mahmoodian, S. Stobbe, A. Rauschenbeutel, P. Schneeweiss, J. Volz, H. Pichler, and P. Zoller. Chiral quantum optics. *Nature*, 541(7638):473–480, January 2017. URL

- <http://dx.doi.org/10.1038/nature21037>. (cited in p. 5 and 15)
- [Lukin01] M. D. Lukin, M. Fleischhauer, R. Cote, L. M. Duan, D. Jaksch, J. I. Cirac, and P. Zoller. Dipole Blockade and Quantum Information Processing in Mesoscopic Atomic Ensembles. *Phys. Rev. Lett.*, 87:037901, Jun 2001. URL <http://dx.doi.org/10.1103/PhysRevLett.87.037901>. (cited in p. 4)
- [Lutzler12] C. Lutzler. *Fabrication of Optical Microfibers*. Master's thesis, University of Bonn, 2012. (cited in p. 32)
- [McKeever04] J. McKeever. Deterministic Generation of Single Photons from One Atom Trapped in a Cavity. *Science*, 303(5666):1992–1994, 2004. URL <http://dx.doi.org/10.1126/science.1095232>. (cited in p. 3)
- [Mitsch14a] R. Mitsch, C. Sayrin, B. Albrecht, P. Schneeweiss, and A. Rauschenbeutel. Exploiting the local polarization of strongly confined light for sub-micrometer-resolution internal state preparation and manipulation of cold atoms. *Phys. Rev. A*, 89:063829, Jun 2014. URL <http://dx.doi.org/10.1103/PhysRevA.89.063829>. (cited in p. 17 and 91)
- [Mitsch14b] R. Mitsch, C. Sayrin, B. Albrecht, P. Schneeweiss, and A. Rauschenbeutel. Quantum state-controlled directional spontaneous emission of photons into a nanophotonic waveguide. *Nature Communications*, 5, December 2014. URL <http://dx.doi.org/10.1038/ncomms6713>. (cited in p. 17)
- [Monroe95] C. Monroe, D. M. Meekhof, B. E. King, W. M. Itano, and D. J. Wineland. Demonstration of a fundamental quantum logic gate. *Physical Review Letters*, 75(25):4714–4717, 1995. URL <http://dx.doi.org/10.1103/PhysRevLett.75.4714>. (cited in p. 1)
- [Morrissey09] M. J. Morrissey, K. Deasy, Y. Wu, S. Chakrabarti, and S. Nic Chormaic. Tapered optical fibers as tools for probing magneto-optical trap characteristics. *Review of Scientific Instruments*, 80(5):053102, 2009. URL <http://dx.doi.org/http://dx.doi.org/10.1063/1.3117201>. (cited in p. 7)
- [Nagai14] R. Nagai and T. Aoki. Ultra-low-loss tapered optical fibers with minimal lengths. *Opt. Express*, 22(23):28427–28436, Nov 2014. URL <http://dx.doi.org/10.1364/OE.22.028427>. (cited in p. 18 and 21)

- [Nayak09] K. P. Nayak. *Optical Nanofibers for Manipulating Atoms and Photons*. Theses, University of Electro-Communications, 2009. URL [http://ir.lib.uec.ac.jp/infolib/user\\_contents/9000000344/9000000344.pdf](http://ir.lib.uec.ac.jp/infolib/user_contents/9000000344/9000000344.pdf). (cited in p. 7)
- [Nicolas14] A. Nicolas, L. Veissier, L. Giner, E. Giacobino, D. Maxein, and J. Laurat. A quantum memory for orbital angular momentum photonic qubits. *Nat Photon*, 8(3):234–238, March 2014. URL <http://dx.doi.org/10.1038/nphoton.2013.355>. (cited in p. 4)
- [Nielsen10] M. A. Nielsen and I. L. Chuang. *Quantum Computation and Quantum Information*. Cambridge University Press, 10th Anniversary Edition, 2010. (cited in p. 1)
- [Okaba14] S. Okaba, T. Takano, F. Benabid, T. Bradley, L. Vincetti, Z. Maizelis, V. Yampol’skii, F. Nori, and H. Katori. Lamb-Dicke spectroscopy of atoms in a hollow-core photonic crystal fibre. *Nature Communications*, 5, 2014. 1408.0659, URL <http://dx.doi.org/10.1038/ncomms5096>. (cited in p. 5)
- [Østfeldt17] C. Østfeldt, J.-B. Béguin, F. T. Pedersen, E. S. Polzik, J. H. Müller, and J. Appel. Dipole force free optical control and cooling of nanofiber trapped atoms. pages 1–5, 2017. 1708.03488, URL <http://arxiv.org/abs/1708.03488>. (cited in p. 91)
- [Palittapongarnpim12] P. Palittapongarnpim, A. MacRae, and A. I. Lvovsky. A Monolithic Filter Cavity for Experiments in Quantum Optics. *arXiv:1203.4843*, 066101:83–85, 2012. URL <http://arxiv.org/abs/1203.4843>{%}0Ahttp://www.arxiv.org/pdf/1203.4843.pdf. (cited in p. 59)
- [Patnaik02] A. K. Patnaik, J. Q. Liang, and K. Hakuta. Slow light propagation in a thin optical fiber via electromagnetically induced transparency. *Physical Review A*, 66(6):063808, December 2002. URL <http://dx.doi.org/10.1103/PhysRevA.66.063808>. (cited in p. 7)
- [Paulisch16] V. Paulisch, H. J. Kimble, and A. González-Tudela. Universal quantum computation in waveguide QED using decoherence free subspaces. *New Journal of Physics*, 18(4), 2016. 1512.04803, URL <http://dx.doi.org/10.1088/1367-2630/18/4/043041>. (cited in p. 5)
- [Petersen14] J. Petersen, J. Volz, and A. Rauschenbeutel. Chiral nanophotonic waveguide interface based on spin-orbit

- interaction of light. *Science*, 346(6205):67–71, 2014. <http://www.sciencemag.org/content/346/6205/67.full.pdf>, URL <http://dx.doi.org/10.1126/science.1257671>. (cited in p. 17)
- [Peyronel12] T. Peyronel, O. Firstenberg, Q.-Y. Liang, S. Hofferberth, A. V. Gorshkov, T. Pohl, M. D. Lukin, and V. Vuletic. Quantum nonlinear optics with single photons enabled by strongly interacting atoms. *Nature*, 488(7409):57–60, August 2012. URL <http://dx.doi.org/10.1038/nature11361>. (cited in p. 2)
- [Pritchard10] J. D. Pritchard, D. Maxwell, A. Gauguet, K. J. Weatherill, M. P. A. Jones, and C. S. Adams. Cooperative atom-light interaction in a blockaded Rydberg ensemble. *Physical Review Letters*, 105(19), 2010. 1006.4087, URL <http://dx.doi.org/10.1103/PhysRevLett.105.193603>. (cited in p. 4)
- [Ravets13] S. Ravets, J. E. Hoffman, P. R. Kordell, J. D. Wong-Campos, S. L. Rolston, and L. A. Orozco. Intermodal energy transfer in a tapered optical fiber: optimizing transmission. *J. Opt. Soc. Am. A*, 30(11):2361–2371, Nov 2013. URL <http://dx.doi.org/10.1364/JOSAA.30.002361>. (cited in p. 18)
- [Reiserer14] A. Reiserer, N. Kalb, G. Rempe, and S. Ritter. A quantum gate between a flying optical photon and a single trapped atom. *Nature*, 508(7495):237–240, April 2014. URL <http://dx.doi.org/10.1038/nature13177>. (cited in p. 3)
- [Rist09] S. Rist, P. Vignolo, and G. Morigi. Photonic spectrum of bichromatic optical lattices. *Phys. Rev. A*, 79:053822, May 2009. URL <http://dx.doi.org/10.1103/PhysRevA.79.053822>. (cited in p. 90)
- [Rosenbusch09] P. Rosenbusch, S. Ghezali, V. A. Dzuba, V. V. Flambaum, K. Beloy, and A. Derevianko. Ac Stark shift of the Cs microwave atomic clock transitions. *Physical Review A - Atomic, Molecular, and Optical Physics*, 79(1):1–8, 2009. 0810.4208, URL <http://dx.doi.org/10.1103/PhysRevA.79.013404>. (cited in p. 44)
- [Sagué07] G. Sagué, E. Vetsch, W. Alt, D. Meschede, and A. Rauschenbeutel. Cold-Atom Physics Using Ultrathin Optical Fibers: Light-Induced Dipole Forces and Surface Interactions. *Phys. Rev. Lett.*, 99:163602, Oct 2007. URL <http://dx.doi.org/10.1103/PhysRevLett.99.163602>. (cited in p. 7)
- [Sayrin15] C. Sayrin, C. Clausen, B. Albrecht, P. Schneeweiss, and A. Rauschenbeutel. Storage of fiber-guided light in a nanofiber-trapped ensemble of cold atoms. *Optica*, 2(4):353–356, Apr

2015. URL <http://dx.doi.org/10.1364/OPTICA.2.000353>. (cited in p. 7 and 17)
- [Scheucher16] M. Scheucher, A. Hilico, E. Will, J. Volz, and A. Rauschenbeutel. Quantum optical circulator controlled by a single chirally coupled atom. *Science*, 354(6319):1577–1580, 2016. <http://science.sciencemag.org/content/354/6319/1577.full.pdf>, URL <http://dx.doi.org/10.1126/science.aaj2118>. (cited in p. 17)
- [Schilke11] A. Schilke, C. Zimmermann, P. Courteille, and W. Guerin. Photonic Band Gaps in One-Dimensionally Ordered Cold Atomic Vapors. *Phys. Rev. Lett.*, 106:223903, 2011. URL <http://dx.doi.org/10.1103/PhysRevLett.106.223903>. (cited in p. 69 and 76)
- [Schlosser02] N. Schlosser, G. Reymond, and P. Grangier. Collisional Blockade in Microscopic Optical Dipole Traps. *Phys. Rev. Lett.*, 89:023005, Jun 2002. URL <http://dx.doi.org/10.1103/PhysRevLett.89.023005>. (cited in p. 45)
- [Shen05] J. T. Shen and F. Shanhui. Coherent photon transport from spontaneous emission in one-dimensional waveguides. *Optics Lett.*, 30, 15:2001–2003, 2005. URL <https://www.osapublishing.org/ol/abstract.cfm?uri=ol-30-15-2001>. (cited in p. 70)
- [Shomroni14] I. Shomroni, S. Rosenblum, Y. Lovsky, O. Bechler, G. Guendelman, and B. Dayan. All-optical routing of single photons by a one-atom switch controlled by a single photon. *Science*, 345(6199):903–906, 2014. <http://science.sciencemag.org/content/345/6199/903.full.pdf>, URL <http://dx.doi.org/10.1126/science.1254699>. (cited in p. 4 and 17)
- [Slama05] S. Slama, C. von Cube, B. Deh, A. Ludewig, C. Zimmermann, and P. W. Courteille. Phase-Sensitive Detection of Bragg Scattering at 1D Optical Lattices. *Phys. Rev. Lett.*, 94:193901, 2005. URL <http://journals.aps.org/prl/pdf/10.1103/PhysRevLett.94.193901>. (cited in p. 69)
- [Slama06] S. Slama, C. von Cube, M. Kohler, C. Zimmermann, and P. W. Courteille. Multiple reflections and diffuse scattering in Bragg scattering at optical lattices. *Phys. Rev. A*, 73:023424, 2006. URL <http://dx.doi.org/10.1103/PhysRevA.73.023424>. (cited in p. 80)
- [Snyder83] A. W. Snyder and J. D. Love. *Optical Waveguide Theory*. Chapman & Hall, 1983. (cited in p. 10 and 13)

- [Solano17a] P. Solano, P. Barberis-Blostein, F. K. Fatemi, L. A. Orozco, and S. L. Rolston. Super- and sub-radiance reveal infinite-range interactions through a nanofiber. pages 1–19, 2017. 1704.07486, URL <http://arxiv.org/abs/1704.07486>. (cited in p. 7)
- [Solano17b] P. Solano, F. K. Fatemi, L. A. Orozco, and S. L. Rolston. Dynamics of trapped atoms around an optical nanofiber probed through polarimetry. pages 1–5, 2017. 1703.09122, URL <http://arxiv.org/abs/1703.09122>. (cited in p. 7)
- [Solano17c] P. Solano, J. A. Grover, J. Hoffman, S. Ravets, F. Fatemi, L. Orozco, and R. S.L. Optical Nanofibers: a new platform for quantum optics. *arXiv:1703.10533*, 2017. URL <https://arxiv.org/abs/1703.10533>. (cited in p. 5)
- [Solano17d] P. Solano, J. A. Grover, Y. Xu, P. Barberis-Blostein, J. N. Munday, L. A. Orozco, W. D. Phillips, and S. L. Rolston. Alignment-dependent decay rate of an atomic dipole near an optical nanofiber. pages 1–12, 2017. 1704.08741, URL <http://arxiv.org/abs/1704.08741>. (cited in p. 7)
- [Sørensen16] H. L. Sørensen, J.-B. Béguin, K. W. Kluge, I. Iakoupov, A. S. Sørensen, J. H. Müller, E. S. Polzik, and J. Appel. Coherent Backscattering of Light Off One-Dimensional Atomic Strings. *Phys. Rev. Lett.*, 117:133604, Sep 2016. URL <http://dx.doi.org/10.1103/PhysRevLett.117.133604>. (cited in p. 7 and 85)
- [Sparkes13] B. M. Sparkes, J. Bernu, M. Hosseini, J. Geng, Q. Glorieux, P. A. Altin, P. K. Lam, N. P. Robins, and B. C. A. Buchler. Gradient echo memory in an ultra-high optical depth cold atomic ensemble. *New Journal of Physics*, 15, 2013. 1211.7171, URL <http://dx.doi.org/10.1088/1367-2630/15/8/085027>. (cited in p. 67)
- [Spillane08] S. M. Spillane, G. S. Pati, K. Salit, M. Hall, P. Kumar, R. G. Beausoleil, and M. S. Shahriar. Observation of Nonlinear Optical Interactions of Ultralow Levels of Light in a Tapered Optical Nanofiber Embedded in a Hot Rubidium Vapor. *Phys. Rev. Lett.*, 100:233602, Jun 2008. URL <http://dx.doi.org/10.1103/PhysRevLett.100.233602>. (cited in p. 7)
- [Sprague14] M. R. Sprague, S. Michelberger P., M. Champion T. F., G. England D., N. J., J. X.-M., S. Kolthammer W., A. A., J. Russell P. St., and A. Walmsley I. Broadband single-photon-level memory in a hollow-core photonic crystal fibre. *Nat Photon*, 8(4):287–291, April 2014. URL <http://dx.doi.org/10.1038/nphoton.2014.45>. (cited in p. 5)

- [Steck] D. A. Steck. Quantum and Atom Optics. available online at <http://atomoptics-nas.uoregon.edu/dsteck/teaching/>. (cited in p. 43)
- [Steiner13] M. Steiner, H. M. Meyer, C. Deutsch, J. Reichel, and M. Köhl. Single ion coupled to an optical fiber cavity. *Physical Review Letters*, 110(4), 2013. 1211.0050, URL <http://dx.doi.org/10.1103/PhysRevLett.110.043003>. (cited in p. 4)
- [Sumetsky06] M. Sumetsky. How thin can a microfiber be and still guide light? *Opt. Lett.*, 31(7):870–872, Apr 2006. URL <http://dx.doi.org/10.1364/OL.31.000870>. (cited in p. 12)
- [Thompson13] J. D. Thompson, T. G. Tiecke, N. P. de Leon, J. Feist, A. V. Akimov, M. Gullans, A. S. Zibrov, V. Vuletic, and M. D. Lukin. Coupling a Single Trapped Atom to a Nanoscale Optical Cavity. *Science*, 340(6137):1202–1205, 2013. arXiv:1212.3127, URL <http://dx.doi.org/10.1126/science.1237125>. (cited in p. 4)
- [Tiarks14] D. Tiarks, S. Baur, K. Schneider, S. Dürr, and G. Rempe. Single-Photon Transistor Using a Förster Resonance. *Phys. Rev. Lett.*, 113:053602, Jul 2014. URL <http://dx.doi.org/10.1103/PhysRevLett.113.053602>. (cited in p. 2)
- [Tiecke14] T. G. Tiecke, J. D. Thompson, N. P. de Leon, L. R. Liu, V. Vuletic, and M. D. Lukin. Nanophotonic quantum phase switch with a single atom. *Nature*, 508(7495):241–244, April 2014. URL <http://dx.doi.org/10.1038/nature13188>. (cited in p. 4)
- [Tong03] L. Tong, R. R. Gattass, J. B. Ashcom, S. He, J. Lou, M. Shen, I. Maxwell, and E. Mazur. Subwavelength-diameter silica wires for low-loss optical wave guiding. *Nature*, 426(6968):816–9, 2003. URL <http://dx.doi.org/10.1038/nature02193>. (cited in p. 9)
- [Turchette95] Q. A. Turchette, C. J. Hood, W. Lange, H. Mabuchi, and H. J. Kimble. Measurement of conditional phase shifts for quantum logic. *Physical Review Letters*, 75(25):4710–4713, 1995. 9511008, URL <http://dx.doi.org/10.1103/PhysRevLett.75.4710>. (cited in p. 3)
- [Vetsch10] E. Vetsch, D. Reitz, G. Sagué, R. Schmidt, S. T. Dawkins, and A. Rauschenbeutel. Optical Interface Created by Laser-Cooled Atoms Trapped in the Evanescent Field Surrounding an Optical Nanofiber. *Phys. Rev. Lett.*, 104:203603, May 2010. URL <http://dx.doi.org/10.1103/PhysRevLett.104.203603>. (cited in p. 4)

- 1103/PhysRevLett.104.203603. (cited in p. 7, 45, and 46)
- [Vetsch12] E. Vetsch, S. Dawkins, R. Mitsch, D. Reitz, P. Schneeweiss, and A. Rauschenbeutel. Nanofiber-Based Optical Trapping of Cold Neutral Atoms. *Selected Topics in Quantum Electronics, IEEE Journal of*, 18(6):1763–1770, Nov 2012. URL <http://dx.doi.org/10.1109/JSTQE.2012.2196025>. (cited in p. 50 and 80)
- [Ward14] J. M. Ward, A. Maimaiti, V. H. Le, and S. N. Chormaic. Contributed Review: Optical micro- and nanofiber pulling rig. *Review of Scientific Instruments*, 85(11):111501, 2014. URL <http://dx.doi.org/10.1063/1.4901098>. (cited in p. 6 and 18)
- [Warken07] F. Warken. Ultra thin glass fibers as a tool for coupling light and matter. 2007. (cited in p. 35 and 36)
- [Weidemuller95] M. Weidemuller, A. Hemmerich, A. Gorlitz, T. Esslinger, and T. W. Hansch. Bragg Diffraction in an Atomic Lattice Bound by Light. *Phys. Rev. Lett.*, 75:4583, 1995. URL <http://journals.aps.org/prl/abstract/10.1103/PhysRevLett.75.4583>. (cited in p. 69)
- [Weiner99] J. Weiner, V. S. Bagnato, S. Zilio, and P. S. Julienne. Experiments and theory in cold and ultracold collisions. *Rev. Mod. Phys.*, 71:1–85, Jan 1999. URL <http://dx.doi.org/10.1103/RevModPhys.71.1>. (cited in p. 45)
- [Witthaut10] D. Witthaut and A. S. Sorensen. {P}hoton scattering by a three-level emitter in a one-dimensional waveguide. *New Journal of Physics*, 12:43052, 2010. URL <http://iopscience.iop.org/article/10.1088/1367-2630/12/4/043052/meta>. (cited in p. 85)
- [Wootters82] W. K. Wootters and W. H. Zurek. A single quantum cannot be cloned. *Nature*, 299(5886):802–803, 1982. 0210060, URL <http://dx.doi.org/10.1038/299802a0>. (cited in p. 2)
- [Wrigge08] G. Wrigge, I. Gerhardt, J. Hwang, G. Zumofen, and V. Sandoghdar. Efficient coupling of photons to a single molecule and the observation of its resonance fluorescence. *Nature Physics*, 4(1):60–66, 2008. 0707.3398, URL <http://dx.doi.org/10.1038/nphys812>. (cited in p. 3)
- [Wuttke13a] C. Wuttke, G. D. Cole, and A. Rauschenbeutel. Optically active mechanical modes of tapered optical fibers. *Phys. Rev. A*, 88:061801, Dec 2013. URL <http://dx.doi.org/10.1103/PhysRevA.88.061801>. (cited in p. 67)

- [Wuttke13b] C. Wuttke and A. Rauschenbeutel. Thermalization via Heat Radiation of an Individual Object Thinner than the Thermal Wavelength. *Physical Review Letters*, 111(2):024301, July 2013. URL <http://dx.doi.org/10.1103/PhysRevLett.111.024301>. (cited in p. 35)
- [Xiang13] Z.-L. Xiang, S. Ashhab, J. Q. You, and F. Nori. Hybrid quantum circuits: Superconducting circuits interacting with other quantum systems. *Rev. Mod. Phys.*, 85:623–653, Apr 2013. URL <http://dx.doi.org/10.1103/RevModPhys.85.623>. (cited in p. 92)
- [Yariv06] A. Yariv and Y. Pochi. *Photonics: Optical Electronics in Modern Communications*. Oxford University Press, 6th edition, 2006. (cited in p. 10)
- [Yin17] J. Yin, Y. Cao, Y.-H. Li, S.-K. Liao, L. Zhang, J.-G. Ren, W.-Q. Cai, W.-Y. Liu, B. Li, H. Dai, G.-B. Li, Q.-M. Lu, Y.-H. Gong, Y. Xu, S.-L. Li, F.-Z. Li, Y.-Y. Yin, Z.-Q. Jiang, M. Li, J.-J. Jia, G. Ren, D. He, Y.-L. Zhou, X.-X. Zhang, N. Wang, X. Chang, Z.-C. Zhu, N.-L. Liu, Y.-A. Chen, C.-Y. Lu, R. Shu, C.-Z. Peng, J.-Y. Wang, and J.-W. Pan. Satellite-based entanglement distribution over 1200 kilometers. *Science*, 356(6343):1140–1144, 2017. <http://science.sciencemag.org/content/356/6343/1140.full.pdf>, URL <http://dx.doi.org/10.1126/science.aan3211>. (cited in p. 1)
- [Zheng13] H. Zheng, D. J. Gauthier, and H. U. Baranger. Waveguide-QED-Based Photonic Quantum Computation. *Phys. Rev. Lett.*, 111:090502, Aug 2013. URL <http://dx.doi.org/10.1103/PhysRevLett.111.090502>. (cited in p. 5)

---

**Sujet : Couplage de chaînes d'atomes froids à une nanofibre optique: Démonstration d'un miroir de Bragg atomique**

---

**Résumé :** Le couplage de guides d'ondes nanoscopiques et d'atomes froids a récemment ouvert de nouvelles voies de recherche. Le guide d'onde dans notre cas est une nanofibre qui confine la lumière transversalement à une échelle inférieure à la longueur d'onde. La lumière guidée présente un fort champ évanescent permettant une interaction atome-photon exaltée au voisinage de la nanofibre. Dans notre expérience, un nuage atomique froid est d'abord superposé à une nanofibre optique. Puis, en utilisant un piège dipolaire via le champ évanescent de la nanofibre, les atomes froids sont piégés à proximité de sa surface. Avec cette plateforme, nous avons obtenu des épaisseurs optiques élevées ( $OD \sim 100$ ) et de longues durées de vie ( $\sim 25$  ms) en utilisant un schéma de piégeage qui préserve les propriétés internes des atomes. Une direction intéressante est alors d'explorer les effets collectifs résultant de l'ordre spatial des atomes. Lorsque la période du réseau est proche de la longueur d'onde de résonance, une réflexion de Bragg aussi élevée que 75 % est observée. Cette réflexion dépend de la polarisation de la sonde par rapport aux réseaux atomiques - une signature de la chiralité dans les systèmes à guide d'ondes nanoscopiques. La possibilité de contrôler le transport de photons dans les guides d'ondes couplés à des systèmes de spin permettrait de nouvelles fonctionnalités pour les réseaux quantiques et l'étude d'effets collectifs résultant d'interactions à longue distance.

*Cette thèse est rédigée en langue anglaise.*

**Mots clés :** nanofibre optique, guide d'ondes, atomes froids, piège dipolaire, réseau optique, transparence induite électromagnétiquement, transition raman, miroir de Bragg, optique non linéaire quantique

---

**Subject : Coupling 1D Atom Arrays to an Optical Nanofiber: Demonstration of an Efficient Bragg Atomic Mirror**

---

**Abstract :** The coupling of cold atoms to 1D nanoscale waveguides have opened new avenues of research. The waveguide in our case is a nanofiber, which confines light transversally to a subwavelength scale. The guided light exhibits a strong evanescent field allowing enhanced atom-photon interaction in the vicinity of nanofiber. In our experiment, a cold atomic cloud is first interfaced with an optical nanofiber. By using an optical lattice in the evanescent field, the atoms are then trapped in 1D atomic arrays close to the nanofiber. In this platform, we reach high optical depth ( $OD \sim 100$ ) and long lifetimes ( $\sim 25$  ms) by using a dual-color compensated trapping scheme that preserves the internal properties of atoms. In this thesis, we explore collective effects emerging from the spatial ordering of atoms. When the period of the lattice is made close to commensurate with the resonant wavelength, Bragg reflection as high as 75 % is observed. The reflection shows dependency on orientation of the probe polarization relative to the atomic arrays - a chiral signature in nanoscale waveguide-QED systems. The ability to control photon transport in 1D waveguides coupled to spin systems would enable novel quantum networking capabilities and the study of many-body effects arising from long-range interactions.

*This thesis is written in English.*

---

**Keywords :** optical nanofiber, nanoscale waveguide, waveguide QED, cold atoms, dipole trap, optical lattice, electromagnetically-induced transparency, Raman transition, Bragg mirror, quantum non-linear optics